Electron Spin Dynamics in Quantum Dots, and the Roles of Charge Transfer Excited States in Diluted Magnetic Semiconductors

William K. Liu

A dissertation submitted in partial fulfillment of the
requirements for the degree of

Doctor of Philosophy

University of Washington

2007

Program Authorized to Offer Degree:
Chemistry

University of Washington
Graduate School

This is to certify that I have examined this copy of a doctoral dissertation by

William K. Liu

and have found that it is complete and satisfactory in all respects,
and that any and all revisions required by the final
examining committee have been made.

Chair of the Supervisory Committee:

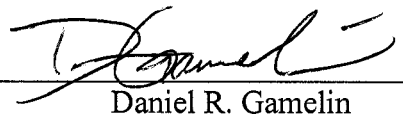

Daniel R. Gamelin

Reading Committee:

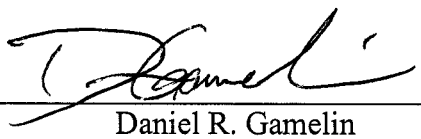

Daniel R. Gamelin

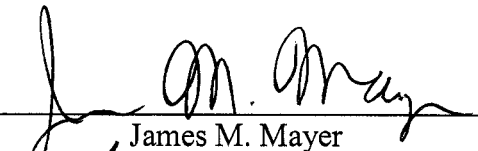

James M. Mayer

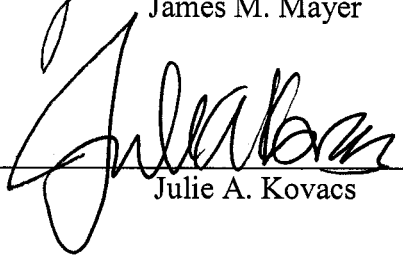

Julie A. Kovacs

Date: 8/15/07

In presenting this dissertation in partial fulfillment of the requirements for the doctoral degree at the University of Washington, I agree that the Library shall make its copies freely available for inspection. I further agree that extensive copying of the dissertation is allowable only for scholarly purposes, consistent with "fair use" as prescribed in the U.S. Copyright Law. Requests for copying or reproduction of this dissertation may be referred to ProQuest Information and Learning, 300 North Zeeb Road, Ann Arbor, MI 48106-1346, 1-800-521-0600, to whom the author has granted "the right to reproduce and sell (a) copies of the manuscript in microform and/or (b) printed copies of the manuscript made from microform."

Signature William Kavi Jr

Date 8/15/07

University of Washington

Abstract

Electron Spin Dynamics in Quantum Dots, and the
Roles of Charge Transfer Excited States in Diluted Magnetic Semiconductors

William K. Liu

Chair of the Supervisory Committee:
Associate Professor Daniel R. Gamelin
Department of Chemistry

In this dissertation, photoelectrochemical measurements have been used in combination with absorption and magnetic circular dichroism spectroscopic measurements to investigate the electronic structural properties of nanocrystalline Co^{2+}:ZnO and Mn^{2+}:ZnO diluted magnetic semiconductors that give rise to macroscopic charge separation when these materials are excited with photons throughout the visible energy range. From analysis of the spectroscopic results, sub-bandgap charge transfer transitions have been identified and shown to be responsible for the photoinduced charge separation in these materials. In a broader context, these charge transfer excited states are shown to be relevant to the understanding of ferromagnetism of TM^{2+}:ZnO, where TM^{2+} denotes $3d$ transition metal cations. The assignment of the charge transfer transition (ligand-to-metal versus

metal-to-ligand) can reveal the polarity of the carriers that mediate the ferromagnetism (*n*-type versus *p*-type, respectively). To investigate the exchange interaction between the carrier and magnetic dopant cation of TM^{2+}:ZnO diluted magnetic semiconductors, electron paramagnetic resonance measurements were performed on colloidal Co^{2+}:ZnO and Mn^{2+}:ZnO nanocrystals possessing additional quantum-confined conduction band electrons. Additionally, the electron-nuclear hyperfine interaction between nuclear spins of ^{67}Zn cations and additional quantum-confined conduction band electrons, as reflected in the spin dephasing time, in colloidal ZnO quantum dots is investigated by electron paramagnetic resonance spectroscopy.

TABLE OF CONTENTS

Page

LIST OF FIGURES

LIST OF TABLES

ACKNOWLEDGMENTS

I wish to express my sincere appreciation to the Department of Chemistry for their financial and administrative support. I want to thank Professor Daniel R. Gamelin for being an exceptional mentor during my time as a graduate student in his research group. He has been an endless source of knowledge, support, and inspiration. In addition, I want to thank all the previous and current group members as well as all the other brilliant people I had the pleasure to meet and work with. The work presented in this dissertation would not have been possible had it not been for all their indispensable contributions of effort, insight, and knowledge.

Specifically, I want to express my deepest gratitude to those listed below who have greatly enriched my personal and academic life during my time at the University of Washington. This list is by no means complete, and I offer my apology to any of those I may have inadvertently forgotten.

Prof. Daniel R. Gamelin
Prof. Bruce H. Robinson
Prof. Mackay Salley
Prof. Victor Polinger
Dr. J. Daniel Bryan
Dr. Dana A. Schwartz
Dr. Pavle V. Radovanovic
Dr. Nick S. Norberg
Dr. Kevin R. Kittilstved
Dr. Jialong Zhao
Dr. Stefan Ochsenbein
Dr. Rémi Beaulac
Dr. Priscilla Lugo-Mas

Paul "Skippy" Archer
Kelly Whitaker
Claire Johnson
Steve Santangelo
Alyssa Smith
Michael White
Diane Zhong
Curtis Deer
Vladimir Vlaskin
Bridget Williams

DEDICATION

To my parents for all their sacrifice and encouragement.

Chapter 1: Introduction

1.1 Introduction

The present and future state of an industrialized world relies heavily on the available resources of energy. In 2004, the global annual energy consumption was ~15 TW and it is projected to increase to ~23.5 TW by 2030.[1] Currently, fossil fuels (oil, coal, and natural gas) supply the majority of the global energy demand. With the ever growing public concerns, however, of dramatic global climate changes caused by elevating CO_2 levels,[2-4] harmful environmental impact from oil drilling and numerous oil spills,[5-13] and the continuing consumption of the world's nonrenewable oil and coal reserves[1] have motivated the scientific community to search for viable methods of harvesting other energy sources.

One of the most readily available and abundant energy sources that can be tapped is solar radiation. With a temperature of about 6000 K, the Sun emits a continuing influx of radiation from its surface with an energy distribution very similar to a blackbody. The enormous amount of energy, approximately 9.5×10^{24} W that impinges on the Earth's surface, could conceivably be collected and used to produce both fuel (hydrogen fuel) and electricity without generating detrimental environmental pollutants such as greenhouse gases from combustion of fossil fuels or radioactive byproducts from nuclear plants. The major obstacle that continues to challenge the scientific community to this day, however, is how to efficiently tap into this gigantic energy reservoir.

The pivotal discovery of photocatalytic water decomposition on TiO_2 electrodes[14] by ultraviolet light irradiation brought about a renewed interest in using solar energy for generating a clean and renewable source of carbon-free energy (Eqn. 1.1.1).

$$TiO_2 \xrightarrow{h\nu(UV)} e^-_{CB} + h^+_{VB} \qquad \text{Eqn. [1.1.1(a)]}$$

$$2e^-_{CB} + 2H^+ \rightarrow H_{2(g)} \qquad \text{Eqn. [1.1.1(b)]}$$

$$2h^+_{VB} + H_2O \rightarrow \frac{1}{2}O_2 + 2H^+ \qquad \text{Eqn. [1.1.1(c)]}$$

The overall reaction is the photodecomposition of water

$$H_2O \xrightarrow{h\nu(UV)} \frac{1}{2}O_2 + H_2 \qquad \text{Eqn. [1.1.1(d)]}$$

Unfortunately, one of the major limitation preventing this (TiO_2) and other wide bandgap semiconductor photoelectrodes (such as $SrTiO_3$[15] and $InTaO_4$[16]) from becoming a commercially viable avenue of producing hydrogen and oxygen from photocatalytic cleavage of water or used in solar cells for direct conversion of solar energy to electricity is the poor matching of their absorption spectra with that of the Sun's solar spectrum. Thus, considerable effort has been devoted by numerous investigators with the ultimate goal of shifting or extending the photoresponse of these wide bandgap semiconductors into the visible spectral region of the solar spectrum, since a large fraction of the solar power output consists of wavelengths in that spectral range.

Among the diverse approaches taken in the field of semiconductor-based photocatalysis and photoelectrochemistry, one widely used strategy for extending the photoresponse of wide bandgap semiconductors to the visible spectral region of the solar spectrum have been doping with 3*d* transition metal impurities.[16-26] The doping process entails a small percentage of the metal impurity cations substitutionally replacing the host semiconductor lattice cations. Kudo *et al.* demonstrated photocatalytic H_2 evolution from an aqueous Na_2SO_3 solution under visible light irradiation (λ>420 nm) on Cu^{2+}-doped ZnS macroscopic crystalline particles.[17] Zou *et al.* demonstrated that $InTaO_4$ doped with transition metal cations of Mn, Co, or Ni would photocatalytically evolve H_2 and O_2 from CH_3OH/H_2O and $AgNO_3/H_2O$ solutions, respectively, under visible light illumination (λ>420 nm).[18] And similarly, Jaramillo *et al.* observed H_2 production off the platinum counter electrode submerged in an aqueous electrolyte and coupled to a Co^{2+}-doped ZnO electrode that was under illumination at λ>400 nm in a photoelectrochemical cell arrangement.[21] The above examples unambiguously demonstrate the consequences of incorporating dopant impurities into wide bandgap semiconductors, however, the nature by which photoexcitation of these dopant impurities results in the observed photoresponse have not been adequately examined and deserves some attention. The central paradox behind the observed photoresponse in these transition metal doped semiconductors is that the ligand field excitations are highly localized at the transition metal dopant

cation. Therefore, the process by which such an excitation could lead to electron-hole separation to generate the observed photoresponse is not apparent.

In Chapter 2, nanocrystalline Co^{2+}-doped ZnO electrodes are used as a model system by which to elucidate the mechanism of photoinduced carrier generation in this and similar doped semiconductors. The use of Co^{2+}-doped ZnO is ideal because it possesses a well characterized and prominent spin-orbit-split $^4A_2 \rightarrow {}^4T_1(P)$ ligand field band feature in the visible spectral region of the electronic absorption spectrum arising from the Co^{2+} in the trigonally distorted tetraoxo cation coordination environment of wurtzite ZnO,[27,28] and numerous researchers have observed photoresponse in this material under visible light illumination.[20-26]

The electronic structural information obtained from spectroscopic and photoelectrochemical measurements in Chapter 2 is not limited to just elucidating the mechanism behind the photoresponse in transition metal doped semiconductors, but also has relevance in explaining the observed high Curie temperature ferromagnetism in transition metal doped oxide semiconductors[27,29-36]. In the broad field of magnetic materials research, transition metal doped oxide semiconductors fall under the general class of diluted magnetic semiconductors. As described above, a fraction of the diamagnetic semiconductor lattice cations are substitutionally replaced with magnetic cations. The presence of these localized magnetic cations in the nonmagnetic semiconductor host leads to *s,p-d* exchange interaction (exchange interaction between the semiconductor valence band electrons and dopant *d* electrons, and exchange

interaction between the semiconductor conduction band electrons and dopant *d* electrons).[37] This *s,p-d* exchange interaction results in giant excitonic Zeeman splitting that can lead to interesting magneto-optical effects, such as giant Faraday rotation, and in ferromagnetism in some of the doped semiconductors.[38] It is these pronounced changes in their properties upon application of a magnetic field that make diluted magnetic semiconductors a key component to the realization of semiconductor spin-based electronic devices[39]. Currently, there are a number of existing theoretical models that attempt to explain the observed magnetism in diluted magnetic semiconductors. Dietl *et al.* have applied the Zener model of ferromagnetism to various II-VI and III-V semiconductors doped with Mn cations. Their results suggested that above room temperature ferromagnetism can be achieved in ZnO and GaN doped with 5% Mn cations given that the semiconductor also contained a sufficiently high hole concentration of 3.5×10^{20} cm^{-3}.[37,40] It is uncertain, however, if such a hole concentration can be achieved in either of these semiconductors. While high concentrations of *n*-doping can be accomplished in both semiconductors, high concentration of *p*-doping is considered quite difficult due to such factors as low solubility limits of the hole dopant in the semiconductor, the hole dopant forming a deep acceptor in the semiconductor bandgap, or self compensation by intrinsic shallow donor defects in the semiconductor.[37,41,42] Experimental work done on GaMnN suggested that the difficulty in *p*-type doping of GaN may be attributed to the Mn level being a deep acceptor in GaN, thus making the Mn an ineffective acceptor.[43,44] In the

case of ZnO, substituting Mn^{2+} with Zn^{2+} ions in the ZnO lattice does not lead to any introduction of carriers. But *p*-doping have been achieved in ZnO by introducing group V elements (such as N).[41,42,45] The hole concentration, however, was only $\sim 10^{16}$ cm^{-3} (refs. [41,45]) and therefore order of magnitudes smaller than the 3.5×10^{20} cm^{-3} suggested by Dietl *et al.* as being necessary for achieving above room temperature ferromagnetism.

Ferromagnetism in 3*d* transition metal doped ZnO has also been theoretically investigated by *ab initio* calculations based on local density approximations by Sato *et al.* Their results showed that under the condition of no additional carrier dopants, the anti-ferromagnetic state was stable in Mn^{2+}-doped ZnO, whereas the ferromagnetic state was stable for ZnO doped with V^{2+}, Cr^{2+}, Fe^{2+}, Co^{2+}, or Ni^{2+} with transition metal dopant concentration ranging from 5 to 25%.[46-49] Furthermore, the calculations of Sato *et al.* showed that ferromagnetism was induced in Mn^{2+}-doped ZnO with hole doping, agreeing with Dietl's prediction. Similarly, using density functional theory/local density approximation Spaldin *et al.* concluded that *p*-type Mn^{2+}-doped ZnO should exhibit ferromagnetism, however, contrary to the calculated results of Sato *et al.* they also concluded that *p*-type Co^{2+}-doped ZnO should exhibit ferromagnetism.[50] Coey *et al.* used a spin-split donor impurity-band model to explain the observed above room temperature ferromagnetism in ZnO films doped with 5% of

Sc, Ti, V, Fe, Co, or Ni, but an absence of ferromagnetism when doped with Cr, Mn, or Cu.[30,51]

With all these numerous theoretical models, it would appear that the ferromagnetism in diluted magnetic semiconductors is well described and fully understood, however, there are limitations to each model as well as inconsistencies between some of the theoretical predictions. Dietl's *et al.* predications based on the Zener model is specifically for *p*-type materials, Coey's *et al.* spin-split donor impurity-band model does not explicitly account for the observed ferromagnetism in *p*-type Mn^{2+}-doped ZnO, and the results of *ab initio* local density approximation and density functional theory predictions of ferromagnetism as to whether it depends on holes or electrons appear to be inconsistent as mentioned above for the case of Co^{2+}-doped ZnO. Therefore, it is prudent to gain insight into the microscopic material properties essential for high Curie temperature ferromagnetism in order to effectively direct the development of new materials. In Chapter 3, a detailed model based on the energies of donor- and acceptor-type excited states is presented to explain and predict both *p*- and *n*-type ferromagnetism in diluted magnetic oxide semiconductors.

Although the aforementioned models and theoretical predications differ in their approaches to explaining ferromagnetism in diluted magnetic semiconductors, they all assert that carriers (holes or electrons) are needed. It is under that premise that in Chapter 4 the exchange coupling between the magnetic dopant cations and intentionally added quantum confined electrons in paramagnetic colloidal Mn^{2+}- and

Co^{2+}-doped ZnO quantum dots is investigated. The findings in Chapter 4 are relevant to the overall field of semiconductor spin-based electronics where interest in manipulating and controlling semiconductor spins for use in applications ranging from spin polarized magneto-electrical and magneto-optical devices (such as spin field effect transistor[52] and spin light emitting diode[53,54]) to quantum computers[55].

Spin transport/injection (transferring spin polarized current into an otherwise nonmagnetic semiconductor) is important, however, it is not the only prerequisite for successful implementation of spin-based devices. The spin polarized carriers in these materials must also exhibit sufficiently long spin coherence time.[56] The spin relaxation or coherence times are characterized by T_1 and T_2, which represent the decay of longitudinal and transverse spin order, respectively.[57] In the simplest and most basic two state system containing a population of spin $\pm\frac{1}{2}$ electrons at thermal equilibrium in an external magnetic field, a nonequilibrium perturbation to the system can lead to (i) a change in the relative population of the two states, and (ii) a change in the coherence or phase relationship between the two states.[56] For case (i) the two state system must eventually return (relax) to the original Boltzmann distribution when the cause of the nonequilibrium perturbation is removed. It can do so by coupling to phonons and this relaxation is described by the time T_1 (spin-lattice relaxation or longitudinal magnetization decay time). Similarly for case (ii), decoherence of the spins by direct interactions with nearby magnetic dipoles is described by T_2 (spin-spin relaxation or transverse magnetization decay time).[56] Generally, $T_2 \leq T_1$ such that T_2 is

the more relevant quantity for coherent spin-based devices.[56] The spin decoherence time has been investigated for various II-VI and III-V semiconductors of bulk single crystals, epitaxial thin films, and quantum dots using time resolve Faraday rotation spectroscopy, or luminescence pump-probe and Hanle measurements.[58-65] In Chapter 4, the spin decoherence time is determined by electron paramagnetic resonance spectroscopy for colloidal ZnO quantum dots containing additional quantum confined conduction band electrons.

1.2 Notes to Chapter 1

[1] U.S. Department of Energy: Energy Information Administration, *International Energy Outlook 2007*; Washington, DC, DOE/EIA-0484 (2007).

[2] Raupach, M. R.; Marland, G.; Ciais, P.; Le Quere, C.; Canadell, J. G.; Klepper, G., *Proc. National Academy of Sciences* **2007**, *104*, 10288.

[3] Marzec, A., *Pol. J. Appl. Chem.* **2002**, *46*, 143.

[4] Eisenberg, R.; Nocera, D. G., *Inorg. Chem.* **2005**, *44*, 6799.

[5] Fernandez, N.; Cesar, A.; Gonzalez, M.; DelValls, T. A., *Ciencias Marinas* **2006**, *32*, 421.

[6] Soriano, J. A.; Vinas, L.; Franco, M. A.; Gonzalez, J. J.; Ortiz, L.; Bayona, J. M.; Albaiges, J., *Sci. Total Environ.* **2006**, *370*, 80.

[7] Chukwu, L. O.; Nwachukwu, S. C. U., *J. Environ. Bio.* **2005**, *26*, 449.

[8] Osuji, L. C.; Adesiyan, S. O., *Chem. & Biodiversity* **2005**, *2*, 1079.

[9] Moreira, S. M.; Moreira-Santos, M.; Ribeiro, R.; Guilhermino, L., *Ecotoxicol.* **2004**, *13*, 619.

[10] Law, R. J.; Kelly, C., *Aqua. Living Res.* **2004**, **17**, 389.

[11] Lee, K.; Prince, R. C.; Greer, C. W.; Doe, K. G.; Wilson, J. E. H.; Cobanli, S. E.; Wohlgeschaffen, G. D.; Alroumi, D.; King, T.; Tremblay, G. H., *Spill Sci. & Technol. Bull.* **2003**, *8*, 187.

[12] Fernley, P. W.; Moore, M. N.; Lowe, D. M.; Donkin, P.; Evans, S., *Mar. Environ. Res.* **2000**, *50*, 451.

[13] Madan, A., *Indian J. Environ. Protection* **1988**, *8*, 687.

[14] Honda, K.; Fujishima, A., *Nature* **1972**, *238*, 37.

[15] Mavroides, J. G.; Kafalas, J. A.; Kolesar, D. F., *Appl. Phys. Lett.* **1975**, *28*, 241.

[16] Zou, Z.; Ye, J.; Sayama, K.; Arakawa, H., *Nature* **2001**, *414*, 625.

[17] Kudo, A.; Sekizawa, M., *Catal. Lett.* **1999**, *58*, 241.

[18] Zou, Z.; Ye, J.; Sayama, K.; Arakawa, H., *J. Photochem. Photobiol., A* **2002**, *148*, 65.

[19] Iwasaki, M.; Hara, M.; Kawada, H.; Tada, H.; Ito, S., *J. Colloid Interface Sci.* **2000**, *224*, 202.

[20] Kobayashi, K.; Maeda, T.; Matsushima, S.; Okada, G., *J. Mater. Sci.* **1992**, *27*, 5953.

[21] Jaramillo, T. F.; Baeck, S.-H.; Kleiman-Shwarsctein, A.; Choi, K.-S.; Stucky, G. D.; McFarland, E. W., *J. Comb. Chem.* **2005**, *7*, 264.

[22] Bahadur, L.; Rao, T. N.; Pandey, J. P., *Semicond. Sci. Technol.* **1994**, *9*, 275.

[23] Kobayashi, K.; Maeda, T.; Matsushima, S.; Okada, G., *Jpn. J. Appl. Phys.* **1992**, *31*, L1079.

[24] Bahadur. L.; Rao, T. N., *Sol. Energy Mater. Sol. Cells* **1992**, *27*, 347.

[25] Fichou, D.; Pouliquen, J.; Kossanyi, J.; Jakani, M.; Campet, G.; Claverie, J., *J. Electroanal. Chem.* **1985**, *188*, 167.

[26] Jakani, M.; Campet, G.; Claverie, J.; Fichou, D.; Pouliquen, J.; Kossanyi, J., *J. Solid State Chem.* **1985**, *56*, 269.

[27] Schwartz, D. A.; Norberg, N. S.; Nguyen, Q. P.; Parker, J. M.;Gamelin, D. R., *J. Am. Chem. Soc.* **2003**, *125*, 13205.

[28] Weakliem, H. A., *J. Chem. Phys.* **1962**, *36*, 2117.

[29] Pearton, S. J.; Heo, W. H.; Ivill, M.; Norton, D. P.; Steiner, T., *Semicond. Sci. Technol.* **2004**, *19*, R59.

[30] Venkatesan, M.; Fitzgerald, C. B.; Lunney, J. G.; Coey, J. M. D., *Phys. Rev. Lett.* **2004**, *93*, 177206.

[31] Saeki, H.; Tabata, H.; Kawai, T., *Solid State Commun.* **2001**, *20*, 439.

[32] Matsumoto, Y.; Murakami, M.; Shono, T.; Hasegawa, T.; Fukumura, T.; Kawasaki, M.; Ahmet, P.; Chikyow, T.; Koshihara, S.; Koinuma, H., *Science* **2001**, *291*, 854.

[33] Ivill, M.; Pearton, S. J.; Norton, D. P.; Kelly, J.; Hebard, A. F., *J. Appl. Phys.* **2005**, *97*, 053904.

[34] Ueda, K.; Tabata, H.; Kawai, T., *Appl. Phys. Lett.* **2001**, *79*, 988.

[35] Schwartz, D. A.; Gamelin, D. R., *Adv. Mater.* **2004**, *16*, 2115

[36] Radovanovic, P. V.; Gamelin, D. R., *Phys. Rev. Lett.* **2003**, *91*, 157202.

[37] Liu, C.; Yun, F.; Morkoc, H., *J. Mater. Sci. Mater. Electron.* **2005**, *16*, 555.

[38] Furdyna, J. K., *J. Appl. Phys.* **1988**, *64*, R29.

[39] Wolf, S. A.; Awschalom, D. D.; Buhrman, R. A.; Daughton, J. M.; von Molnar, S.; Roukes, M. L.; Chtchelkanova, A. Y.; Treger, D. M., *Science* **2001**, *294*, 1488.

[40] Dietl, T.; Ohno, H.; Matsukura, F.; Cibert, J.; Ferrand, D., *Science* **2000**, *287*, 1019.

[41] Pearton, S. J.; Norton, D. P.; Ip, K.; Heo, Y. W.; Steiner, T., *Superlattices Microstruct.* **2003**, *34*, 3.

[42] Park, C. H.; Zhang, S. B.; Wei, S. H., *Phys. Rev. B* **2002**, *66*, 073202.

[43] Pearton, S. J.; Abernation, C. R.; Norton, D. P.; Hebard, A. F.; Park, Y. D.; Boatner, L. A.; Budai, J. D., *Mater. Sci. Eng., R* **2003**, *40*, 137.

[44] Korotkov, R. Y.; Gregie, J. M.; Wessels, B. W., *Appl. Phys. Lett.* **2002**, *80*, 1731.

[45] Look, D. C.; Claflin, B., *Phys. Status Solidi B* **2004**, *241*, 624.

[46] Sato, K.; Katayama-Yoshida, H., *Semicond. Sci. Technol.* **2002**, *17*, 367.

[47] Sato, K.; Katayama-Yoshida, H., *Physica E* **2001**, *10*, 251.

[48] Sato, K.; Katayama-Yoshida, H., *Physica B* **2001**, *308-310*, 904.

[49] Sato, K.; Katayama-Yoshida, H., *Jpn. J. Appl. Phys.* **2001**, *40*, L334.

[50] Spaldin, N. A., *Phys. Rev. B* **2004**, *69*, 125201.

[51] Coey, J. M. D.; Venkatesan, M.; Fitzgerald, C. B., *Nature Mater.* **2005**, *4*, 173.

[52] Datta, S.; Das, B, *Appl. Phys. Lett.* **1990**, *56*, 665.

[53] Fiederling, R.; Keim, M.; Reuscher, G.; Ossau, W.; Schmidt, G.; Waag, A.; Molenkamp L. W., *Nature* **1999**, *402*, 787.

[54] Ohno, Y.; Young, D. K.; Beschoten, B.; Matsukura, F.; Ohno, H.; Awschalom, D. D., *Nature* **1999**, *402*, 790.

[55] Loss, D.; DiVincenzo, D. P., *Phys. Rev. A* **1998**, *57*, 120.

[56] Awschalom, D. D.; Loss, D.; Samarth, N., *Semiconductor Spintronics and Quantum Computation*; Springer: New York, 2002.

[57] Lau, W. H.; Olesberg, J. T.; Flatté, M. E., *Phys. Rev. B* **2001**, *64*, 161301(R).

[58] Kikkawa, J. M.; Smorchkova, I. P.; Samarth, N.; Awschalom, D. D., *Science* **1997**, *277*, 1284.

[59] Kikkawa, J. M.; Awschalom, D. D., *Phys. Rev. Lett.* **1998**, *80*, 4313.

[60] Beschoten, B.; Johnston-Halperin, E.; Young, D. K.; Poggio, M.; Grimaldi, J. E.; Keller, S.; DenBaars, S. P.; Mishra, U. K.; Hu, E. L.; Awschalom, D. D., *Phys. Rev. B* **2001**, *63*, 121202(R).

[61] Gupta, J. A.; Awschalom, D. D.; Peng, X.; Alivisatos, A. P., *Phys. Rev. B* **1999**, *59*, 10421(R).

[62] Ghosh, S.; Sih, V.; Lau, W. H.; Awschalom, D. D., *Appl. Phys. Lett.* **2005**, *86*, 232507.

[63] Kikkawa, J. M.; Gupta, J. A.; Malajovich; Awschalom, D. D., *Physica E* **2001**, *9*, 194.

[64] Gupta, J. A.; Awschalom, D. D.; Efros, A. L., *Phys. Rev. B* **2002**, *66*, 125307.

[65] Masumoto, Y.; Pal, B.; Oguchi, S.; Ikezawa, M., arXiv:cond-mat/0608046v1

Chapter 2: Spectroscopy of Photovoltaic and Photoconductive Nanocrystalline Co^{2+}:ZnO Electrodes

In this chapter, I demonstrate that photocurrent and photoconductivity measurements can be used in combination with absorption and magnetic circular dichroism (MCD) spectroscopic measurements to elucidate the mechanism of photoinduced carrier generation in nanocrystalline Co^{2+}:ZnO electrodes. The experiments presented here allow for direct observation of two broad Co^{2+} charge transfer (CT) bands extending throughout the visible energy range. The observed difference in the internal quantum efficiencies between these two charge transfer excitations is explain by the differences in excited-state wave functions arising from configuration interaction with the *1S* excitonic levels of ZnO. In addition, practical factors controlling the overall photovoltaic efficiencies of the photoelectrochemical cells, including electrode conductivity and porosity, are examined.

2.1 Introduction

Doping with transition metal impurities has been widely investigated as a strategy for extending the photoresponse of wide bandgap oxide semiconductors into the visible spectral range, thereby making them suitable candidates for photochemical conversion of solar energy into electrical or chemical potential.[1-5] Recently, for example, direct hydrogen production by $InTaO_4$ was observed with visible irradiation when Ni^{2+} dopants were introduced as colored impurities.[1] The photochemistry was reported to proceed via excitation of a sub-bandgap absorption feature attributed by

the authors to a Ni^{2+} *d-d* transition. Similarly, H_2 production from H_2O has been observed with low-energy Co^{2+} *d-d* excitation in Co^{2+}-doped zinc oxide (Co^{2+}:ZnO) photoelectrochemical probes,[2] and visible Cr^{3+} ligand field excitation in Cr^{3+}/Sb^{5+} codoped TiO_2 was reported to induce O_2 evolution from an aqueous silver nitrate solution.[3] In the above examples, it is unclear how ligand field excitation can induce electron-hole separation to generate the observed photocatalytic activity in these transition metal doped semiconductors, given that the ligand field excitations are highly localized at the transition metal impurity centers.[1]

In many regards, Co^{2+}:ZnO is the archetypical dopant-sensitized wide bandgap semiconductor. The visible photoresponse of Co^{2+}:ZnO has been observed by several groups using single crystals[6] or polycrystalline Co^{2+}:ZnO prepared by pellet sintering,[7] spray pyrolysis,[8] sol-gel coating,[9] electrodeposition,[2] or radio frequency sputtering.[10,11] In most cases, the photoresponse was found to extend throughout the visible energy range, with a photoanodic current excited between 14000 and 18000 cm^{-1} that was clearly attributable to the $^4A_2 \rightarrow {}^4T_1(P)$ *d-d* transition of the Co^{2+} dopant. Previous analyses have led to proposals that Co^{2+}:ZnO photocurrent occurs via thermal electron emission[10,11] from the $^4T_1(P)$ excited state, or relaxation of the $^4T_1(P)$ excited state to a lower energy photoionized state,[7] but the proposed photoionization level has itself never been detected directly. Additionally, Co^{2+} doping also enhances photocurrent generation with near-ultraviolet excitation, reportedly by

shifting the onset of the ZnO absorption band edge to lower energies,[12] but the origins of the near-edge absorption intensity have not been adequately investigated. Some researchers have attributed the apparent decrease in the ZnO absorption edge energy to an increase in the valence band energy upon Co^{2+} doping,[2] whereas others have suggested that this near-edge absorption intensity results from promotion of a Co^{2+} d_e electron into the conduction band[9] or from transitions involving other defects in the bulk material.[7]

In this chapter, we use photovoltaic and photoconductive device structures to obtain high quality photocurrent action spectra for nanocrystalline Co^{2+}:ZnO thin film electrodes. These photocurrent and photoconductivity measurements as well as absorption and magnetic circular dichroism (MCD) spectroscopic measurements all show evidence for the existence of broad Co^{2+}-based charge-transfer (CT) transitions extending throughout the visible energy range and, in particular, overlapping the $^4A_2 \rightarrow {}^4T_1(P)$ ligand field absorption band at ca. 14000 cm^{-1}. The lowest energy CT transition is assigned as a $Co^{2+} \rightarrow$ conduction band ($ML_{CB}CT$) excitation, and a higher energy CT transition involving electron promotion from the valence band to Co^{2+} ($L_{VB}MCT$) is also observed. Sensitization of the $Co^{2+} \rightarrow$ conduction band CT by ligand field excitation is concluded to be responsible for the distinct structured photocurrent action spectrum of these electrodes in the visible energy range. The different internal quantum efficiencies for charge separation measured for the two CT excited states are related to differences in intrinsic escape probabilities for

photogenerated electrons and holes by consideration of configuration interaction with the *1S* excitonic excited states. Practical factors controlling the overall efficiencies of the photoelectrochemical cells, including electrode conductivity and porosity, have also been examined.

The detailed spectroscopic and spectroelectrochemical description of this archetypical doped wide bandgap semiconductor provides a basis for understanding related doped oxide semiconductors currently under investigation for photocatalysis and solar energy conversion. In a broader context, the charge transfer electronic structural information obtained from these measurements is extremely valuable in understanding the physical properties of doped oxide semiconductors in general, and the high Curie temperature ferromagnetism recently discovered in some of the same doped oxide semiconductors,[13,14] including Co^{2+}:ZnO.[15-20]

2.2 Experimental

2.2.1 Synthesis of Co^{2+}:ZnO Nanocrystals

Colloidal nanocrystals of Co^{2+}:ZnO were prepared as described previously[20] with minor modifications. Briefly, in a typical preparation, an ethanolic solution of 0.552 M tetramethylammonium hydroxide pentahydrate ($N(CH_3)_4OH{\cdot}5H_2O$, 97%, Sigma-Aldrich) was added dropwise at a rate of ~2 mL/min to a dimethyl sulfoxide (DMSO, 99.7%, Acros) solution of 96 mM zinc acetate dihydrate ($Zn(OAc)_2{\cdot}2H_2O$, 98%, Strem) and 5 mM cobalt acetate tetrahydrate ($Co(OAc)_2{\cdot}4H_2O$, 99.8%, GFS Chemical) under vigorous stirring at room temperature. The reaction mixture was then

heated at 333 K under constant stirring to promote nanocrystal growth. Subsequently, the nanocrystals were precipitated from the DMSO by addition of ethyl acetate, collected, and resuspended in ethanol. The colloids were then reprecipitated and washed with heptane. For one set of experiments, the nanocrystals at this stage were resuspended in a minimal amount of ethanol and used for spin coating directly as prepared. For a second set of experiments, dodecylamine ($CH_3(CH_2)_{11}NH_2$, 98%, Sigma-Aldrich) was added and the suspension was heated at 453 K for at least 30 minutes to yield dodecylamine capped nanocrystals.[17,21] The dodecylamine capped nanocrystals were cooled, precipitated, and washed with ethanol, and then resuspended in toluene for spin coating. For the third set of experiments the colloids were capped with trioctylphosphine oxide (TOPO, $(CH_3(CH_2)_7)_3PO$, 90%, Sigma-Aldrich) instead of dodecylamine, again yielding high-optical-quality colloidal suspensions of the nanocrystals in toluene. For clarity, samples prepared in these three ways are hereafter referred to as (1) Co^{2+}:ZnO(OH^-), (2) Co^{2+}:ZnO(amine), and (3) Co^{2+}:ZnO(TOPO), respectively.

2.2.2 Preparation of Nanocrystalline Co^{2+}:ZnO Electrodes

Electrodes of Co^{2+}:ZnO were prepared by spin coating colloidal Co^{2+}:ZnO onto indium tin oxide (ITO) coated glass (2.5×1.3 cm^2, Delta Technologies, R_s = 70-100 Ω). Electrical tape was used to mask off a 5 mm strip at one edge of the ITO to ensure direct electrical contact could be made later. The electrode was heated at 723 K in air for 1-2 minutes after each layer was added. After the last layer was applied, the

films were annealed aerobically at 723 K for 1 hour to induce particle sintering and to calcine the remaining organic solvents or surface ligands.[22]

For some experiments, 1-2 drops of a polystyrene sphere (PS) suspension (85 ± 5 nm, PolySciences Inc., 4.55×10^{13} particles/mL) were added to 2.0 mL of the concentrated ethanol Co^{2+}:ZnO colloidal suspension. The mixture was sonicated for 10 minutes and spin coated onto ITO as described above. The polystyrene spheres were then calcined during annealing. Such films are denoted by the label "PS". For other experiments, nanocrystalline Co^{2+}:ZnO electrodes were sealed along with 20-25 mg tin metal (Sn) pellets in evacuated borosilicate tubes and annealed at 773 K for 15-180 minutes. There was no physical contact between the sample and the Sn pellets. The sealed test tubes were cooled to room temperature prior to breaking the vacuum. For clarity, films annealed with Sn metal are labeled with the postscript "Sn" (e.g., Co^{2+}:ZnO(Sn-PS) for a Co^{2+}:ZnO film prepared with PS during spin coating and also annealed in the presence of Sn).

2.2.3 Assembly of Co^{2+}:ZnO Photovoltaic Cells

Two-electrode photovoltaic cells were constructed in Grätzel's configuration[23,24] using the nanocrystalline Co^{2+}:ZnO/ITO films as the working electrodes (WE). For counter electrodes (CE), platinized ITO electrodes were prepared by spin coating a 2-propanol solution of 10 mM chloroplatinic acid hexahydrate ($H_2Pt(Cl)_6{\cdot}6H_2O$, 99.9%, Strem Chemicals Inc.) onto cleaned pieces of ITO-coated glass and heating to 658 K for 15 minutes in a tube furnace open to air.[25] Prior to use,

the platinized ITO electrodes were rinsed with ethanol and dried in nitrogen gas. A ~6 mm diameter aperture was prepared from electrical tape and adhered to the CE. The shallow well formed by the electrical tape was filled with an electrolyte solution of 0.5 M LiI/0.05 M I_2 in propylene carbonate.[25] The WE and CE were then sandwiched together at an offset and secured with binding clips.[23,24] Strips of copper tape with a conductive adhesive (*L*-Com Connectivity Products) were placed onto the exposed ITO surfaces of both electrodes for electrical contacts.

2.2.4 Physical Measurements

Cobalt concentrations in Co^{2+}:ZnO samples were determined by inductively coupled plasma atomic emission spectrometry (ICP-AES, Jarrel Ash model 995). Film thicknesses were measured using an Alpha Step 500 contact probe surface profilometer. Scanning electron microscopy (SEM) images were collected on an FEI Serion XL30 field emission electron microscope. Electronic absorption spectra were collected using a Cary 5E spectrophotometer (Varian). Magnetic circular dichroism spectra were collected as described previously.[20] Short circuit currents were measured using a μAutolab Type II potentiostat (Eco Chemie B.V.). An Aviv 40DS spectropolarimeter equipped with a 350 W xenon lamp was used as the illumination source to collect photocurrent action spectra. Excitation intensities over the wavelength range of the experiment were measured using a calibrated silicon photodiode. All photocurrent measurements were performed by illumination through the WE. Room temperature film resistance measurements were performed using an

in-line four-point probe (Lucas/Signatone Corp.). Due to the high resistivities of the films, sheet resistance values could not be determined accurately and only film resistance values are reported.

2.2.5 Photoconductivity and Vapor Sensing

An ~100 μm channel was etched into a piece of ITO using concentrated HCl. The width of the channel was determined using a reflective microscope. The channel was then filled with a spin-coated film of Co^{2+}:ZnO nanocrystals as described above. A 100 V DC bias was applied across the film and the dark current and photocurrent were measured while the film was enclosed in flowing atmospheres of vapor from various solvents including H_2O (HPLC grade), pentane, toluene, and methanol, with argon as the carrier gas, or under vacuum or ambient air. Each of the solvents was degassed by the freeze-pump-thaw method prior to use, and the methanol was distilled from $I_2/Mg_{(s)}$.[26] The illumination source was an unfocused 20 W tungsten halogen lamp.

2.3 Results and Discussion

Figure 2.3.1(a) shows a schematic of the Co^{2+}:ZnO photovoltaic cell assembly. A color photograph of an assembled cell is shown in Figure 2.3.1(b). Figure 2.3.1(c) shows an SEM image of a representative 3% Co^{2+}:ZnO(OH^-) nanocrystalline electrode. Extensive sintering of the nanocrystals during calcination yields a highly porous but continuous network of interconnected grains in these films. As shown in Figure 2.3.1(d), addition of 85 ± 5 nm diameter polystyrene spheres during spin coat

processing increased the film porosity substantially, with roughly twice the vacant volume relative to Figure 2.3.1(c). Note that the film thicknesses (ca. 4 μm) are ~13 times greater than the widths of the areas imaged in Figure 2.3.1(c),(d).

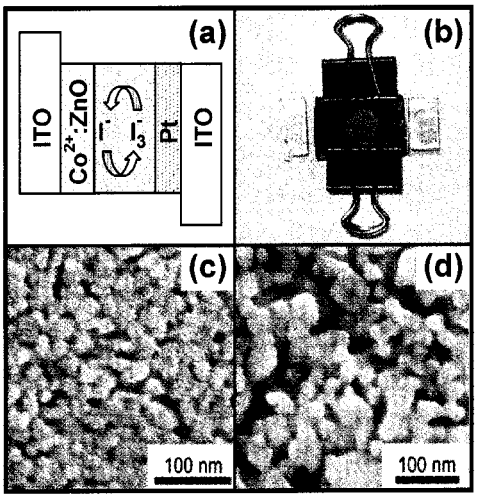

Figure 2.3.1. (a) Schematic of the Co^{2+}:ZnO regenerative photovoltaic cell. **(b)** Photograph of the assembled cell. SEM images of ca. 4 μm thick nanocrystalline 3% Co^{2+}:ZnO films prepared from solutions of Co^{2+}:ZnO(OH^-) **(c)** without and **(d)** with added polystyrene spheres (Co^{2+}:ZnO(PS)).

Figure 2.3.2(a) compares the 300 K electronic absorption spectrum of a representative 4 μm thickness 3% Co^{2+}:ZnO(amine) film (dashed) to the photocurrent action spectrum of the same film incorporated into a regenerative photovoltaic cell (solid line). The absorption spectra of all Co^{2+}:ZnO films were essentially identical with the one shown in Figure 2.3.2(a). The absorption spectrum in Figure 2.3.2(a) is dominated in the visible by the prominent spin-orbit-split $^4A_2 \rightarrow {}^4T_1(P)$ ligand field band (~16400 cm^{-1}) characteristic of Co^{2+} in the trigonally distorted tetraoxo cation coordination environment of wurtzite ZnO.[20,27] The lower energy $^4A_2 \rightarrow {}^4T_1(F)$ ligand

field band was also observed (the transition is not shown Figure 2.3.2 since it occurs centered at ~7000 cm^{-1}).[27] The Co^{2+}:ZnO photocurrent action spectrum, represented as incident photon-to-current conversion efficiency (IPCE)[23] as defined in Eqn. 2.3.1, follows the Co^{2+}:ZnO absorption spectrum closely throughout the entire spectral range shown.

$$IPCE(\%) = \frac{(1.24\times10^{3})\, i_{sc}\,(\mu A/cm^{2})}{\lambda(nm)\times\gamma_{inc}\,(W/m^{2})} \qquad \text{Eqn. [2.3.1]}$$

Increasing the excitation energy from the near infrared, photocurrent was first observed at ca. 14000 cm^{-1}, coinciding with the onset of Co^{2+} $^4A_2 \rightarrow {}^4T_1(P)$ absorption. Above the $^4A_2 \rightarrow {}^4T_1(P)$ threshold, photocurrents were observed with excitation throughout the rest of the visible and ultraviolet energy region up to 25000 cm^{-1}, the experimental limit imposed by the onset of I_3^- absorbance.[28] Solvent vibrational overtones occluded the lower energy ligand-field absorption bands in the photovoltaic cell, but the absence of photoactivity with excitation into these bands was verified by the absence of detectable photoconductivity in the solventless etched-channel photocurrent device configuration (*vide infra*). All Co^{2+}:ZnO photovoltaic cells exhibited photocurrent action spectra similar to that presented in Figure 2.3.2, which itself generally agrees with photoconductivity data reported previously for polycrystalline Co^{2+}:ZnO produced by spray pyrolysis[8] or pellet sintering[7]. A significant difference in peak IPCE values was observed when comparing Co^{2+}:ZnO(OH^-) and Co^{2+}:ZnO(amine) electrodes, however, with the former

consistently performing better (see Figure 2.3.3). Thicker Co^{2+}:ZnO nanocrystalline films also yielded higher IPCE values. Figure 2.3.2(b) reports the action spectra of

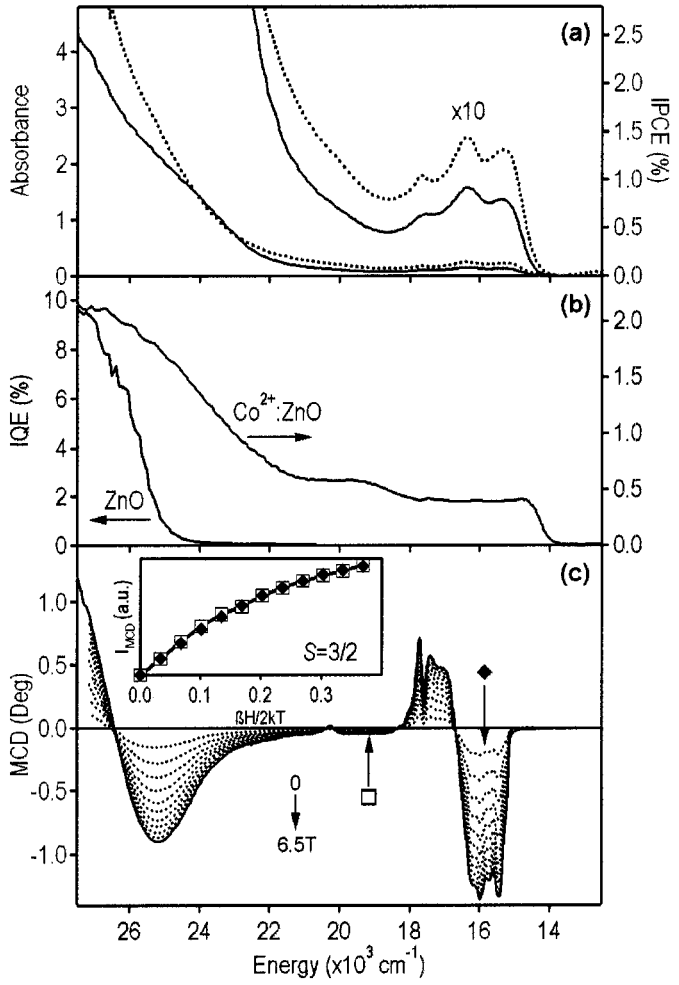

Figure 2.3.2. (a) Absorption (dotted line) and photocurrent action (solid line) spectra of the 4.1 μm thick 3% Co^{2+}:ZnO(amine) nanocrystalline photoanode. The absorption spectrum was taken prior to cell assembly. **(b)** Photocurrent internal quantum efficiency (IQE) for the Co^{2+}:ZnO photovoltaic cell from part (a), compared with the analogous undoped ZnO photovoltaic cell. **(c)** Variable-field (5 K, 0-6.5 T) MCD spectra of a frozen solution of 5 nm diameter 1.7% Co^{2+}:ZnO nanocrystals. Adapted from ref. [20] (MCD was collected by Dr. Dana Schwartz). **Inset:** 5 K MCD saturation magnetization data collected for the bands at 19300 (□) and 15800 cm^{-1}(♦).

Co^{2+}:ZnO and ZnO photovoltaic cells converted to internal quantum efficiencies (*vide infra*).

Figure 2.3.2(c) shows 5 K MCD spectra collected for colloidal Co^{2+}:ZnO nanocrystals prepared in the same way as those used to make the photovoltaic cells. The spectra are presented as a function of applied magnetic field, showing increased MCD intensities with increasing applied fields as illustrated in the inset for the two probe energies labeled in the figure.

Figure 2.3.3 shows the transient photocurrent responses (I vs t) for representative Co^{2+}:ZnO(OH^-) and Co^{2+}:ZnO(amine) films when assembled into photovoltaic cells, with irradiation at 400, 500, and 610 nm. There was no detectable photocurrent for illumination energies <~13000 cm^{-1}. Both photovoltaic cells responded rapidly to illumination, requiring less than ca. 10 seconds to reach steady state for both "on" and "off" steps. In contrast to the Co^{2+}:ZnO(OH^-) and Co^{2+}:ZnO(amine) cells, photovoltaic cells prepared from TOPO-capped Co^{2+}:ZnO nanocrystals showed negligible photocurrent when illuminated at 500 or 610 nm and only very weak photocurrent at 400 nm (data not shown), and consequently, no further experiments were done using TOPO-capped nanocrystals.

Figure 2.3.4(a) shows the steady-state photocurrent of a 3% Co^{2+}:ZnO film (inset) under a 100 V applied bias and broadband illumination using an unfocused 20 W tungsten halogen lamp, before and after evacuation of the chamber encasing the film. Under ambient atmospheric conditions, photocurrents were detected with visible

excitation with a response mimicking that of the regenerative photovoltaic cell (Figure 2.3.2(a)). Broadband excitation using the same unfocused 20 W tungsten halogen lamp and a near infrared long-pass cutoff filter verified the absence of photocurrent with excitation into the low-energy $^4T_1(F)$ and $^4T_2(F)$ ligand field excited states that occur below 10000 cm^{-1}. As shown in Figure 2.3.4(a), the photocurrent measured with

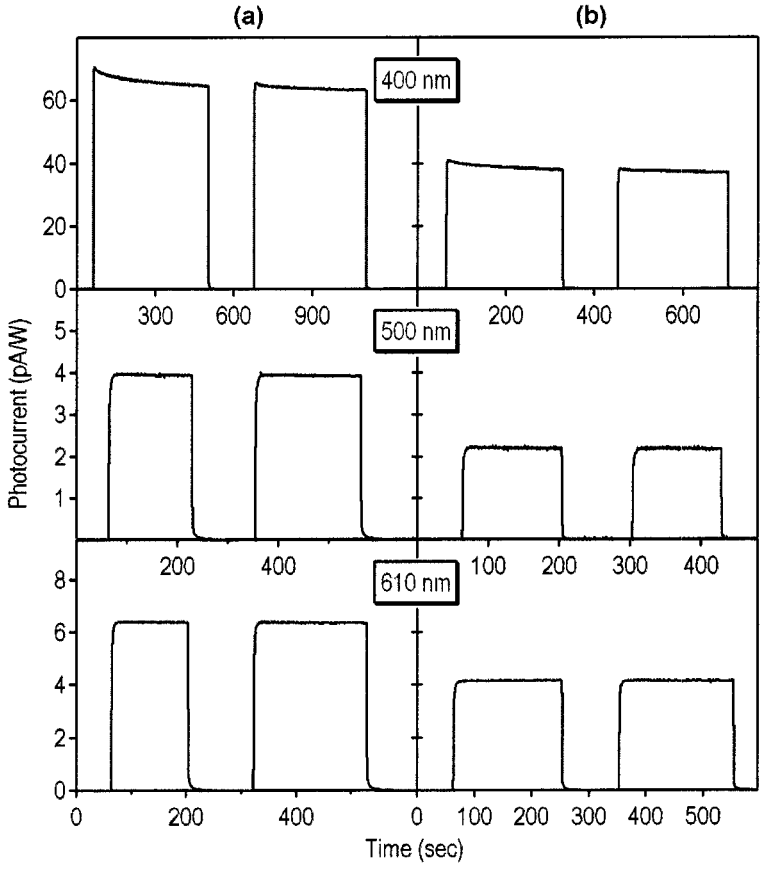

Figure 2.3.3. Transient photocurrent response curves collected with 400, 500, and 610 nm monochromatic excitation for **(a)** 3% Co^{2+}:ZnO(OH^-) and **(b)** 3% Co^{2+}:ZnO(amine) photovoltaic cells. The data have been corrected for the power output of the illumination source at the specified wavelength.

this device was rapidly quenched upon evacuation of the chamber encasing the film. Figure 2.3.4(b) shows the dark-current and photocurrent (broadband illumination with an unfocused 20 W tungsten halogen lamp) responses of the same film exposed to different solvent vapors at 298 K. For a vacuum or vapors of pentane or toluene, the dark current was negligible. Under illumination, the currents increased by a factor of

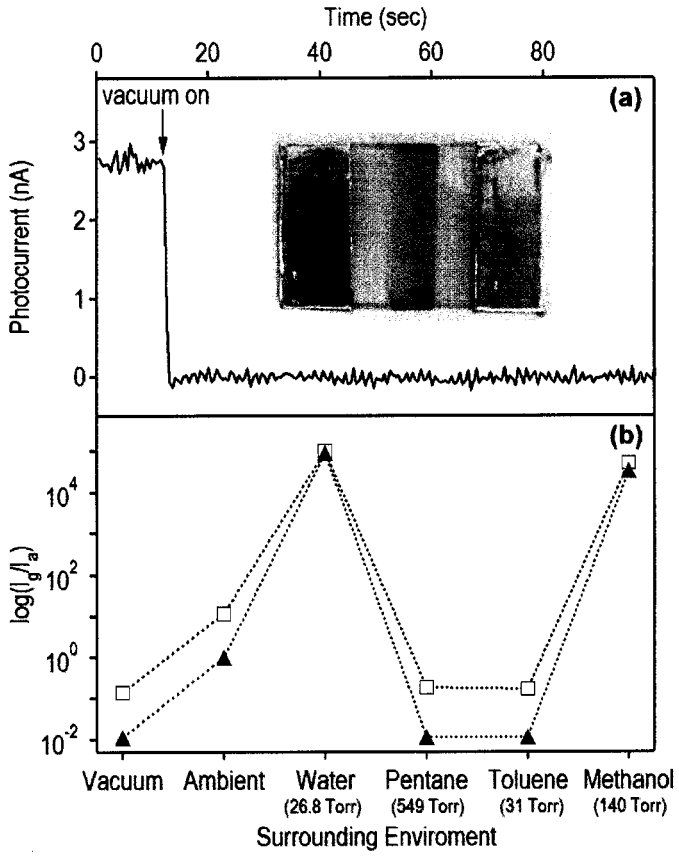

Figure 2.3.4. (a) The effect of a vacuum on the photoconductivity of a 3% Co^{2+}:ZnO(OH^-) nanocrystalline film under a 100 V bias. **Inset:** photograph of a thin film on ITO electrodes. **(b)** The dark-current responses (▲) and photocurrent responses (□) of a 3% Co^{2+}:ZnO nanocrystalline film under a 100 V bias, exposed to various solvent vapors, and plotted as the log of the measured current (I_g) relative to the dark current under ambient conditions (I_a). An unfocused 20 W tungsten halogen lamp was used for illumination.

10 each. In contrast, the dark currents for the same film under vapors of methanol, water, or ambient air were orders of magnitude larger, with water being the highest (128 μA). An increase in current was also observed upon illumination in each case (note the logarithmic *y*-scale in Figure 2.3.4(b)).

The resistances of the as-prepared nanocrystalline Co^{2+}:ZnO films were all beyond the upper limit of our detection capabilities (>10^9 Ω). Heating the films in evacuated glass tubes at 773 K in the presence of Sn metal improved film conductivities significantly relative to those heated aerobically, with no discernible changes in the Co^{2+}:ZnO absorption spectrum. These data are summarized in Table 2.3.1, which also reports the relative areas of the internal quantum efficiency curves (*vide infra*) integrated between 14000 and 21550 cm^{-1}. Although the absorption

Table 2.3.1. Summary of Relative Photocurrent IQEs* for Various Nanocrystalline 3% Co^{2+}:ZnO Photovoltaic Cells, Integrated between 21550 and 14000 cm^{-1}.

Film Resistance (Ω)	Relative Integrated IQE	Variations In Co^{2+}:ZnO(OH^-) Electrode Preparation	Relative Integrated IQE
>10^9 (aerobic anneal)	1.0	Co^{2+}:ZnO(OH^-)	1.0
>10^9 (vacuum anneal without Sn)	1.0	Co^{2+}:ZnO(Sn)	3.1
3.8×10^7 (vacuum anneal with Sn)	3.3	Co^{2+}:ZnO(Sn-PS)	3.5
1.5×10^7 (vacuum anneal with Sn)	3.0		
2.0×10^6 (vacuum anneal with Sn)	2.3		

* Numbers are reported relative to a reference Co^{2+}:ZnO(OH^-) cell, which is listed as the first entry in each column.

spectra did not change with this procedure, the photocurrent action spectra of films heated with Sn metal all showed a new maximum at 23600 cm^{-1} that was never observed in films that were not annealed with Sn metal. The relative integrated internal quantum efficiencies of cells prepared with and without polystyrene spheres are also summarized in Table 2.3.1. Values are reported relative to the first entry of each column.

2.3.1 Electronic Structure Contribution to Photoinduced Charge Separation in Co^{2+}:ZnO

As a wide bandgap semiconductor, ZnO is normally insensitive to irradiation with visible light. Doping ZnO with Co^{2+} introduces new sub-bandgap absorption that extends the response of ZnO photovoltaic cells throughout the visible energy range (Figure 2.3.2). The photocurrent action spectra (Figure 2.3.2(a)) of the Co^{2+}:ZnO photovoltaic cells examined here were all essentially identical and all generally traced the Co^{2+}:ZnO absorption spectrum over the entire ultraviolet and visible spectral ranges. The dominant feature in the visible region of the photocurrent action spectrum is clearly attributable to the $^4A_2 \rightarrow {}^4T_1(P)$ Co^{2+} ligand field transition, and the photocurrent action spectrum in this energy region closely traces the fine structure of this absorption band between ca. 14000 and 18000 cm^{-1}. The energy, intensity, and band shape of this transition are all similar to those observed for tetrahedral Co^{2+} ions in other semiconductors and in coordination complexes, and are described well by ligand field theory using the parameters Dq = 390 cm^{-1}, B = 775 cm^{-1}, C = 3500 cm^{-1},

and λ = -250 cm^{-1}.[27] Given the highly localized nature of the $^4A_2 \rightarrow {}^4T_1(P)$ excited state, it is paradoxical that this excitation generates macroscopic charge separation.

The photocurrent action spectrum was converted from IPCE to internal quantum efficiency (IQE) as described by Eqn. 2.3.1.1, where T refers to the experimental film transmittance obtained from Figure 2.3.2(a).[29]

$$IQE(\%) = \frac{IPCE}{(1-T)} \qquad \text{Eqn. [2.3.1.1]}$$

Examination of the resulting photocurrent IQE spectrum, plotted in Figure 2.3.2(b), reveals that the quantum yield for generation of detectable carriers by absorbed photons in Co^{2+}:ZnO is wavelength dependent. The photocurrent IQE spectrum shows three distinct sub-bandgap energy regions in the Co^{2+}:ZnO excited state electronic structure: (a) below energies of ca. 14000 cm^{-1} (e.g., $^4T_1(F)$ and $^4T_2(F)$ ligand field excited states), where absorbed photons generate no detectable carriers; (b) between 14000 and 22000 cm^{-1}, where a nearly constant photocurrent IQE of ~0.5% is observed; and (c) above 22000 cm^{-1}, where the photocurrent IQE increases by a factor of more than 4 relative to its value at lower energies, but where no analogous photocurrent intensity is observed in undoped ZnO cells (Figure 2.3.2(b)).

To analyze these three regions of the photocurrent action spectrum, the photocurrent IQE spectrum may be compared with the 300 K electronic absorption and 5 K MCD spectra of Co^{2+}:ZnO, also included in Figure 2.3.2. The electronic absorption spectrum has been described in detail previously.[27] The absorption

spectrum is dominated in the visible energy range by the intense Co^{2+} $^4A_2 \rightarrow {}^4T_1(P)$ ligand field band and in the ultraviolet energy range by the ZnO bandgap absorption. The MCD spectrum reveals two new spectroscopic transitions in this same energy range. Although previous reports have described narrowing of the fundamental bandgap energy of ZnO upon Co^{2+} doping,[2,12] the broad negative MCD feature at ca. 25200 cm^{-1} reveals that the red shift of the band edge absorption is in fact attributable to the appearance of a new electronic excited state at this energy which was not discernible[27] by electronic absorption spectroscopy. The $S = \frac{3}{2}$ saturation magnetization of this MCD intensity rules out its assignment[7] to non-Co^{2+} defect transitions. This transition has been assigned as a light-induced acceptor-type ionization of the transition metal dopant on the basis of optical electronegativity considerations,[20] an assignment strongly supported by the appearance of a similar band shifted to lower energy by 6750 cm^{-1} in the corresponding spectra of Ni^{2+}:ZnO.[20] To higher energy, the positive MCD intensity at ca. 28000 cm^{-1} is the onset of an intense pseudo-A term from the first excitonic transition of the ZnO host, which gains MCD intensity through O_{VB}-Co^{2+} covalency (*p-d* hybridization).[20] The MCD spectrum additionally reveals a very weak, broad transition between ca. 18000 and 22000 cm^{-1} that is also not evident from the electronic absorption spectrum and therefore has not been assigned previously. The saturation magnetization of this weak intensity (measured at 19500 cm^{-1}, Figure 2.3.2(c) (inset)) confirms that it arises from

a $S = 3/2$ ground state, consistent with its assignment to the same magnetically isolated pseudo-tetrahedral Co^{2+} as all of the other observable MCD features. Because of the absence of structure in this weak feature, it is not likely associated with the spin-forbidden *d-d* excitations anticipated in this energy region from ligand field theory. The exception is the sharp peak at 20280 cm^{-1} in both the absorption and MCD spectra, assigned as the $^4A_2 \rightarrow {}^2A_1(G)$ spin-flip transition.[20,27,30] The broad, unstructured band shape of the MCD intensity between 18000 and 22000 cm^{-1} suggests the transition should instead be assigned as a light-induced donor- or acceptor-type ionization process of the transition metal dopant.

These light-induced donor- or acceptor-type ionization processes of the transition metal dopant in DMSs have been studied extensively by both experimental[31-35] and theoretical[36-40] methods. In donor-type ionizations, an electron is formally promoted from the TM^{2+} *d* shell donor orbitals to ZnO-based acceptor orbitals of the conduction band (CB), that is, $d^n (CB)^0 \rightarrow d^{n-1} (CB)^1$. In acceptor-type ionizations, an electron is formally promoted to the TM^{2+} *d* shell acceptor orbitals from ZnO-based donor orbitals of the valence band (VB), that is, $(VB)^q d^n \rightarrow (VB)^{q-1} d^{n+1}$, where *q* is the number of electrons in the valence band. Because considerable charge is shifted between the dopant and the semiconductor in each of these electronic transitions they are often referred to collectively as charge-transfer (CT) processes.[31-38] Treating the semiconductor lattice as a ligand to the dopant, the

donor- and acceptor-type ionization transitions are thus formally metal-to-ligand conduction band CT ($ML_{CB}CT$) and ligand valence band-to-metal CT ($L_{VB}MCT$) transitions, as summarized in Eqn. 2.3.1.2.

$$TM^{2+} \rightarrow TM^{+} + h^{+}_{VB} \quad \left(L_{VB}MCT,\ TM^{2+} \text{ acts as acceptor}\right) \quad \text{Eqn. [2.3.1.2(a)]}$$

$$TM^{2+} \rightarrow TM^{3+} + e^{-}_{CB} \quad \left(ML_{CB}CT,\ TM^{2+} \text{ acts as donor}\right) \quad \text{Eqn. [2.3.1.2(b)]}$$

Analysis of the charge-transfer energies in Co^{2+}:ZnO is facilitated by consideration of the optical electronegativities, χ_{opt}, of the donor (D) and acceptor (A) involved in the transitions. Following Jørgensen,[41-43] Eqn. 2.3.1.3 relates D-A charge transfer transition energies to $\chi_{opt}(D)$ and $\chi_{opt}(A)$ on Pauling's electronegativity scale, taking into account differences in spin-pairing energies (SPEs) between the ground and excited electronic states.

$$E_{CT} = 30000cm^{-1}\left(\chi_{opt}(D) - \chi_{opt}(A)\right) + \Delta SPE \qquad \text{Eqn. [2.3.1.3]}$$

The SPEs of the ground and CT excited states can be estimated from Eqn. 2.3.1.4 using the Racah electron-electron repulsion parameters B and C, determined spectroscopically from analysis of the ligand field absorption data.

$$SPE = \left[\langle S(S+1)\rangle - S(S+1)\right]D \qquad \text{Eqn. [2.3.1.4(a)]}$$

$$D = \left(\frac{7}{6}\right)\left[\left(\frac{5}{2}\right)B + C\right] \qquad \text{Eqn. [2.3.1.4(b)]}$$

For tetrahedral Co^{2+}, χ_{opt} reflects the energy of the doubly occupied d_e (nonbonding) set of d orbitals. A $L_{VB}MCT$ excitation would promote an electron into the half

occupied d_{t_2} (σ*-antibonding) orbitals that lie $10Dq$ above the d_e pair, so for calculation of this transition energy a value of $10Dq$ must be added to Eqn. 2.3.1.3. Using this approach, $\chi_{opt}(Co^{2+}) = 1.9$, $\chi_{opt}(O^{2-}_{VB}) = 2.4$, and $\Delta SPE = +(4/3)D = 8440$ cm^{-1}, a value of $E_{LMCT} \approx 27000$ cm^{-1} is calculated for the first $L_{VB}MCT$ transition of Co^{2+}:ZnO,[20] in excellent agreement with the observed transition energy of ca. 25200 cm^{-1} in Figure 2.3.2(c). The sub-bandgap photocurrent action intensity at 24000 cm^{-1} is therefore attributed to $L_{VB}MCT$ excitation of Co^{2+}:ZnO. This assignment differs from those made previously, in which this photocurrent intensity was suggested to result from promotion of a Co^{2+} d_e electron into the conduction band (i.e. $ML_{CB}CT$),[9] from a transition involving dopant-related defects in the bulk,[7] or from the onset of direct ZnO bandgap excitation.[2]

The photocurrent action intensity below ca. 22000 cm^{-1} is too low in energy to be attributed to the $L_{VB}MCT$ excited state. This conclusion is supported by the reduced photocurrent IQE in this energy range, which suggests charge separation via a different excited state having a lower intrinsic quantum yield for charge separation. This low-energy excited state is unlikely to be the $^4A_2 \rightarrow {}^4T_1(P)$ ligand field state because the high-energy end of this photocurrent action region (ca. 22000 cm^{-1}) substantially exceeds the high-energy tail of the $^4A_2 \rightarrow {}^4T_1(P)$ ligand field absorption band (ca. 19000 cm^{-1}). Indeed, close inspection of the data in Figure 2.3.2(b) reveals that the photocurrent IQE actually decreases as the photon energy is tuned from 22000

to 18000 cm^{-1}. $^4A_2 \rightarrow {}^4T_1(P)$ ligand field excitation thus leads to a reduction in charge separation quantum efficiency, not an increase. We therefore assign the photocurrent action intensity between 14000 and 22000 cm^{-1} in Figure 2.3.2 to an $ML_{CB}CT$ excitation of Co^{2+}:ZnO. The energy anticipated for the $ML_{CB}CT$ transition in Co^{2+}:ZnO can be estimated, again using Jørgensen's optical electronegativity formalism (Eqn. 2.3.1.3). The lowest energy $ML_{CB}CT$ transition involves promotion of an electron from the filled d_e set of orbitals into the conduction band, and consequently no correction for Dq is required. Using Eqn. 2.3.1.3, the value of $\chi_{opt}(Zn^{2+})$ = 1.1 in ZnO estimated previously[43] and verified spectroscopically in Mn^{2+}:ZnO,[21] and $\Delta SPE = -2D$ (-12688 cm^{-1}), the energy of the first $ML_{CB}CT$ transition in Co^{2+}:ZnO is predicted to be 11300 cm^{-1}. Given the crudeness of the model, this energy is in remarkable agreement with the onset of the photocurrent action at 14000 cm^{-1} (Figure 2.3.2), supporting assignment of the broad, weak MCD intensity and photocurrent action in this energy region to a $ML_{CB}CT$ transition.

Between 19000 and 22000 cm^{-1}, the measured photocurrent IQE reflects direct excitation into the very weak, broad absorbance assigned as the $ML_{CB}CT$ band. The photocurrent IQE value in this region is ~0.6%. With excitation between 19000 and 14000 cm^{-1}, the photocurrent IQE reflects excitation into the intense $^4A_2 \rightarrow {}^4T_1(P)$ ligand field band. The photocurrent IQE with ligand field excitation decreases to ~0.4%. These data demonstrate that $^4A_2 \rightarrow {}^4T_1(P)$ ligand field excitation sensitizes

charge separation via the $ML_{CB}CT$ excited state, but with a reduced (~70%) photocurrent IQE relative to direct $ML_{CB}CT$ excitation. Despite the reduced photocurrent IQE, the IPCE is greatly enhanced by this sensitization due to the large increase in optical density at this energy brought by the intense $^4A_2 \rightarrow {}^4T_1(P)$ band. The reduced efficiency for the sensitized photocurrent relative to direct $ML_{CB}CT$ excitation stems from the availability of competitive relaxation pathways for the $^4T_1(P)$ excited state, including luminescence and nonradiative decay to the ground state through the ligand field manifold. The fact that $^4T_1(P) \rightarrow {}^4A_2$ luminescence is observed in Co^{2+}:ZnO, albeit with small quantum yields,[44] indicates a relatively slow relaxation of this excited state and strongly suggests that the $^4T_1(P)$ electronic origin must lie at or below that of the $ML_{CB}CT$ transition. Our attempts to measure the temperature dependence of the photocurrent action or photoconductivity spectra to estimate the energy difference between these two electronic origins have all been unsuccessful due to conductivity quenching under the cryogenic experimental conditions (see Section 2.3.2). Nevertheless, we may conclude that these two electronic origins must be nearly degenerate.

The electronic structure and photophysical properties of Co^{2+}: ZnO deduced from these spectroscopic and photovoltaic measurements are summarized schematically in the energy level diagram of Figure 2.3.1.1, where they are compared directly to the low temperature MCD spectrum from Figure 2.3.2(c). Direct $L_{VB}MCT$ or $ML_{CB}CT$ excitation generates current in the regenerative photovoltaic cells. The

fact that the photocurrent IQEs differ for these two CT excited states indicates that the $L_{VB}MCT$ excited state does not relax efficiently to the $ML_{CB}CT$ excited state or the ligand field excited state manifold, but instead leads directly to upper excited state

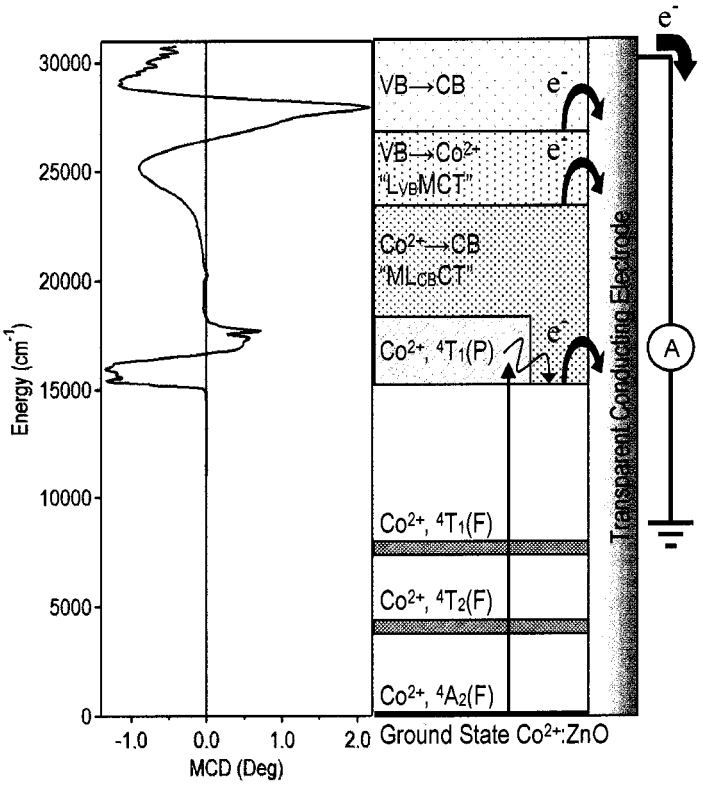

Figure 2.3.1.1. Energy level diagram for Co^{2+}:ZnO deduced from combined spectroscopic and photoelectrochemical measurements, compared with the 5 K, 6.5 T MCD spectrum from Figure 2.3.2(c). The thick arrows describe photoinduced charge separation with excitonic excitation, direct $L_{VB}MCT$ or $ML_{CB}CT$ excitation, and $ML_{CB}CT$ excitation sensitized by Co^{2+} $^4A_2 \rightarrow {}^4T_1(P)$ ligand field excitation.

charge separation. This slow internal conversion is likely due to the fact that the $L_{VB}MCT$ and $ML_{CB}CT$ configurations (Eqns. 2.3.1.5(a) and 2.3.1.5(b), *vide infra*) differ by two electrons. Importantly, the broad $ML_{CB}CT$ band overlaps the intense

$^4A_2 \rightarrow {}^4T_1(P)$ ligand field band in the visible, placing the $ML_{CB}CT$ state in an energy region suitable for sensitization by ligand field excitation. The nonradiative $^4T_1(P) \rightarrow ML_{CB}CT$ internal conversion is indicated in Figure 2.3.1.1 by the curly line. A central conclusion of this study is therefore that there exist two independent Co^{2+}-based pathways to excited-state charge separation in Co^{2+}:ZnO, one involving Co^{2+} photoreduction ($L_{VB}MCT$) and the other involving Co^{2+} photooxidation ($ML_{CB}CT$). Although the internal quantum efficiency of the latter is only ca. 25% that of the former, it proceeds with photons ca. 1 eV lower in energy and is sensitized by the strongly absorbing $^4A_2 \rightarrow {}^4T_1(P)$ ligand field absorption at the low-energy end of the photocurrent action spectrum. From the perspective of solar energy conversion, therefore, ligand field sensitization of the $ML_{CB}CT$ excited state is responsible for the majority of the Co^{2+}:ZnO photoreactivity. Importantly, both CT excitations are able to drive the formation of H_2 from H_2O at Pt counter electrodes in photoelectrochemical cell configurations.[2] Indeed, examination of transient photoelectrochemical potentials found no significant wavelength dependence following initial charge separation, with similar open-circuit recombination kinetics and effective cell capacitances for ultraviolet and visible excitation energies.[45]

We now address the origin of the different photocurrent IQEs for the two CT processes. Although the absolute photocurrent IQE was found to depend on the method of cell preparation (see Chapter 2 Section 2.3.2), the ratio of the photocurrent IQEs for the two CT transitions appears to remain a constant for all of the cells

investigated, despite rather dramatic changes in surface chemistry. This constant ratio implies that the relative photocurrent IQEs for $L_{VB}MCT$ and $ML_{CB}CT$ excitations result from relative branching ratios for charge separation in the respective CT excited states rather than from different probabilities of carrier trapping at the semiconductor surfaces.

In each CT excitation, the transient bound carriers must escape for photocurrent to be detected. Since the photovoltaic devices are regenerative and since neither Co^{+} nor Co^{3+} has been detected in irradiated Co^{2+}:ZnO,[44] excited states leading to detectable photocurrents must generate both electrons and holes at the nanocrystal surfaces. The experimental ratio of photocurrent IQEs ($IQE_{25000}/IQE_{20000} \approx 4$ from Figure 2.3.2(b)) suggests that the carriers generated by $L_{VB}MCT$ excitation are ~4 times more likely to escape than are those generated with $ML_{CB}CT$ excitation. We attribute the difference in photocurrent IQEs between $ML_{CB}CT$ and $L_{VB}MCT$ excited states to differences in the wave functions of these two excited states. The $ML_{CB}CT$ and $L_{VB}MCT$ excited states have configurations formally analogous to deep donor and acceptor states, respectively,[46] and the probability of carrier escape is governed by the localization of these carrier wave functions at the cobalt ions. The limiting carrier in the photocurrent measurement is the one placed on the cobalt center upon photoexcitation. In a configuration interaction (CI) model, the energy difference between the CT and excitonic states (*A*, *B*, and *C 1S* excitonic states,[47] treated together here) regulates the mixing between localized (bound) and delocalized

configurations and therefore determines the effective Bohr radius of the limiting carrier. The three relevant configurations are

$$\psi_1\left(L_{VB}MCT\right):\ \left(Co^{+}+h_{VB}^{+}\right) \qquad \text{Eqn. [2.3.1.5(a)]}$$

$$\psi_2\left(ML_{CB}CT\right):\ \left(Co^{3+}+e_{CB}^{-}\right) \qquad \text{Eqn. [2.3.1.5(b)]}$$

$$\psi_3\left(excitonic\right):\ \left(Co^{2+}+e_{CB}^{-}+h_{VB}^{+}\right) \qquad \text{Eqn. [2.3.1.5(c)]}$$

and the CI wave functions for the two CT excited states in the perturbation limit are therefore

$$\psi_1^{'}=\psi_1+c\psi_3 \qquad \text{Eqn. [2.3.1.6(a)]}$$

$$\psi_2^{'}=\psi_2+c\psi_3 \qquad \text{Eqn. [2.3.1.6(b)]}$$

where $c = H_{n3}/\Delta E_{n,3}$.

The relatively small energetic difference ($\Delta E_{1,3}$ ~ 3000 cm^{-1}, Figure 2.3.2) between the $L_{VB}MCT$ state and the excitonic states leads to extensive mixing of the two, imparting partial excitonic character to the $L_{VB}MCT$ state, and resulting in a relatively small binding energy for the photogenerated carriers (i.e., Co^{+} is a relatively shallow donor in ZnO[15]). Conversely, the substantially greater energetic difference ($\Delta E_{2,3}$ ~ 12000 cm^{-1}, Figure 2.3.2) between the $ML_{CB}CT$ excited state and the excitonic states does not allow for extensive mixing of the two, meaning the limiting photogenerated carrier in the $ML_{CB}CT$ state is strongly bound to the cobalt (i.e., Co^{3+} is a deep acceptor), favoring charge recombination over carrier escape. Although not

detected spectroscopically,[44] Co^{3+} in ZnO has been predicted by cluster model calculations to be relatively stable.[48] Assuming that the binding energy is inversely proportional to the CI mixing between the CT and excitonic states, the ratio of localization energies for the last bound charge carriers in the two CT states in Co^{2+}:ZnO may be estimated as $(\Delta E_{2,3}/\Delta E_{1,3}) = (12000\ cm^{-1}/3000\ cm^{-1}) = 4$, which is on the same order of magnitude as the ratio of photocurrent IQEs measured for these two excited states (also ~4, Figure 2.3.2(b)), suggesting H_{13} and H_{23} matrix elements are of similar magnitude. Notably, the IQEs of both CT states are smaller than that for excitonic excitation in pure ZnO (Figure 2.3.2(b)), consistent with the attribution of carrier generation to a relatively small admixture of excitonic character into the CT wave functions.

The difference in CI mixing is also manifested in the different absorption oscillator strengths for the two CT excitations. Calculations have shown that the oscillator strengths of dopant/semiconductor CT transitions are vanishingly small in the limit of delocalized (band)→ localized (TM^{n+}) or localized (TM^{n+})→ delocalized (band) due to the vanishing donor-acceptor orbital overlap.[31,49] More generally, theoretical and experimental investigations have shown that donor-acceptor CT oscillator strengths are closely related to the square of the perturbation coefficient, c, describing mixing of the donor and acceptor wave functions.[50] In the limit in which all dopant-semiconductor CT absorption intensity is borrowed by CI with the excitonic excited states, the oscillator strength for the CT transition becomes

$$f_{CT} \approx \frac{E_{CT}}{E_{Ex}}\left[\frac{H_{n3}}{\Delta E_{n,3}}\right]^2 f_{Ex} \qquad \text{Eqn. [2.3.1.7]}$$

Approximating $H_{13} = H_{23}$ and estimating the transition threshold energies from Figure 2.3.2 (E_{MLCT} = 14000 cm^{-1}, E_{LMCT} = 23000 cm^{-1}, E_{Ex} = 26000 cm^{-1}), the ratio of CT oscillator strengths in Co^{2+}:ZnO is estimated from Eqn. 2.3.1.7 to be $f_{MLCT}/f_{LMCT} \approx$ 0.038. The precise experimental ratio is not accessible because (i) the CT bands overlap other absorption bands, (ii) the band shapes of the two CT transitions are not known, and (iii) the very small intensity of the $ML_{CB}CT$ transition makes it difficult to identify at most energies. Nevertheless, the ratio of oscillator strengths predicted above is very close to the ratio of the absorbances of these two CT transitions measured at cryogenic temperatures on the same sample as used for Figure 2.3.2(c): $A_{19700cm^{-1}}/A_{25000cm^{-1}} \approx 0.017$. The greater absorption intensity of the $L_{VB}MCT$ transition in Figure 2.3.2 is therefore direct experimental evidence for greater hybridization of the $L_{VB}MCT$ excited state with the excitonic states relative to the $ML_{CB}CT$ excited state in Co^{2+}:ZnO. The relatively large molar absorption coefficient determined recently for the $ML_{CB}CT$ transition in Mn^{2+}:ZnO ($\varepsilon_{Mn^{2+}} \approx 950\ M^{-1}\ cm^{-1}$ at 24000 cm^{-1} and 300 K),[21] which also occurs very near the fundamental bandgap energy of ZnO, supports this interpretation of the CT intensity origins and specifically supports the tacit assertion that the intensity differences do not arise from intrinsic differences in H_{n3} due, for example, to potential symmetry restrictions. Furthermore, the excellent agreement between experimental CT absorption intensities and the trends predicted

based on the above CI model lends credence to the conclusion that CI contributions to the excited-state wave functions dominate the photocurrent IQEs of the same CT transitions.

To quantify the mixing coefficients, c, the experimental oscillator strength for the $ML_{CB}CT$ transition was estimated from the low-temperature absorption spectrum. Accurate determination of the experimental $ML_{CB}CT$ oscillator strength is complicated by the low $ML_{CB}CT$ absorption intensity and the presence of other overlapping absorption bands. Assuming constant $ML_{CB}CT$ absorption intensity between 14000 and 23000 ± 1000 cm^{-1} equal to that observed at 19700 cm^{-1} yields an estimated $ML_{CB}CT$ oscillator strength of $(1.05 \pm 0.05)\times10^{-3}$. From this oscillator strength, Eqn. 2.3.1.7, and the summed oscillator strengths of the nearly degenerate *A*, *B*, and *C 1S* excitons of ZnO ($f_{Ex} = 1.06$),[47] the mixing coefficient (c in Eqn. 2.3.1.6) is estimated to be 0.043 ± 0.003 for the $ML_{CB}CT$ excited state and 0.17 ± 0.01 for the $L_{VB}MCT$ excited state. Within the approximations of Eqn. 2.3.1.7 and the limitations in determining the $ML_{CB}CT$ oscillator strength with accuracy, the $ML_{CB}CT$ excited-state wave function is thus estimated to have ~4-5% excitonic character, whereas the $L_{VB}MCT$ excited-state wave function is estimated to have ~16-18% excitonic character and a correspondingly larger effective Bohr radius. The Bohr radii of the last bound carriers governs the efficiencies of charge hopping to the nanocrystal surfaces for the two CT excited states.[51] Using Eqn. 2.3.1.8[51,32] and the electron and hole effective masses in ZnO, the effective Bohr radii for the limiting carriers in the

L_{VB}MCT and ML_{CB}CT excited states of Co^{2+}:ZnO are estimated to be 0.65 and 0.24 nm, respectively. These dimensions are smaller than but on the same length scale as the mean Co^{2+}-Co^{2+} separation in 3% Co^{2+}:ZnO (ca. 0.92 nm).

$$r_B = \frac{\hbar}{\sqrt{2m^* \Delta E_{n,3}}} \qquad \text{Eqn. [2.3.1.8]}$$

In summary, we conclude that the greater photocurrent IQE of the Co^{2+}:ZnO photoanode following L_{VB}MCT excitation relative to ML_{CB}CT excitation is attributable to a 4-fold greater excitonic character of the L_{VB}MCT excited state wave function. Because this configuration interaction is diminished by increased energetic separation from the excitonic levels, this analysis suggests that sensitization of wide bandgap oxide semiconductors by substitutional dopants will also diminish rapidly as CT energies are tuned away from the fundamental absorption edge of the host semiconductor, perhaps providing an intrinsic limitation to the potential for highly efficient visible light sensitization by substitutional dopants.

2.3.2 General Factors Contributing to Co^{2+}:ZnO Photovoltaic Cell Performance

The major differences among the various cells examined are not found in the wavelength dependence of the photoresponse, but rather in overall efficiencies. As described above, the similar photocurrent action profiles for all of the films studied, independent of surface chemistry or film porosity, argue against surface effects playing any significant role in the initial photophysical events behind the responses of these cells. The differences in overall efficiencies of the different photovoltaic cells

are attributed to the different Co^{2+}:ZnO electrode microstructures and surface chemistries, which combine to govern the competition between slow surface e^{-}-h^{+} recombination and electrolyte diffusion kinetics. In this section we describe briefly two practical aspects of Co^{2+}:ZnO photovoltaic cell construction that were found to influence cell performances significantly.

In general, the resistances of the nanocrystalline Co^{2+}:ZnO electrodes were very high, often beyond the upper limit of our detection capabilities ($>10^{9}$ Ω). Such high resistances favor recombination and other quenching processes that reduce successful capture of photogenerated carriers at the contact electrodes. Measurements of Co^{2+}:ZnO electrode short-circuit dark-current and photocurrent responses under an applied bias (Figure 2.3.4) revealed that the film resistances were extremely sensitive to atmospheric changes. Large increases in current were observed upon exposure to vapors of protic molecules (H_2O, CH_3OH) or air when compared to aprotic molecules (pentane, toluene) or vacuum, suggesting that the film conductivities are dominated by a surface hopping transport mechanism in which protons are the relevant charge carriers.[52,53] Such a high sensitivity to surface chemistry has precedence in studies of gas sensing nanocrystalline ZnO electrodes.[54,55] The importance of surface hopping conductivity may be responsible for the low IPCE values of Co^{2+}:ZnO(amine) films (Figure 2.3.3), since the amine capping process has previously been found to passivate ZnO nanocrystal surface defects, in particular removing surface hydroxides.[17] These

results suggest that poor macroscopic conductivities may limit the overall performances of these nanocrystalline Co^{2+}:ZnO photovoltaic cells, and that improvements in this direction may be possible.

To test the influence of film resistance on photovoltaic cell performance, Co^{2+}:ZnO nanocrystalline electrodes were heated under vacuum at 773 K in the presence of Sn metal. This procedure reduced their resistance by over 3 orders of magnitude (from 10^9 to 10^6 Ω) relative to films annealed aerobically, dependent upon the duration of vacuum annealing (Table 2.3.1). Although it is possible that Sn^{2+} may occupy ZnO interstitial sites as shallow donor defects analogous to interstitial Zn,[15,56] the low vapor pressure of Sn metal (5×10^{-11} Torr at 773 K) argues against this interpretation of the resistance change. Instead, we attribute the reduced resistivities of these films to the formation of oxygen vacancies, a common *n*-type defect in ZnO, facilitated by the oxygen getting capacity of Sn metal. Decreasing the film resistance did generally enhance the overall cell performance, but somewhat surprisingly, the best photovoltaic performance was not observed for the film with the lowest resistance (Table 2.3.1). Nevertheless, these experiments clearly demonstrate that the overall performance of the Co^{2+}:ZnO photovoltaic cells is to some extent limited by the poor macroscopic conductivity of the photoanode. Since Co^{2+} doping itself is responsible for part of the reduced conductivity of Co^{2+}:ZnO, the Co^{2+} concentration must be adjusted to balance high optical densities with high conductivities, and this balance

contributes to the photocatalysis maximum observed at ca. 3% Co^{2+}.[2,7,8,45]

In addition to conductivity limitations, these photovoltaic cells are expected to be limited by relatively slow electrolyte diffusion throughout the porous network of Co^{2+}:ZnO nanocrystals. In these Co^{2+}:ZnO nanocrystalline photovoltaic cells, migration of photogenerated carriers to the crystallite surfaces is substantially more rapid than diffusion of the redox-active electrolytes throughout the porous electrode. For the I^-/I_3^- electrolyte, I^- is present in large excess (9:1 I^-:I_3^-) and the current-limiting redox species is I_3^-.[25] It is therefore reasonable to hypothesize that the photovoltaic properties of these cells could be improved by making the films more porous.[57] The Co^{2+}:ZnO(OH^-) and Co^{2+}:ZnO(OH^--Sn) cells were indeed improved when the films were prepared by addition of 85 ± 5 nm diameter polystyrene spheres to the colloid suspension used for spin-coat processing (Table 2.3.1). SEM images of films prepared with and without added PS (Figure 2.3.1) show average Co^{2+}:ZnO grain diameters of only ~20-50 nm in both films, but the film prepared with added PS is substantially less dense. We conclude that diffusion of electrolyte into the nanoporous network of Co^{2+}:ZnO has been facilitated by the increased film porosity, and that the improved photovoltaic cell performance is due to the improved mobility of I_3^- throughout the photoanode. These results demonstrate that, in addition to film conductivity, electrolyte diffusion is a limiting factor in the performance of these photovoltaic cells and an area where further improvements could likely be made.

2.4 Conclusion

Electronic absorption, magnetic circular dichroism, and photocurrent action spectroscopic measurements have been used to investigate the electronic structural properties of Co^{2+}:ZnO that give rise to macroscopic charge separation when the material is excited with photons in the visible energy range. From analysis of the spectroscopic results, two sub-bandgap CT transitions have been identified and shown to be responsible for photoinduced charge separation. The lower energy CT transition extends down to ca. 14000 cm^{-1} and is assigned as a $ML_{CB}CT$ excitation on the basis of an optical electronegativity analysis. This transition, long postulated to exist in this energy range, is observed directly for the first time using MCD spectroscopy. To higher energy, a more intense $L_{VB}MCT$ transition is detected using MCD spectroscopy. Relative to $ML_{CB}CT$ excitation, $L_{VB}MCT$ excitation yields a 4-fold increase in photocurrent IQE, an increase attributed to greater configuration interaction between this excited state and the *1S* excitonic excited states of ZnO. From this analysis, we conclude that the two CT excited states differ substantially, with the $ML_{CB}CT$ excited state best described as a localized $Co^{3+} + e^{-}_{CB}$ configuration and the $L_{VB}MCT$ excited state ($Co^{+} + h^{+}_{VB}$) having a 4-fold greater admixture of delocalized excitonic ($Co^{2+} + h^{+}_{VB} + e^{-}_{CB}$) character in its wave function. Quantitative analysis of the CT absorption intensities supports this interpretation and suggests admixtures of ~4 and ~17% excitonic character in the $ML_{CB}CT$ and $L_{VB}MCT$ excited states, respectively.

The importance of the electronic structural information obtained from these spectroscopic and photoelectrochemical measurements is not limited to improving our understanding of the photophysical properties of Co^{2+}:ZnO, but relates broadly to the general physical properties of doped oxide semiconductors. Of particular interest to our laboratories is the high Curie temperature ferromagnetism reported recently in transition metal doped ZnO, TiO_2, SnO_2, and related oxide semiconductors,[13,14] including specifically Co^{2+}:ZnO.[15-20] Theoretical models of this magnetism have suggested that ferromagnetic ordering is stabilized by exchange interactions between the magnetic dopants and additional free or defect-bound charge carriers.[16,17,58,59] These exchange interactions may be parameterized as configuration interactions involving CT excited states. To understand the microscopic origins of ferromagnetism in doped oxide semiconductors, it is therefore imperative to have a detailed fundamental understanding of the CT electronic structures of these materials. A detailed description of CT contributions to the magnetism of doped ZnO semiconductors will be presented in Chapter 3.[60]

In addition to fundamental electronic structural studies, various practical aspects of Co^{2+}:ZnO regenerative photovoltaic cell construction have been examined. The conductivity and the porosity of the nanocrystalline Co^{2+}:ZnO electrodes were both found to influence the overall performances of the regenerative photovoltaic cells. Although steps were taken to demonstrate improvement in cell efficiencies by addressing these two factors, the cells described here have not been fully optimized

and continued improvement may be possible with further attention to these two parameters. These two parameters are in some ways specific to this particular application, however, and may not be important for other applications such as the use of colloidal Co^{2+}:ZnO nanocrystals as photoredox catalysts.

2.5 Notes to Chapter 2

[1] Zou, Z.; Ye, J.; Sayama, K.; Arakawa, H., *Nature* **2001**, *414*, 625.

[2] Jaramillo, T. F.; Baeck, S.-H.; Kleiman-Shwarsctein, A.; Choi, K.-S.; Stucky, G. D.; McFarland, E. W., *J. Comb. Chem.* **2005**, *7*, 264.

[3] Kato, H.; Kudo, A., *J. Phys. Chem. B* **2002**, *106*, 5029.

[4] Lettmann, C.; Hinrichs, H.; Maier, W. F., *Angew. Chem., Int. Ed.* **2001**, *40*, 3160.

[5] Serpone, N.; Lawless, D.; Disdier, J.; Hermann, J.-M., *Langmuir* **1994**, *10*, 643.

[6] Kanai, Y., *J. Phys. Soc. Jpn.* **1968**, *24*, 956.

[7] Fichou, D.; Pouliquen, J.; Kossanyi, J.; Jakani, M.; Campet, G.; Claverie, J., *J. Electroanal. Chem.* **1985**, *188*, 167.

[8] Bahadur, L.; Rao, T. N., *Sol. Energy Mater. Sol. Cells* **1992**, *27*, 347.

[9] Hirano, T.; Kozuka, H., *J. Mater. Sci.* **2003**, *38*, 4203.

[10] Kobayashi, K.; Maeda, T.; Matsushima, S.; Okada, G., *Jpn. J. Appl. Phys.* **1992**, *31*, L1079.

[11] Kobayashi, K.; Maeda, T.; Matsushima, S.; Okada, G., *J. Mater.Sci.* **1992**, *27*, 5953.

[12] Lim, S.-W.; Hwang, D.-K.; Myoung, J.-M., *Solid State Commun.* **2003**, *125*, 231.

[13] For a compilation of recent reviews see: Chambers, S. A.; Yoo, Y. K., Eds. *MRS Bull.* **2003**, *23*, 706.

[14] Pearton, S. J.; Heo, W. H.; Ivill, M.; Norton, D. P.; Steiner, T., *Semicond. Sci. Technol.* **2004**, *19*, R59.

[15] Schwartz, D. A.; Gamelin, D. R., *Adv. Mater.* **2004**, *16*, 2115.

[16] Coey, J. M. D.; Venkatesan, M.; Fitzgerald, C. B., *Nature Mater.* **2005**, *4*, 173.

[17] Kittilstved, K. R.; Norberg, N. S.; Gamelin, D. R., *Phys. Rev. Lett.* **2005**, *94*, 147209.

[18] Ueda, K.; Tabata, H.; Kawai, T., *Appl. Phys. Lett.* **2001**, *79*, 988.

[19] Venkatesan, M.; Fitzgerald, C. B.; Lunney, J. G.; Coey, J. M. D., *Phys. Rev. Lett.* **2004**, *93*, 177206.

[20] Schwartz, D. A.; Norberg, N. S.; Nguyen, Q. P.; Parker, J. M.;Gamelin, D. R., *J. Am. Chem. Soc.* **2003**, *125*, 13205.

[21] Norberg, N. S.; Kittilstved, K. R.; Amonette, J. E.; Kukkadapu, R.K.; Schwartz, D. A.; Gamelin, D. R., *J. Am. Chem. Soc.* **2004**, *126*, 9387.

[22] Noack, V.; Eychmüller, A., *Chem. Mater.* **2002**, *14*, 1411.

[23] Hagfeldt, A.; Grätzel, M., *Acc. Chem. Res.* **2000**, *33*, 269.

[24] Smestad, G. P., *Sol. Energy Mater. Sol. Cells* **1998**, *55*, 157.

[25] Papageorgiou, N.; Maier, W. F.; Grätzel, M., *J. Electrochem. Soc.* **1997**, *144*, 876.

[26] Perrin, D. D.; Armarego, W. L. F.; Perrin, D. R., *Purification of Laboratory Chemicals*, 2nd ed.; Pergamon Press: New York, 1980; p568.

[27] Weakliem, H. A., *J. Chem. Phys.* **1962**, *36*, 2117.

[28] Hauch, A.; Georg, A., *Electrochim. Acta* **2001**, *46*, 3457.

[29] To avoid division by zero, a nonzero absorption baseline offset must be included in the application of Eqn. 2.3.1.1 at energies below 14000 cm^{-1} where the sample absorbance goes to zero. Addition of a small baseline offset does not alter the relative IQEs to any significant extent.

[30] Koidl, P., *Phys. Rev. B* **1977**, *15*, 2493.

[31] Noras, J. M.; Allen, J. W., *J. Phys. C* **1980**, *13*, 3511.

[32] Heitz, R.; Hoffmann, A.; Broser, I., *Phys. Rev. B* **1993**, *48*, 8672.

[33] Bishop, S.G.; Robbins, D. J.; Dean, P. J., *Solid State Commun.* **1980**, *33*, 119.

[34] Müller, B.; Roussos, G.; Schulz, H.-J., *J. Cryst. Growth* **1985**, *72*, 360.

[35] Juhl, A.; Hoffmann, A.; Bimberg, D.; Schulz, H.-J., *Appl. Phys. Lett.* **1987**, *50*, 1292.

[36] Fleurov, V. N.; Kikoin, K. A., *Solid State Commun.* **1982**, *42*, 353.

[37] Mizokawa, T.; Fujimori, A., *Phys. Rev. B* **1993**, *48*, 14150.

[38] Blinowski, J.; Kacman, P.; Dietl, T., *Mater Res. Soc. Symp. Proc.* **2002**, *690*, 109.

[39] Fazzio, A.; Caldas, M. J.; Zunger, A., *Phys. Rev. B* **1984**, *30*, 3430.

[40] Langer, J. M.; Delerue, C.; Lannoo, M.; Heinrich, H., *Phys. Rev. B* **1988**, *38*, 7723.

[41] Jørgensen, C. K., *Prog. Inorg. Chem.* **1970**, *12*, 101.

[42] Lever, A. B. P., *Inorganic Electronic Spectroscopy*, 2nd ed.; Elsevier Science Publishers: Amsterdam, The Netherlands, 1984, and references therein.

[43] Duffy, J. A., *J. Chem. Soc., Dalton Trans.* **1983**, 1475.

[44] Schultz, H.-J.; Thiede, M., *Phys. Rev. B* **1987**, *35*, 18.

[45] Fichou, D.; Mesmaeker, A. K.-D., *J. Electroanal. Chem.* **1986**, *215*, 161.

[46] Robbins, D. J.; Dean, P. J.; West, C. L.; Hayes, W., *Philos. Trans. R. Soc. London* **1982**, *304*, 499.

[47] Wrzesinski, J.; Fröhlich, D., *Solid State Commun.* **1998**, *105*, 301.

[48] Gemma, N., *J. Phys. C: Solid State Phys.* **1984**, *17*, 2333.

[49] Bulyanitsa, D. S.; Grinberg, A. A., *Sov. Phys. Semicond.* **1978**, *12*, 933.

[50] Solomon, E. I.; Hanson, M. A., Bioinorganic Spectroscopy. In *Inorganic Electronic Structure and Spectroscopy*; Solomon, E. I., Lever, A. B. P., Eds.; Wiley-Interscience: New York,1999; Vol. II, p1.

[51] Shklovskii, B. I., *Sov. Phys. Semicond.* **1973**, *6*, 1053.

[52] Schaub, R.; Thostrup, P.; Lopez, N.; Laegsgarrd, E.; Stensgaard,I.; Norskov, J. K.; Besenbacher, F., *Phys. Rev. Lett.* **2001**, *87*, 266104.

[53] Wan, Q.; Li, Q. H.; Chen, Y. J.; Wang, T. H.; He, X. L.; Gao, X.G.; Li, J. P., *Appl. Phys. Lett.* **2004**, *84*, 3085.

[54] Traversa, E.; Bearzotti, A., *Sens. Actuators, B* **1995**, *23*, 181.

[55] Cheng, X. L.; Zhao, H.; Hso, L. H.; Gao, S.; Zhao, J. G., *Sens. Actuators, B* **2004**, *102*, 248.

[56] Thomas, D. G., *J. Phys. Chem. Solids* **1957**, *3*, 229.

[57] Brabec, C. J.; Nann, T.; Shaheen, S. E., *MRS Bull.* **2004**, *29*, 43.

[58] Dietl, T.; Ohno, H.; Matsukura, F.; Cibert, J.; Ferrand, D., *Science* **2000**, *287*, 1019.

[59] Sato, K.; Katayama-Yoshida, H., *Physica E* **2001**, *10*, 251.

[60] Kittilstved, K. R.; Liu, W. K.; Gamelin, D. R., *Nature Mater.* **2006**, *5*, 291.

Chapter 3: Correlation Between the Electronic Structures and Polarity-Dependent High-T_C Ferromagnetism in Oxide-Diluted Magnetic Semiconductors

Future spin-based electronics (spintronics) technologies based on diluted magnetic semiconductors (DMSs) will rely heavily on a sound understanding of the microscopic origins of ferromagnetism in such materials. Discoveries of room temperature ferromagnetism in wide bandgap DMSs hold great promise, however, the origin of this ferromagnetism remains poorly understood. In this chapter, a relationship between the electronic structures and polarity-dependent high-T_C ferromagnetism of 3*d* transition metal ions doped ZnO (TM^{2+}:ZnO) DMSs is demonstrated. The trends in ferromagnetism across the 3*d* series of TM^{2+}:ZnO DMSs predicted from the energies of donor- and acceptor-type excited states reproduce the experimental trends well. The results presented in this chapter provide a unified basis for understanding both *n*- and *p*-type ferromagnetic oxide DMSs. The contents of this chapter are results from a collaborative effort with Dr. Kevin R. Kittilstved (University of Washington).

3.1 Introduction

Diluted magnetic semiconductors (DMSs) are attracting intense interest for potential new device applications in spin-based information-processing technologies. For practical spintronics applications, ferromagnetic DMSs with Curie temperatures (T_C) greatly exceeding room temperature will be required. Theoretical predictions[1,2]

of high-T_C ferromagnetism in DMSs of GaN and ZnO stimulated efforts to develop these and related wide bandgap materials.[3] In many regards, ZnO is the archetypical wide bandgap semiconductor. Compared with other oxides that have been investigated as DMSs (for example, TiO_2 and SnO_2), ZnO is relatively well behaved from an experimental point of view, affording the possibility for extensive systematic experimentation and data analysis. Well defined doping and defect chemistries, suitability for transparent high-power high-temperature applications, and the ability to lase or emit spontaneously at ultraviolet wavelengths combine to make ZnO attractive for many potential device applications.[4] For spintronics applications, the relatively long room-temperature spin-coherence time of *n*-type ZnO is advantageous.[5] Additionally, the potential to generate both p-and n-type ZnO of low resistivity makes bipolar spintronics based on ZnO a realistic possibility, and reports of both hole-[6–9] and electron-mediated[10-12] ferromagnetism in ZnO DMSs are encouraging in this regard. The microscopic origins of this high-T_C ferromagnetism, however, remain poorly understood. A detailed understanding of high-T_C ferromagnetism in wide bandgap DMSs is required to harness functionality for device applications. The development of such an understanding has emerged as one of the most important challenges in modern magnetism.[13,14]

In this chapter, we demonstrate that ferromagnetism in ZnO DMSs is intimately related to the electronic structures of the magnetic impurity ions. Electronic absorption, magnetic circular dichroism (MCD), and photocurrent action

spectroscopies are used to identify and assign dopant-derived donor- and acceptor-type ionization excited states, and to analyze the properties of these states related to carrier-mediated ferromagnetism. The opposite polarities predicted[2] and observed[6] for ferromagnetic Co^{2+}:ZnO (*n*-type) and Mn^{2+}:ZnO (*p*-type) are of particular interest. From experimentally calibrated excited-state energies and configuration interaction considerations, trends in ferromagnetism across the 3*d* series of *n*-and *p*-type TM^{2+}:ZnO DMSs are predicted and compared to experimental results. The predicted trends reproduce experimental trends remarkably well, confirming the role of donor and acceptor excited-state configurations in the ferromagnetism of TM^{2+}:ZnO DMSs and, by extension, wide bandgap DMSs as a class.

3.2 Experimental

Alkyl-capped (Alkyl = trioctylphosphine oxide or dodecylamine) colloidal TM^{2+}:ZnO (TM^{2+} = Co^{2+}, Mn^{2+}) nanocrystals were synthesized as described previously in Chapter 2. Manganese acetate tetrahydrate ($Mn(OAc)_2 \cdot 4H_2O$, 99.999%, Strem Chemicals Inc.) was used for the synthesis of Mn^{2+}:ZnO. The colloidal Mn^{2+}:ZnO (up to 2% Mn^{2+}) and Co^{2+}:ZnO (up to 3.5% Co^{2+}) nanocrystals were used to fabricate poly-nanocrystalline films on quartz substrates for magnetic[6] measurements and on transparent indium tin oxide substrates for photovoltaic measurements as described previously in Chapter 2. The dopant concentrations were determined by inductively coupled plasma-atomic emission spectrometry (Jarrel Ash

model 995). Electronic absorption spectra were collected using a Cary 5E spectrophotometer (Varian). MCD spectra were collected using an ultraviolet/visible/near-infrared spectrophotometer constructed from an Aviv 40DS with a sample compartment modified to house a high-field superconducting magneto-optical cryostat mounted in the Faraday configuration. MCD intensities were measured as the absorbance difference $\Delta A = A_L - A_R$ (where L and R refer to left- and right-circularly-polarized photons) and are reported as $\theta(\text{deg}) = (32.9\ \Delta A)/A$. Magnetic susceptibility measurements were carried out using a Quantum Design MPMS-5S SQUID magnetometer. The net diamagnetic background was subtracted from the raw magnetization data (see the Appendix A). Photocurrent action spectra were measured using a μAutolab Type II potentiostat (Eco Chemie B.V.) integrated with the Aviv 40DS spectropolarimeter and converted to internal quantum efficiency (IQE).

3.3 Results and Discussion

3.3.1 Experimental Trends in TM^{2+}:ZnO Dilute Magnetic Semiconductor Ferromagnetism

Several groups have reported ferromagnetism in TM^{2+}:ZnO DMSs.[3] To minimize potential sources of experimental error, some groups have compared different TM^{2+}:ZnO DMSs prepared under identical conditions. Ueda *et al.* examined a series of *n*-type TM^{2+}:ZnO (TM^{2+} = Co^{2+}, Mn^{2+}, Cr^{2+}, and Ni^{2+}) films prepared by pulsed laser deposition.[15] High-T_C ferromagnetism was only observed in Co^{2+}-doped films and not in any of the others. Venkatesan and collaborators[12,14] prepared a

broader series of *n*-type ZnO DMSs by pulsed laser deposition and observed two maxima in the 300 K ferromagnetic saturation moments, one at Co^{2+}:ZnO (d^7) and the other at V^{2+}:ZnO (d^3). Mn^{2+}:ZnO (d^5) showed little or no ferromagnetism under the sample preparation conditions of either laboratory. Kittilstved *et al.* observed the same trend in natively *n*-type Co^{2+}:ZnO and Mn^{2+}:ZnO prepared using an oxidative direct chemical route that unambiguously precluded formation of metal precipitates.[6] The chemical approach also allowed investigation of the influence of nitrogen, a *p*-type dopant in ZnO. When nitrogen was introduced during materials preparation, Mn^{2+}:ZnO showed strong ferromagnetism, whereas Co^{2+}:ZnO showed none.[6,9,16] When plotted in table format as in Figure 3.3.1.1, the opposite carrier polarities of ferromagnetic Co^{2+}:ZnO and Mn^{2+}:ZnO become strikingly apparent. This polarity-dependent ferromagnetism is shown below to derive from specific electronic structural properties of the Co^{2+} and Mn^{2+} ions in the ZnO host semiconductor.

The experimental trends described above and in Figure 3.3.1.1 are in general agreement with most theoretical predictions, despite the use of a variety of different theoretical models.[1,2,14,17,18] A key property common to all of the models describing ZnO-DMS ferromagnetism is strong electronic coupling between the magnetic ions and charge carriers at the Fermi level. As isovalent TM^{2+} doping of ZnO does not itself introduce carriers, carriers in TM^{2+}:ZnO DMSs are associated with additional shallow donor or acceptor defects. The dopant-carrier exchange energy is

parameterized variously as J_{sd}, J_{pd}, $N_0\alpha$, or $N_0\beta$[1,14,19] depending on the specific interaction and model under consideration. Microscopically, these exchange-coupling parameters account for partial carrier delocalization onto the magnetic dopant. In a configuration interaction picture, this implies mixing between the relevant localized

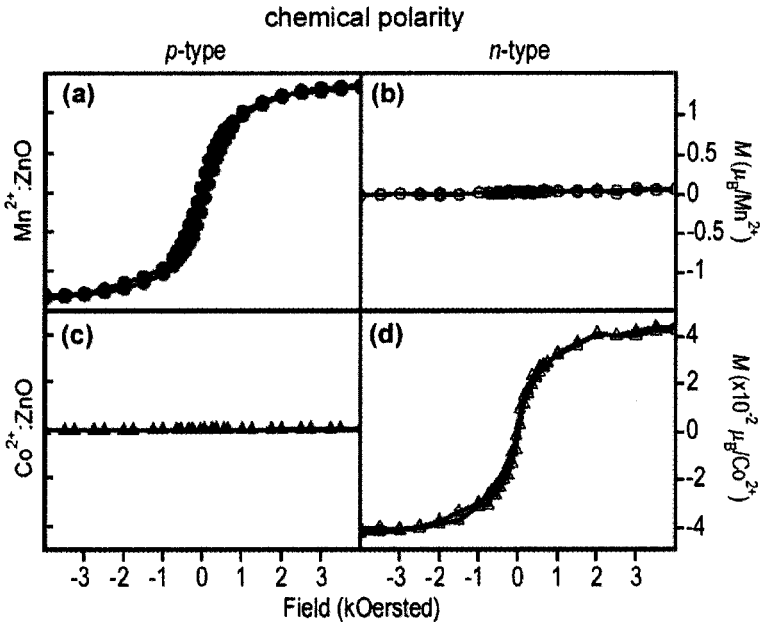

Figure 3.3.1.1. 300 K magnetization data for 0.2% Mn^{2+}:ZnO and 3.5% Co^{2+}:ZnO polycrystalline thin films prepared by direct chemical synthesis with or without addition of nitrogen. **(a)** 0.2% Mn^{2+}:ZnO with added nitrogen, **(b)** 0.2% Mn^{2+}:ZnO without added nitrogen, **(c)** 3.5% Co^{2+}:ZnO with added nitrogen, and **(d)** 3.5% Co^{2+}:ZnO without added nitrogen.

and charge-separated electronic configurations of the magnetic impurity ion. The striking differences between Co^{2+}:ZnO and Mn^{2+}:ZnO in Figure 3.3.1.1 indicate that TM^{2+} electronic structures must regulate the abilities of holes and electrons to delocalize onto these dopants. Specifically, the data in Figure 3.3.1.1 suggest that the

resonances described by Eqns. 3.3.1.1(a) and 3.3.1.1(b) are relevant, whereas those of Eqns. 3.3.1.1(c) and 3.3.1.1(d) are not.

$$Co^{2+} + e^{-}_{donor} \leftrightarrow Co^{+} \qquad \text{Eqn. [3.3.1.1(a)]}$$

$$Mn^{2+} + h^{+}_{acceptor} \leftrightarrow Mn^{3+} \qquad \text{Eqn. [3.3.1.1(b)]}$$

$$Co^{2+} + h^{+}_{acceptor} \not\leftrightarrow Co^{3+} \qquad \text{Eqn. [3.3.1.1(c)]}$$

$$Mn^{2+} + e^{-}_{donor} \not\leftrightarrow Mn^{+} \qquad \text{Eqn. [3.3.1.1(d)]}$$

The forward direction in Eqn. 3.3.1.1(a) describes the formal transfer of a shallow donor's electron $\left(e^{-}_{donor}\right)$ onto Co^{2+} to form Co^{+}, whereas in Eqn. 3.3.1.1(b) it describes the transfer of a shallow acceptor's hole $\left(h^{+}_{acceptor}\right)$ onto Mn^{2+} to form Mn^{3+}. The reverse directions describe formal donor- and acceptor-type ionization processes of the one-electron reduced (Co^{+}) or oxidized (Mn^{3+}) magnetic dopants. As equilibria, Eqns. 3.3.1.1(a) and 3.3.1.1(b) thus describe dopant-donor/acceptor hybridization. This hybridization is the pivotal feature determining T_C in theoretical models describing DMS ferromagnetism. In the spin-split donor impurity-band model for *n*-type ferromagnetic DMSs,[14] a phenomenological dopant effective radius scaling parameter $\left(r_c^{eff}/r_o\right)^3$ was introduced to account for hybridization enhancement of the *s–d* exchange parameter (J_{sd}) required to increase the predicted T_C from 1 to ~500 K. The actual extent of hybridization was small, and 1–2% electron transfer to the dopant was considered sufficient,[14] that is, the ground state lies far to the left in Eqn.

3.3.1.1(a), a conclusion consistent with ferromagnetic *X*-ray MCD data showing a multiplet structure characteristic of tetrahedral Co^{2+} in ZnO[20]. Similarly, in the Zener model description of *p*-type ferromagnetic DMSs, the high T_C predicted for *p*-type Mn^{2+}:ZnO is derived from its large *p–d* exchange parameter[1] ($N_0\beta$), the magnitude of which is determined primarily by *p–d* hybridization.[19] *Ab initio* local spin-density approximation of the density-functional theory (LSDA-DFT) calculations[2,17,18] have predicted ferromagnetism in *p*-type Mn^{2+}:ZnO that results from partial delocalization of $h^+_{acceptor}$ onto Mn^{2+}, which imparts manganese 3*d* character at the Fermi level, but e^-_{donor} did not delocalize onto Mn^{2+} and consequently no ferromagnetism was predicted for *n*-type Mn^{2+}:ZnO[2]. To understand the resonances described by Eqn. 3.3.1.1, and to develop a comprehensive model that describes both *n*- and *p*-type high-T_C ferromagnetic ZnO DMSs, it is imperative to understand the dopant-derived donor- and acceptor-type ionization processes of these DMSs.

3.3.2 Excited States and Electronic Structures

The sub-bandgap electronic excited states of Co^{2+}:ZnO and Mn^{2+}:ZnO were investigated using optical spectroscopic and photoelectrochemical probes. Figure 3.3.2.1 shows electronic absorption spectra, photocurrent internal quantum efficiencies[21] (IQEs), and MCD spectra of paramagnetic Co^{2+}:ZnO and Mn^{2+}:ZnO. The intense absorption and MCD feature at ~28000 cm^{-1} in both DMSs arises from

the first excitonic configuration of ZnO at the band edge. The structured intensity of Co^{2+}:ZnO centered at 16000 cm^{-1} in Figure 3.3.2.1(a),(c) is the spin-orbit split $^4A_2 \rightarrow {}^4T_1(P)$ ligand field band of Co^{2+} doped substitutionally into wurtzite ZnO.[22,23]

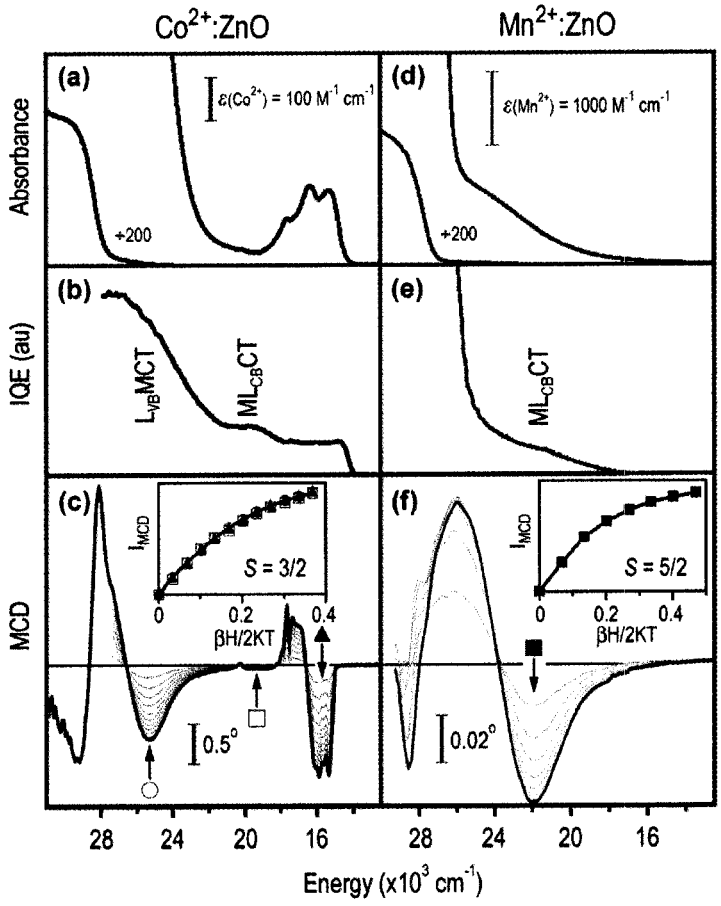

Figure 3.3.2.1. Electronic absorption, photocurrent IQE, and MCD spectroscopic data for Co^{2+}:ZnO and Mn^{2+}:ZnO. **(a)** and **(d)** 300 K electronic absorption spectra. **(b)** and **(e)** Photocurrent IQEs of photovoltaic cells. **(c)** and **(f)** Variable-field 5 K MCD spectra. The insets show MCD saturation magnetization data measured at the energies marked, superimposed on $S = \frac{3}{2}$ and $S = \frac{5}{2}$ Brillouin curves. Data in parts **(b)**, **(c)**, and **(f)** are from refs. [21], [23] and [9], respectively.

As discussed in Chapter 2, the two additional sub-bandgap features observed in the MCD and photocurrent action spectra of Co^{2+}:ZnO (Figures 3.3.2.1(a)–(c)) are assigned as $L_{VB}MCT$ and $ML_{CB}CT$ transitions for the higher energy (centered at ~25000 cm^{-1}) and lower energy (from ~22000 cm^{-1} extending down to 14000 cm^{-1}) bands, respectively.

In the spectra of Mn^{2+}:ZnO (Figures 3.3.2.1(d)–(f)), only one sub-bandgap absorption band is observed, a photoactive state having an associated pseudo-A term MCD signal centered at ~24000 cm^{-1}. Again, applying Jørgensen's optical electronegativity model[24,25] (Eqn. 2.3.1.3 in Chapter 2), the $L_{VB}MCT$ and $ML_{CB}CT$ transitions of Mn^{2+}:ZnO ($\chi_{opt}(Mn^{2+}) = 1.45$), $B = 596$ cm^{-1}, $C/B = 6.5$, $Dq = 420$ cm^{-1}) are predicted to occur at ~49000 and 24000 cm^{-1}, respectively, leading to assignment of this band as the $ML_{CB}CT$ transition.[9] Its assignment to ligand field transitions is ruled out by its high molar extinction coefficient ($\varepsilon_{Mn^{2+}} \approx 950$ M^{-1} cm^{-1} at 24000 cm^{-1} and 300 K, compared with $\varepsilon_{Mn^{2+}} \approx$ 1-10 M^{-1} cm^{-1} ~24850 cm^{-1} anticipated for the $^4T_1(G)$ ligand field excited state)[9]. The very high energy predicted for the $L_{VB}MCT$ transition in Mn^{2+}:ZnO agrees with that estimated from analysis of Mn^{2+}:ZnO *X*-ray absorption data[26] (~62000 ± 12000 cm^{-1}).

Two key observations from Figure 3.3.2.1 pertain to the magnetism of these ZnO DMSs: (i) both Co^{2+}:ZnO and Mn^{2+}:ZnO possess donor- or acceptor-type

ionization states immediately below the ZnO band edge; (ii) the identities of the ionization states at the band edge are different for Co^{2+}:ZnO and Mn^{2+}:ZnO, the former being an $L_{VB}MCT$ state and the latter being an $ML_{CB}CT$ state. As described below, observation (i) relates to the existence of high-T_C ferromagnetism mediated by shallow donors or acceptors, whereas observation (ii) relates to the polarity of the mediating charge carrier.

The spectroscopic data in Figure 3.3.2.1 also provide information about excited-state wavefunctions. As discussed previously[21,27–32] and in Chapter 2, donor- and acceptor-type ionization excited states in DMSs may be described as excitons bound to the isoelectronic impurity in which either the electron ($L_{VB}MCT$) or the hole ($ML_{CB}CT$) is strongly localized at the TM^{2+} ion. The configuration interaction wavefunctions describing these excited states in the perturbation limit are given by Eqn. 3.3.2.1(d)[21,32], where the mixing coefficient $c_{n,3} = H_{n3}/\Delta E_{n,3}$, and H_{n3} and $\Delta E_{n,3}$ are the off-diagonal electronic coupling matrix element and the energy difference between the relevant localized and delocalized configurations, respectively.

$$\psi_1(\mathrm{L_{VB}MCT}): TM^{+} + h^{+}_{VB} \qquad \text{Eqn. [3.3.2.1(a)]}$$

$$\psi_2(\mathrm{ML_{CB}CT}): TM^{3+} + e^{-}_{CB} \qquad \text{Eqn. [3.3.2.1(b)]}$$

$$\psi_3(\mathrm{excitonic}): TM^{2+} + e^{-}_{CB} + h^{+}_{VB} \qquad \text{Eqn. [3.3.2.1(c)]}$$

$$\psi'_n = \psi_n + c_{n,3}\psi_3 \qquad \text{Eqn. [3.3.2.1(d)]}$$

Excited states leading to detectable photocurrents in the TM^{2+}:ZnO photovoltaic cells

must generate both electrons and holes at the electrode surfaces. Although the absolute photocurrent IQEs depend on cell-engineering parameters[21], the ratio of photocurrent IQEs for the L_{VB}MCT and ML_{CB}CT transitions in Co^{2+}:ZnO ($IQE_{25000}/IQE_{20000} \approx 4$ from Figure 3.3.2.1(b)) is due to the intrinsic branching ratios for charge separation in the respective excited states, and reflects differences in mixing between localized (Eqns. 3.3.2.1(a) and 3.3.2.1(b)) and delocalized (Eqn. 3.3.2.1(c)) excited-state configurations for the carrier transferred to the dopant upon excitation.

The relatively small energetic difference ($\Delta E_{1,3} \approx 2600$ cm^{-1}, Figure 3.3.2.1) between the L_{VB}MCT and excitonic states in Co^{2+}:ZnO imparts substantial excitonic character to the L_{VB}MCT wavefunction, and reflects a relatively small binding energy for the photogenerated bound electron, favoring carrier escape. Conversely, the greater energetic difference ($\Delta E_{2,3} \approx 13400$ cm^{-1}, Figure 3.3.2.1) between the ML_{CB}CT and excitonic states does not allow extensive mixing of the two, so the photogenerated hole is strongly bound to the cobalt and charge recombination is favored. The ratio of localization energies for the last bound charge carriers in the L_{VB}MCT and ML_{CB}CT excited states in Co^{2+}:ZnO ($\Delta E_{2,3}/\Delta E_{1,3} \approx 5$) is similar to the ratio of photocurrent IQEs measured for these two excited states (~4, Figure 3.3.2.1(b)), and both IQEs are smaller than that for excitonic excitation in pure ZnO, consistent with the attribution of photocurrent to the admixture of ψ_3 into the L_{VB}MCT and ML_{CB}CT wavefunctions described by Eqn. 3.3.2.1(d). Quantitative analysis of the transition oscillator strengths yields estimated mixing coefficients $c_{1,3} = 0.17 \pm 0.01$ and $c_{2,3} = 0.043 \pm 0.003$ for

Co^{2+}:ZnO[21], and $c_{2,3} = 0.19 \pm 0.03$ for Mn^{2+}:ZnO.

The $L_{VB}MCT$ and $ML_{CB}CT$ energies of dopants in unstable oxidation states can be analyzed using Born thermodynamic cycles. Following McClure *et al.*[33], the energy of a $ML_{CB}CT$ transition for TM^{2+} in ZnO as defined by Eqn. 2.3.1.2(b) in Chapter 2 is given by Eqn. 3.3.2.2, where I_3(TM) is the third ionization potential of the dopant, $\Delta V(\text{site}) = V_3 - V_2$ is the difference in total potential for TM^{3+} and TM^{2+} at the Zn^{2+} crystal site, and χ is the electron affinity of the semiconductor.

$$E_{M^{2+}LCT} = I_3(TM) - \Delta V(site) - \chi \qquad \text{Eqn. [3.3.2.2]}$$

Similarly, the $L_{VB}MCT$ energy involving the one-electron oxidized dopant (TM^{3+}) is given by Eqn. 3.3.2.3, where E_g is the bandgap energy of the host crystal.

$$E_{LM^{3+}CT} = E_g + \Delta V(site) - I_3(TM) + \chi \qquad \text{Eqn. [3.3.2.3]}$$

Concatenation of these two processes gives $TM^{2+} \rightarrow TM^{3+} + e_{CB}^- \rightarrow TM^{2+} + e_{CB}^- + h_{VB}^+$, which is identical to excitonic excitation (Eqn. 3.3.2.1(c)), and the sum of Eqns. 3.3.2.2 and 3.3.2.3 yields $E_{M^{2+}LCT} + E_{LM^{3+}CT} = E_g$. Corresponding relationships hold for the reverse order of promotions, $TM^{2+} \rightarrow TM^{+} + h_{VB}^+ \rightarrow TM^{2+} + h_{VB}^+ + e_{CB}^-$ for which $E_{LM^{2+}CT} + E_{M^{+}LCT} = E_g$. $E_{LM^{3+}CT}$ and $E_{M^{+}LCT}$ are thus identical to $\Delta E_{2,3}$ and $\Delta E_{1,3}$ from Eqns. 3.3.2.1(a)–3.3.2.1(c), respectively. This model assumes that e_{CB}^- and h_{VB}^+ are far from their sources in the $L_{VB}MCT$ and $ML_{CB}CT$ excited states (Eqn. 2.3.1.2 in Chapter 2), a condition that is never actually fulfilled. Although additional corrections

should be considered, these corrections are small compared with the photon energies under consideration and empirically the model accounts well for experimental energies.[30,33] From these identities and the spectroscopic data in Figure 3.3.2.1, E_{M^+LCT} and $E_{LM^{3+}CT}$ can be deduced for cobalt and manganese in ZnO. From this

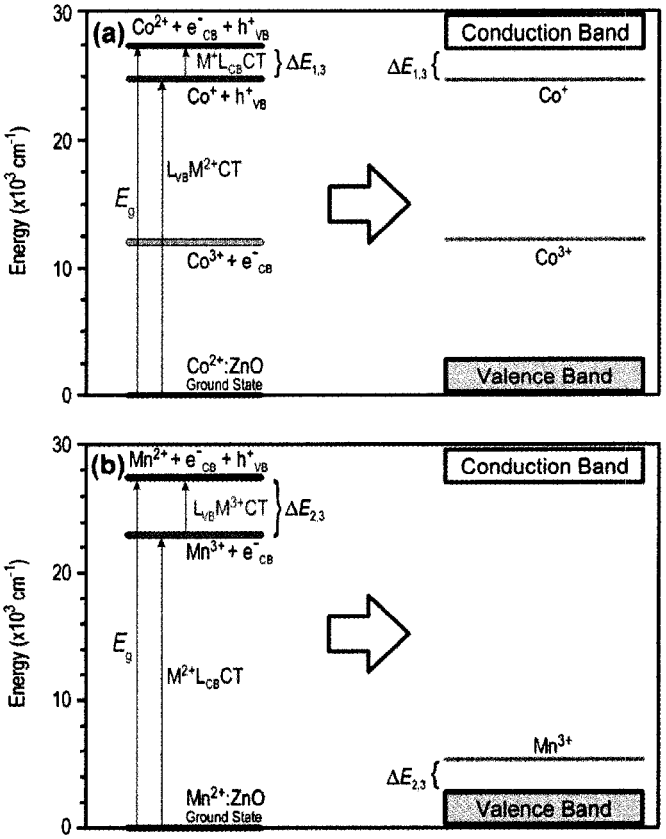

Figure 3.3.2.2. Schematic summary of the spectroscopic analysis for Co^{2+}- and Mn^{2+}-doped ZnO DMSs. This shows the relationship between excited-state energies and donor or acceptor energies derived from the Born cycle analysis. **(a)** Co^{2+}:ZnO. **(b)** Mn^{2+}:ZnO. From this analysis, Co^{+} should be a shallow donor and Mn^{3+} a shallow acceptor in ZnO.

analysis, the transition $Co^{+} \rightarrow Co^{2+} + e^{-}_{CB}$ occurs at very low energy ($\Delta E_{1,3} \approx 2600$ cm^{-1}) as does the transition $Mn^{3+} \rightarrow Mn^{2+} + h^{+}_{VB}$ ($\Delta E_{2,3} \approx 3400$ cm^{-1}), whereas those involving Co^{3+} ($\Delta E_{2,3} \approx 13400$ cm^{-1}) and Mn^{+} ($\Delta E_{1,3} \approx -21600$ cm^{-1}) do not. This analysis is summarized schematically in Figure 3.3.2.2 and numerically in Table 3.3.2.1.

Table 3.3.2.1. Donor or acceptor properties for one-electron reduced or oxidized transition metal dopants in ZnO, estimated from Eqn. 3.3.3.2 and the data in Figure 3.3.2.1. The properties of commonly-invoked shallow donors and acceptors are included for comparison.

Donor or Acceptor	Carrier Type	E_b (cm^{-1})*	E_b (eV)*	r_B (nm)	Ref.
Mn^{3+}:ZnO	h^+	3400	0.42	0.45	This work
Mn^{+}:ZnO	e^-	-21600	-2.68	0.24†	This work
Co^{3+}:ZnO	h^+	13400	1.66	0.23	This work
Co^{+}:ZnO	e^-	2600	0.32	0.70	This work
N_O^{2-}:ZnO	h^+	1600	0.20	0.65	[4]
Zn_i^{0}:ZnO	e^-	240	0.03	2.31	[34]

* From $\Delta E_{n,3}$ for transition metal dopants. † Unstable.

3.3.3 Electronic Structure and Ferromagnetism

In this section, we assume the basic framework of the spin-split donor impurity-band model described in ref. [14] and focus on the key microscopic property governing defect-mediated ferromagnetism in this model, namely hybridization between the magnetic dopant and the defect so that carriers at the Fermi level are partially delocalized onto the magnetic dopant (Eqn. 3.3.1.1, and accounted for in ref.

[14] using the scaling parameter $\left(r_c^{eff}/r_o\right)^3$). Although the model in ref. [14] was developed exclusively for donor defects, the kernel of the model also applies to acceptor defects as shown below. From perturbation theory, dopant-defect hybridization is parameterized by the mixing coefficient, c_{DD} (Eqn. 3.3.3.1). For effective hybridization, the energy difference between dopant and defect levels $\left(\Delta E_{DD}\right)$ must be small and the resonance integral $\left(H_{DD}\right)$ must be large.

$$c_{DD} = \frac{H_{DD}}{\Delta E_{DD}} \qquad \text{Eqn. [3.3.3.1]}$$

To analyze ΔE_{DD}, the thermodynamics of the four dopant-defect resonances described by Eqns. 3.3.1.1(a)–3.3.1.1(d) are plotted in Figure 3.3.3.1 for commonly-invoked shallow donors and acceptors in ZnO (shallow donor: interstitial zinc[34] $\left(Zn_i^0\right)$, shallow acceptor: substitutional nitrogen[4] $\left(N_O^{2-}\right)$, see Table 3.3.2.1). These plots expose cases where the dopant-defect resonance is approximately thermoneutral (that is, where ΔE_{DD} is small). The major conclusion drawn from Figure 3.3.3.1 is that dopant-defect hybridization maximizes when the one-electron-reduced (or oxidized) dopant approaches a potential similar to that of the shallow donor (or acceptor). From Figure 3.3.3.1 and Table 3.3.2.1, a near-thermoneutral dopant-defect resonance involving shallow donor or acceptor defects can occur in *p*-type Mn^{2+}:ZnO ($\left|\Delta E_{DD}\right| \approx$ 0.22 eV) and *n*-type Co^{2+}:ZnO ($\left|\Delta E_{DD}\right| \approx 0.27$ eV), but not in *n*-type Mn^{2+}:ZnO (

$|\Delta E_{DD}| \approx 2.7$eV) or *p*-type Co^{2+}:ZnO ($|\Delta E_{DD}| \approx 1.7$ eV). The small ΔE_{DD} values for *p*-type Mn^{2+}:ZnO and *n*-type Co^{2+}:ZnO favor effective hybridization (Eqn. 3.3.3.1)

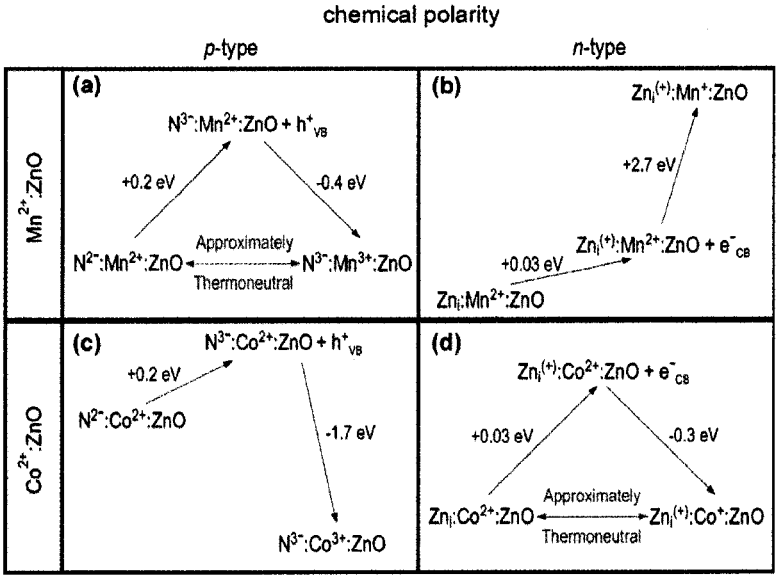

Figure 3.3.3.1. Schematic summary of dopant–donor/acceptor resonance thermodynamics determined from spectroscopic analysis and the binding energies of common shallow donors $\left(Zn_i^0\right)$ or acceptors $\left(N_O^{2-}\right)$ in ZnO. The resulting values of $|\Delta E_{DD}|$ are: **(a)** 0.22, **(b)** 2.7, **(c)** 1.7, and **(d)** 0.27 eV. Resonance is approximately thermoneutral only for *p*-type Mn^{2+}:ZnO and *n*-type Co^{2+}:ZnO. A small $|\Delta E_{DD}|$ favors dopant–donor/acceptor hybridization (Eqn. 3.3.3.1). (Not drawn to scale).

and hence high-T_C ferromagnetism, whereas the large ΔE_{DD} values for *n*-type Mn^{2+}:ZnO and *p*-type Co^{2+}:ZnO limit hybridization and are not favorable for ferromagnetism. The polarity conditions for ferromagnetism predicted by the spectroscopic analysis are thus in agreement with the experimental magnetic results summarized in Figure 3.3.1.1.

The resonance integral of Eqn. 3.3.3.1 is proportional to the spatial overlap of dopant and defect wavefunctions[35,36] which, for fixed concentrations of dopants and defects across the transition metal series, in turn relates to the effective Bohr radii of the limiting charge carriers on each center. Eqn. 3.3.3.2 allows effective Bohr radii for the TM^{n+} and donor/acceptor species in Figure 3.3.3.1 to be estimated.[28,32,37]

$$r_B = \frac{\hbar}{\sqrt{2m^* E_b}} \qquad \text{Eqn. [3.3.3.2]}$$

In Eqn. 3.3.3.2, m^* is the effective mass of the relevant carrier (in ZnO, $m_e^* \approx 0.24m_e$ and $m_h^* \approx 0.45m_e$) and E_b is the binding energy of the last bound carrier. Table 3.3.2.1 summarizes the relevant binding energies and Bohr radii. From the spectroscopic analysis (Figure 3.3.2.2), Co^{+} is a shallow donor and Mn^{3+} a shallow acceptor in ZnO, with carrier binding energies $E_b \approx \Delta E_{n,3}$, whereas Co^{3+} and Mn^{+} are both energetically misaligned with the band structure of ZnO. The Bohr radii for Mn^{+} and Co^{3+} are both substantially smaller than those of Co^{+}, Zn_i^0, Mn^{3+} or N_O^{2-}. Experimental confirmation of this comparison is obtained from the photocurrent IQEs of Figure 3.3.2.1(b), which show that e^- hopping is considerably more favorable than h^+ hopping in photoexcited Co^{2+}:ZnO. Dopant-donor/acceptor hybridization is thus favored by energetic proximity of both to the appropriate band edge of the host semiconductor. In general, although deeper donors or acceptors may be suitable for thermoneutral resonance with deeper magnetic dopants, their smaller Bohr radii would require correspondingly

increased dopant and defect concentrations to achieve sufficient overlap, at which point short-range antiferromagnetic superexchange interactions may become problematic.

To test the broader applicability of this spectroscopic analysis for understanding the magnetic properties of ZnO DMSs, trends in c_{DD} were investigated. For ZnO DMSs prepared under identical conditions, the major changes in c_{DD} across the series of $3d$ TM^{2+} ions occur in the energy denominator, ΔE_{DD}. $L_{VB}MCT$ and $ML_{CB}CT$ energies for the $3d$ TM^{2+} series in ZnO were calculated from Pauling electronegativities and literature ligand field parameters using Eqn. 2.3.1.3 (see Appendix A). Eqn. 2.3.1.3 predicts substantial negative $ML_{CB}CT$ energies for Sc^{2+} and Ti^{2+} in ZnO, consistent with the instability of these ions to spontaneous oxidation. Ti^{2+} and Sc^{2+} are therefore not considered in subsequent analyses.

Figure 3.3.3.2 compares the results of this analysis with available experimental and theoretical magnetic data across the same series. To retain generality, $|1/\Delta E_{n,3}|$ is plotted rather than $|1/\Delta E_{DD}|$, but both yield identical trends for fixed shallow defects. The predicted trends are in excellent overall agreement with the experimental data[12,15], particularly considering the crudeness of the $L_{VB}MCT$ and $ML_{CB}CT$ energy calculations from Eqn. 2.3.1.3 and the potential experimental uncertainties. The predicted trends are also in excellent agreement with available LSDA-DFT results across the series.[2] This agreement is a very strong confirmation that

dopant- donor/acceptor hybridization (that is, exchange mediated by shallow bound carriers) is responsible for ferromagnetism in ZnO DMSs. Of the three factors from

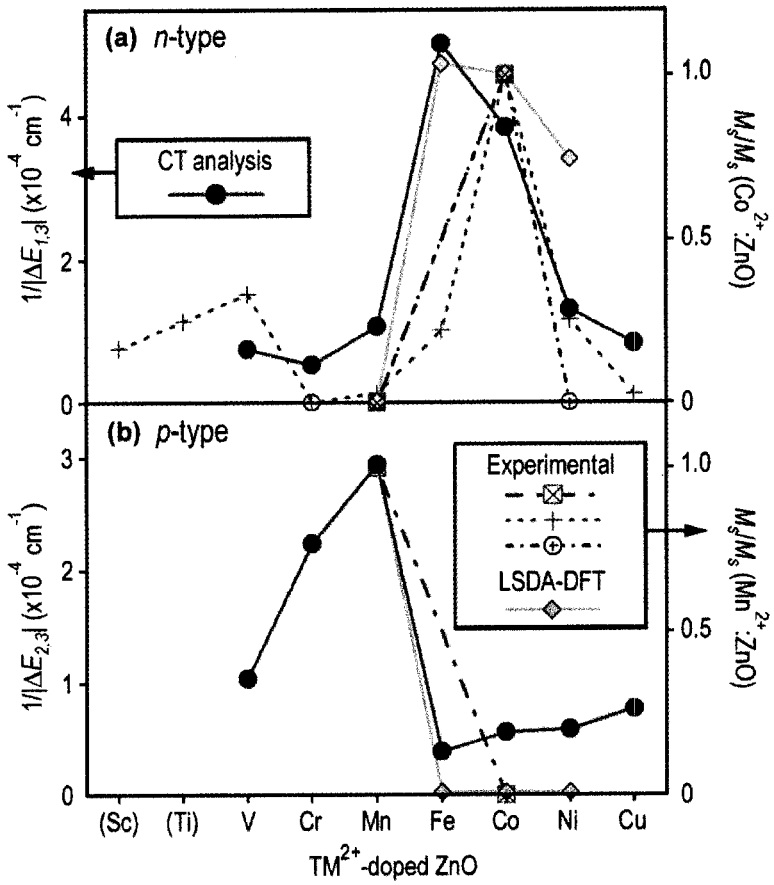

Figure 3.3.3.2. Results of $L_{VB}MCT$ and $ML_{CB}CT$ analysis for the series of TM^{2+}:ZnO DMSs. Calculated trend (●) for **(a)** *n*-type polarity and **(b)** *p*-type polarity. $L_{VB}MCT$ and $ML_{CB}CT$ energies were calculated using Eqn. 2.3.1.3 and are plotted as $|1/\Delta E_{n,3}|$ (left abscissa). Experimental magnetic data are from ref. [15] (⊕), ref. [12] (+), and from Figure 3.3.1.1 (⊠). *Ab initio* LSDA-DFT results are from ref. [2] (♦). For comparison purposes, each literature data set is plotted normalized to the values for Co^{2+}:ZnO in **(a)** and Mn^{2+}:ZnO in **(b)** that were reported for the same data set (right abscissa). Sc and Ti are anticipated to be in the 3+ oxidation state and were therefore not included in the analysis.

Eqn. 2.3.1.3 (electronegativities, spin-pairing energies, and ligand field splittings), spin-pairing energies are primarily responsible for the positions of the maxima and minima in Figure 3.3.3.2. A comprehensive model of both hole- and electron-mediated ferromagnetism in ZnO DMSs therefore must account for Coulomb and electron-electron exchange interactions of the 3*d* ions.

The scenario suggested by this spectroscopic analysis is essentially consistent with the spin-split donor impurity-band model described in ref. [14]. The spectroscopic results demonstrate that Co^{2+} ions can hybridize effectively with shallow-donor impurity bands in ZnO because Co^{+} is also a relatively shallow donor in this lattice, making the Co^{2+}-donor resonance approximately thermoneutral (Figure 3.3.3.1(d), Eqn. 3.3.3.1). Although the donor impurity-band model considered exclusively *n*-type materials, the mechanics of the model are sufficiently general such that it is readily extended to accommodate ferromagnetism involving acceptor impurity bands as well. For this scenario, the spectroscopic results demonstrate that Mn^{2+} can hybridize effectively with shallow-acceptor impurity bands in ZnO because Mn^{3+} is also a relatively shallow acceptor in this lattice (Figure 3.3.3.1(a), Eqn. 3.3.3.1). In both scenarios, strong dopant-defect hybridization favors high-T_C ferromagnetism as described in ref. [14]. Finally, whereas the donor impurity-band model associated trends in the ferromagnetism of *n*-type ZnO DMSs across the 3*d* TM^{2+} series (Figure 3.3.3.2(a)) with a continuous trend in dopant electronegativity, the spectroscopic analysis reveals that the magnetic trends are dominated by the

contributions of electron-electron repulsion, which must be included in addition to electronegativities when estimating energies of multi-electron donor or acceptor configurations (Eqn. 2.3.1.3, Figure 3.3.3.2). Only with the inclusion of electron-electron repulsion terms may the origins of ferromagnetism in *p*-type Mn^{2+}:ZnO be rationalized within this model. These modifications notwithstanding, the central hypothesis of the spin-split impurity-band model, namely that ferromagnetism depends strongly on dopant-donor/acceptor hybridization at the Fermi level, appears to be supported by the spectroscopic data and analysis presented here. We note that although carriers are implicated, this analysis does not imply macroscopic conductivity. The magnetic phase diagrams for carrier-mediated ferromagnetism in ZnO DMSs may possess a region in which the material is both insulating and ferromagnetic. Such a region has been proposed previously for *n*-type oxide DMSs[14] and has been observed experimentally in manganese-doped GaAs[38], where the critical dependence of ferromagnetism on carriers is generally accepted.[1]

3.4 Conclusion

Although this study has focused on ZnO DMSs, similar electronic structural properties also probably govern ferromagnetism in other wide bandgap DMSs. From the spectroscopic analysis, the general conditions conducive to dopant-donor/acceptor hybridization at the Fermi level, and hence to high-T_C ferromagnetism, are (i) approximately thermoneutral dopant-defect resonances (small ΔE_{DD}) and (ii)

energetic proximity of the reduced or oxidized dopant to the semiconductor band structure (small $\Delta E_{n,3}$).

Satisfaction of these conditions can be recognized experimentally by the appearance of dopant-derived donor- or acceptor-type ionization states in close proximity to the band edge of the DMS. Moreover, assignment of these transitions (L_{VB}MCT versus ML_{CB}CT) can reveal the polarity of the carriers that mediate the ferromagnetism (*n*-type versus *p*-type, respectively). L_{VB}MCT or ML_{CB}CT absorption and MCD intensities very near the band edge are indeed observed in $Co^{2+}:TiO_2$[39], $Ni^{2+}:SnO_2$[40], and $Cr^{3+}:TiO_2$[41], all three of which show high-T_C ferromagnetism under appropriate conditions. Careful analysis of the excited states in these and other wide bandgap DMSs, coupled with continued development of sophisticated theoretical models, can therefore be anticipated to provide valuable new insights into the electronic structural origins of polarity dependent high-T_C ferromagnetism in this important class of materials.

3.5 Notes to Chapter 3

[1] Dietl, T.; Ohno, H.; Matsukura, F.; Cibert, J.; Ferrand, D., *Science* **2000**, *287*, 1019.

[2] Sato, K.; Katayama-Yoshida, H., *Semicond. Sci. Technol.* **2002**, *17*, 367.

[3] Pearton, S. J.; Heo, W. H.; Ivill, M.; Norton, D. P.; Steiner, T., *Semicond. Sci. Technol.* **2004**, *19*, R59.

[4] Look, D. C.; Claflin, B., *Phys. Status Solidi B* **2004**, *241*, 624.

[5] Ghosh, S.; Sih, V.; Lau, W. H.; Awschalom, D. D.; Bae, S.-Y., Wang, S.; Vaidya, S.; Chapline, G., *Appl. Phys. Lett.* **2005**, *86*, 232507.

[6] Kittilstved, K. R.; Norberg, N. S.; Gamelin, D. R., *Phys. Rev. Lett.* **2005**, *94*, 147209.

[7] Lim, S.-W.; Jeong, M.-C.; Ham, M.-H.; Myoung, J.-M., *Jpn. J. Appl. Phys.* **2004**, *43*, L280.

[8] Ivill, M.; Pearton, S. J.; Norton, D. P.; Kelly, J.; Hebard, A. F., *J. Appl. Phys.* **2005**, *97*, 053904.

[9] Norberg, N. S.; Kittilstved, K. R.; Amonette, J. E.; Kukkadapu, R. K.; Schwartz, D. A.; Gamelin, D. R., *J. Am. Chem. Soc.* **2004**, *126*, 9387.

[10] Saeki, H.; Tabata, H.; Kawai, T., *Solid State Commun.* **2001**, *120*, 439.

[11] Schwartz, D. A.; Gamelin, D. R., *Adv. Mater.* **2004**, *16*, 2115.

[12] Venkatesan, M.; Fitzgerald, C. B.; Lunney, J. G.; Coey, J. M. D., *Phys. Rev. Lett.* **2004**, *93*, 177206.

[13] Dietl, T., *Nature Mater.* **2003**, *2*, 646.

[14] Coey, J. M. D.; Venkatesan, M.; Fitzgerald, C. B., *Nature Mater.* **2005**, *4*, 173.

[15] Ueda, K.; Tabata, H.; Kawai, T., *Appl. Phys. Lett.* **2001**, *79*, 988.

[16] Kittilstved, K. R.; Gamelin, D. R., *J. Am. Chem. Soc.* **2005**, *127*, 5292.

[17] Petit, L.; Schulthess, T. C.; Svane, A.; Temmerman, W. M.; Szotek, Z., *Mater.*

Res. Soc. Symp. Proc. E **2004**, *825*, G2.9.1.

[18] Wang, Q.; Sun, Q.; Jena, P.; Kawazoe, Y., *Phys. Rev. B* **2004**, *70*, 052408.

[19] Bhattacharjee, A. K., *Phys. Rev. B* **1992**, *46*, 5266.

[20] Kobayashi, M.; Ishida, Y.; Hwang, J. I.; Mizokawa, T., Fujimori, A.; Mamiya, K.; Okamoto, J.; Takeda, Y.; Okane, T.; Saitoh, Y.; Muramatsu, Y.; Tanaka, A.; Saeki, H.; Tabata, H.; Kawai, T., *Phys. Rev. B* **2005**, *72*, 201201.

[21] Liu, W. K.; Salley, G. M.; Gamelin, D. R., *J. Phys. Chem. B* **2005**, *109*, 14486.

[22] Weakliem, H. A., *J. Chem. Phys.* **1962**, *36*, 2117.

[23] Schwartz, D. A.; Norberg, N. S.; Nguyen, Q. P.; Parker, J. M.; Gamelin, D. R., *J. Am. Chem. Soc.* **2003**, *125*, 13205.

[24] Jørgensen, C. K., *Prog. Inorg. Chem.* **1970**, *12*, 101.

[25] Lever, A. B. P., Inorganic Electronic Spectroscopy (Elsevier Science, Amsterdam, 1984).

[26] Mizokawa, T.; Nambu, T.; Fujimori, A.; Fukumura, T.; Kawasaki, M., *Phys. Rev. B* **2002**, *65*, 085209.

[27] Noras, J. M.; Allen, J. W., *J. Phys. C* **1980**, *13*, 3511.

[28] Heitz, R.; Hoffmann, A.; Broser, I., *Phys. Rev. B* **1993**, *48*, 8672.

[29] Bishop, S.G.; Robbins, D. J.; Dean, P. J., *Solid State Commun.* **1980**, *33*, 119.

[30] Müller, B.; Roussos, G.; Schulz, H.-J., *J. Cryst. Growth* **1985**, *72*, 360.

[31] Juhl, A.; Hoffmann, A.; Bimberg, D.; Schulz, H.-J., *Appl. Phys. Lett.* **1987**, *50*, 1292.

[32] Fleurov, V. N.; Kikoin, K. A., *Solid State Commun.* **1982**, *42*, 353.

[33] Wong, W. C.; McClure, D. S.; Basun, S. A.; Kokta, M. R., *Phys. Rev. B* **1995**, *51*, 5682.

[34] Look, D. C.; Hemsky, J. W.; Sizelove, J. R., *Phys. Rev. Lett.* **1999**, *82*, 2552.

[35] Mulliken, R. S., *J. Chem. Phys.* **1955**, *23*, 1841.

[36] Wolfsberg, M.; Helmholz, L., *J. Chem. Phys.* **1952**, *20*, 837.

[37] Shklovskii, B. I., *Sov. Phys. Semicond.* **1973**, *6*, 1053.

[38] Beschoten, B.; Crowell, P. A.; Malajovich, I.; Awschalom, D. D.; Matsukura, F.; Shen, A.; Ohno. H., *Phys. Rev. Lett.* **1999**, *83*, 3073.

[39] Bryan, J. D.; Heald, S. M.; Chambers, S. A.; Gamelin, D. R., *J. Am. Chem. Soc.* **2004**, *126*, 11640.

[40] Archer, P. I.; Radovanovic, P. V.; Heald, S. M.; Gamelin, D. R., *J. Am. Chem. Soc.* **2005**, *127*, 14479.

[41] Bryan, J. D.; Santangelo, S. A.; Keveren, S. C.; Gamelin, D. R., *J. Am. Chem. Soc.* **2005**, *127*, 15568.

Chapter 4: Stable Photogenerated Carriers in Colloidal ZnO and TM^{2+}:ZnO (TM^{2+} = Co^{2+}, Mn^{2+}) Nanocrystals

This chapter describes the use of electron paramagnetic resonance spectroscopy to probe room temperature electron spin dynamics in colloidal pure ZnO quantum dots containing additional quantum-confined conduction band electrons. Some of the work presented in this chapter was performed in collaboration with the research group of Professor Bruce H. Robinson (University of Washington), in particular, Alyssa L. Smith's contribution of deconvoluting the ZnO electron paramagnetic resonance absorption data using algorithms written in MatLab®. The use of electron paramagnetic resonance spectroscopy is extended to probe the coupling between the additional quantum-confined conduction band electrons and magnetic dopant cations in colloidal transition metal (Co^{2+}, Mn^{2+}) doped ZnO nanocrystals.

4.1 Introduction

Electron spins in semiconductor quantum dots are promising candidates for information processing using quantum particles (quantum computation).[1] An attraction of this motif is the slower spin-dephasing expected upon electron confinement. In quantum dots, dephasing mechanisms involving spin-orbit coupling are believed to be suppressed, making electron-nuclear hyperfine coupling the dominant source of spin relaxation.[2,3] The first half of this chapter describes the use of electron paramagnetic resonance spectroscopy to probe electron spin dynamics in

colloidal quantum dots of ZnO, a prototype wide bandgap semiconductor. ZnO is attractive for many potential applications with its well defined doping and defect chemistries, suitability for transparent high-power high-temperature applications, and ability to lase at ultraviolet wavelengths.[4] Recently, relatively long room-temperature ensemble spin-dephasing times ($T_2^* \leq 0.19$ ns at ~290 K) have been measured for bulk and epitaxial *n*-type ZnO using time-resolved Faraday rotation (TRFR) spectroscopy,[5] but to date no studies of spin dynamics in ZnO nanostructures have been reported. In this chapter, spin-dephasing times have been measured at room temperature for colloidal ZnO quantum dots containing between 1 and 6 additional quantum-confined conduction band electrons. The hypothesis that electron-nuclear hyperfine interaction dominate spin-dephasing dynamics is confirmed directly by variation of the ^{67}Zn ($I = 5/2$) content.

Furthermore, colloidal TM^{2+}:ZnO (TM^{2+} = Co^{2+}, Mn^{2+}) nanocrystals containing additional quantum-confined conduction band electrons have been prepared. Although charged[6-8] and magnetically doped[9] colloidal semiconductor nanocrystals have been reported separately, colloidal nanocrystals that have been both charged and magnetically doped as described herein have not. The relevance of examining the TM^{2+}-e^-_{CB} exchange interactions in these materials lies in the pivotal role in which carrier-dopant interaction gives rise to the many observed magneto-electronic phenomena, including carrier-mediated ferromagnetism,[10]

magnetic polaron nucleation,[11] and coherent spin injection.[12] This new motif presents unexplored opportunities for investigation of carrier-dopant interactions in diluted magnetic semiconductor nanostructures. The remainder of this chapter describes the use of electron paramagnetic resonance spectroscopy to probe the exchange coupling between the additional electrons and the magnetic dopants in diluted magnetic semiconductors.

4.2 Experimental

Alkyl-capped (Alkyl = trioctylphosphine oxide or dodecylamine) colloidal nanocrystals of pure ZnO and TM^{2+}:ZnO (TM^{2+} = Co^{2+}, Mn^{2+}) were synthesized as described previously in Chapter 2 and 3. ^{67}Zn-enriched zinc acetate (^{67}Zn(9.60%), 99.8%, Trace Sciences International, see Appendix B for zinc isotope distribution) was used for the synthesis of ^{67}Zn-enriched ZnO. Samples for photochemical reduction experiments were prepared by evaporating the solvent from the desired colloidal suspension to obtain a dry powder. The powder was transferred into a glovebox, resuspended in a degassed and anhydrous toluene/ethanol (98:2 vol:vol) mixture, and sealed under inert atmosphere in either a quartz sample tube or a spectroscopic cell.

Photochemical reduction of the colloidal nanocrystals was achieved by all-lines ultraviolet irradiation with an argon gas laser (333-364 nm, BeamLok 2060 Spectra Physics). Electronic absorption spectra were collected using a Cary 5E (Varian) spectrophotometer. Infrared (IR) absorption spectra were collected using a

Perkin-Elmer 1720 FTIR with the sample in a 15 μm pathlength CaF_2 cell. *X*-band (9.5 GHz) electron paramagnetic resonance (EPR) spectra were collected on a Bruker EMX EPR spectrometer. Dopant concentrations were determined by inductively coupled plasma atomic emission spectrometry (ICP-AES, Jarrel Ash model 995).

4.3 Results and Discussion

4.3.1 Room-Temperature Electron Spin Dynamics in Colloidal ZnO Quantum Dots

Figure 4.3.1.1(a) shows a photograph of as-prepared (ZnO) and charged ($e_{CB}^{-}:\mathrm{ZnO}$) colloidal ZnO quantum dots. Figure 4.3.1.1(b) shows 298 K electronic absorption spectra collected before and after ultraviolet (UV) irradiation. With irradiation, the first excitonic peak in the UV was bleached, and a broad near-infrared (NIR) absorption band of comparable oscillator strength appeared. The bluish hue visible by eye in the charged nanocrystals is due to tailing of this NIR band into the visible region. These spectral changes, prominent in the absorption difference spectrum (charged–as-prepared, Figure 4.3.1.1(c)), agree well with those reported previously.[7,8,13] The UV bleaching has been attributed to electron filling of the conduction band, and the new NIR intensity to dipole allowed intra-conduction band excitation.[7,8] The multiple sharp absorption peaks in the NIR are solvent vibrational overtones. When kept anaerobic, the charged ZnO nanocrystals are kinetically very stable (k_{decay}<0.01/week at 298 K), but they return rapidly and completely to their initial forms upon exposure to air (gray dotted line in Figure 4.3.1.1(b),(c)]. This facile

reversibility demonstrates that no photodegradation occurs under these charging conditions.

Figure 4.3.1.1(d) shows the 298 K *X*-band (9.5 GHz) EPR spectra of colloidal ZnO nanocrystals before and after charging. The as-prepared ZnO nanocrystals showed no EPR signal. After UV irradiation, an intense new EPR signal at $g^* \approx 1.96$

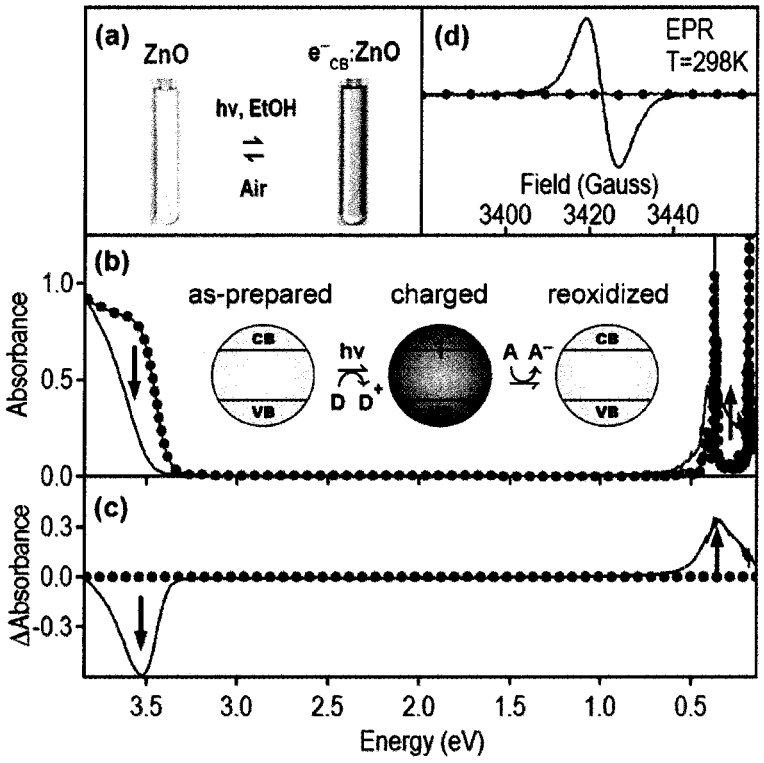

Figure 4.3.1.1. **(a)** Photographs of as-prepared and charged colloidal ZnO quantum dots. **(b)** The 298 K absorption spectra of as-prepared (red line), charged (blue line), and reoxidized (dotted gray line) colloidal ZnO quantum dots. **(c)** Difference absorption spectra showing UV bleaching and IR absorption with charging (blue line) and reversal with reoxidation (dotted gray line). **(d)** The 298 K EPR spectra of as-prepared (red line), charged (blue line), and reoxidized (dotted gray line) colloidal ZnO quantum dots.

was detected, similar to those reported in nano- and microcrystalline aggregates of ZnO.[14-16] Since *n*-type grain-boundary defects are abundant in ZnO aggregates and may severely complicate analysis of their EPR spectra, TOPO-capped ZnO nanocrystals[13,17] were used here to ensure that the physical properties observed are those of the freestanding quantum dots. The deviation from $g_e = 2.0023$ indicates that the new EPR signal in Figure 4.3.1.1(d) does not originate from deeply trapped electrons. From $K \cdot P$ treatment of the ZnO band structure (Eqn. 4.3.1.1),[16,18] the reduction of g^* derives from the combination of interband mixing (P) and spin-orbit coupling (Δ), both of which are relatively small in ZnO. From Eqn. 4.3.1.1, g^* also depends on quantum dot diameter since the energy gap (E_g) is size dependent.[16,18] As with the NIR absorption, the $g^* = 1.96$ signal disappeared upon exposure of the charged quantum dots to air (Figure 4.3.1.1(d)). Collectively, the data in Figure 4.3.1.1 confirm that the added electrons reside in the ZnO quantum dot conduction band. One electron in a $d = 4.6$ nm quantum dot corresponds to a carrier density of 2×10^{19} cm^{-3}.

$$g^* = g_e - \frac{2}{3}\left(\frac{P^2\Delta}{E_g\left(E_g + \Delta\right)}\right) \qquad \text{Eqn. [4.3.1.1]}$$

Both the NIR absorption and $g^* = 1.96$ EPR intensities increase with increasing UV irradiation times. Interestingly, plots of EPR vs NIR intensities are not linear. To understand this observation, the average number of electrons per ZnO nanocrystal $(\langle n \rangle)$ was determined for several samples by titration with recrystallized methyl

viologen dichloride (see Appendix B).[19] Whereas the rate of change of the integrated NIR intensity increases slightly with increasing $\langle n \rangle$, the data in Figure 4.3.1.2(a) show a pronounced curvature in the EPR intensity with increasing $\langle n \rangle$. Tight-binding calculations[20] describe the lowest conduction energy levels of ZnO quantum dots as having *S*, *P*, and *D* symmetries with orbital degeneracies of 2, 6, and 10, respectively. To analyze the data in Figure 4.3.1.2(a), it was assumed that electron filling of these levels in each quantum dot follows the Aufbau principle (as observed with electrochemical charging)[20] and Hund's rules, and that Poissonian statistics govern electron distributions over the ensemble of quantum dots. To test these assumptions, spin-weighted Poissonian population distributions were calculated using Eqn. 4.3.1.2. Here, *n* is the number of electrons in a given quantum dot and represents the number of possible EPR transitions allowed ($\Delta M_s = \pm 1$) in the resulting multi-electron configuration. Thus Eqn. 4.3.1.2 allows estimation of the EPR intensity as a function of average electron occupancy $\langle n \rangle$ within the Poissonian filling model.

$$P(\alpha; n; \langle n \rangle) = \alpha \frac{\langle n \rangle^n e^{-\langle n \rangle}}{n!} \qquad \text{Eqn. [4.3.1.2]}$$

The sum of spin-weighted populations calculated for all of the EPR active configurations [$S(S = ½)$, $P(S = ½, 1, 3/2)$, and $D(S = ½, 1, 3/2, 2, 5/2)$] is plotted vs $\langle n \rangle$ in Figure 4.3.1.2(b). The calculated curve reproduces the experimental data (Figure 4.3.1.2(a)) remarkably well. The minor differences in curvature are reasonable

given the simplicity of the model, since non-Poissonian populations due to the finite particle size distribution may be reasonably anticipated. Notably, curves calculated excluding either $S = 1$ (non-Kramers) or all $S > \frac{1}{2}$ configurations fail to reproduce the

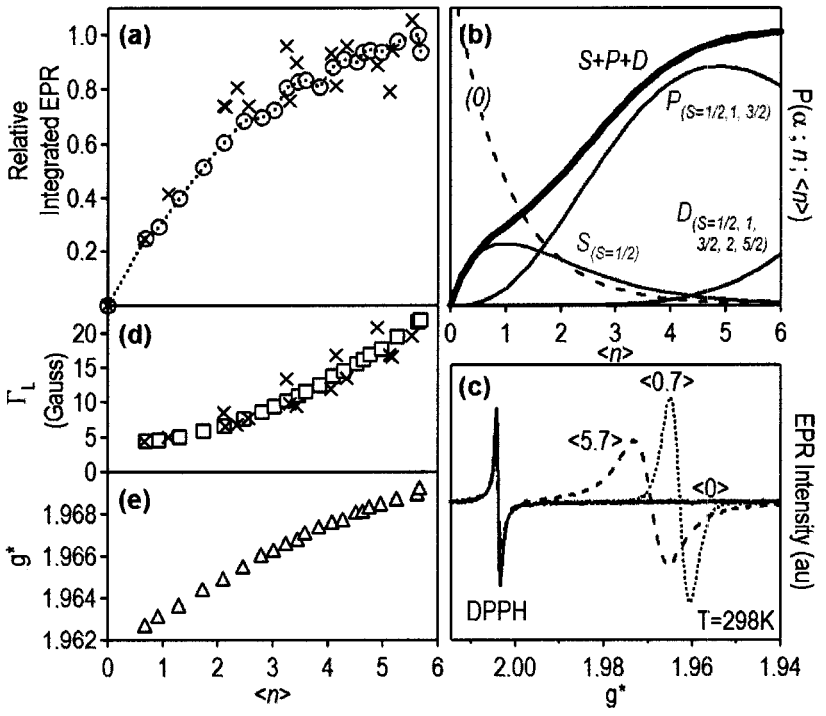

Figure 4.3.1.2. EPR spectra of colloidal ZnO quantum dots (d = 4.60 ± 0.4 nm, 298 K) as a function of $\langle n \rangle$. **(a)** Relative double integration of the first-derivative EPR intensities. Data for which $\langle n \rangle$ was determined by chemical titration are marked x. **(b)** Spin-weighted Poissonian probabilities for S, P, and D filling in an ensemble of ZnO quantum dots. **(c)** EPR spectra of as-prepared (solid line), low $\langle n \rangle$ (dotted line), and high $\langle n \rangle$ (dashed line) ZnO quantum dots (DPPH internal standard, g = 2.0037 ± 0.0002). **(d)** Lorentzian line widths. **(e)** e^-_{CB} g^* values.

experimental curvature of Figure 4.3.1.2(a) adequately (see Appendix B), suggesting that zero-field splittings of the $S > \frac{1}{2}$ configurations are small relative to the X-band

photon energy. The curvature in Figure 4.3.1.2(a) thus ultimately reflects differences between *unpaired* and *total* $(\langle n \rangle)$ electron populations in charged quantum dots with level filling governed predominantly by Poissonian statistics. These conclusions are supported by use of the same statistical model to analyze the change in NIR intensity with $\langle n \rangle$ (see Appendix B), which yields ~0.25 for the relative *S-P:P-D* oscillator strengths, in good agreement with the published ratio (~0:33).[8]

The e_{CB}^- EPR signal is substantially broader than that of the internal reference DPPH (diphenylpicrylhydrazyl radical) at all values of $\langle n \rangle$ (Figure 4.3.1.2(c)). Although the EPR lineshapes are nearly Lorentzian, analysis reveals some inhomogeneous broadening, as might be expected from the finite quantum dot size distribution and the size dependence of g^* (Eqn. 4.3.1.1). For analysis of the linewidths, the homogeneous (Γ_L, Lorentzian full-width at half-height) and inhomogeneous ($\Gamma_{\Delta g^*}$, Gaussian standard deviation) contributions to the lineshape in each EPR spectrum were therefore deconvolved. The resulting homogeneous linewidths are plotted vs $\langle n \rangle$ in Figure 4.3.1.2(d). Whereas Γ_L increases with increasing $\langle n \rangle$, $\Gamma_{\Delta g^*}$ remains small and nearly constant ($1.5 < \Gamma_{\Delta g^*} < 3.3$ G) over the entire range of $\langle n \rangle$ (see Appendix B).[21] This broadening and the concomitant g^* shift (Figure 4.3.1.2(e)) with increasing $\langle n \rangle$ are discussed in more detail below.

The e_{CB}^{-} :ZnO EPR linewidths are of fundamental importance since they directly reflect electron spin dynamics. The longitudinal relaxation time (T_1) for the charged ZnO quantum dots was investigated by pulse saturation recovery (Figure 4.3.1.3(a))[22] and saturation rollover EPR measurements (not shown). Both experiments show T_1 to be on the microsecond time scale (~240 ns) at 298 K, which is comparable to the previously measured T_2^* ($\leq$0.19 ns at 290 K) for ZnO.[5] Therefore, the governing process to the overall relaxation rate is spin-spin relaxation as given by Eqn. 4.3.1.3.[23]

$$T_{Total} = T_2 + 2T_1 \qquad \text{Eqn. [4.3.1.3]}$$

To a good approximation, Γ_L is then related to the spin-dephasing time T_2 according to Eqn. 4.3.1.4. From $\Gamma_L = 4.54$ G measured for $\langle n \rangle = 0.7$ at 298 K, $T_2 = 25$ ns is determined.

$$T_2 = \frac{2\hbar}{g_e \mu_B \Gamma_L} \qquad \text{Eqn. [4.3.1.4]}$$

In GaAs, InAs, and CdSe quantum dots, spin dephasing has been associated with the electron-nuclear hyperfine interaction,[2,3] which is large in these lattices because many of their ions have nuclear spin. In contrast to the semiconductors mentioned above, the vast majority of cations and anions in ZnO have $I = 0$. Only ^{67}Zn ($I = 5/2$, 4.1% natural abundance) may contribute significantly to spin dephasing via the hyperfine interaction. To test the hypothesis that the linewidth shown in Figure

4.3.1.2 depends on electron-nuclear hyperfine coupling, a series of 4.0 ± 0.4 nm diameter nanocrystal samples having different average ^{67}Zn contents $\left(\left\langle {}^{67}\mathrm{Zn}\right\rangle\right)$ have

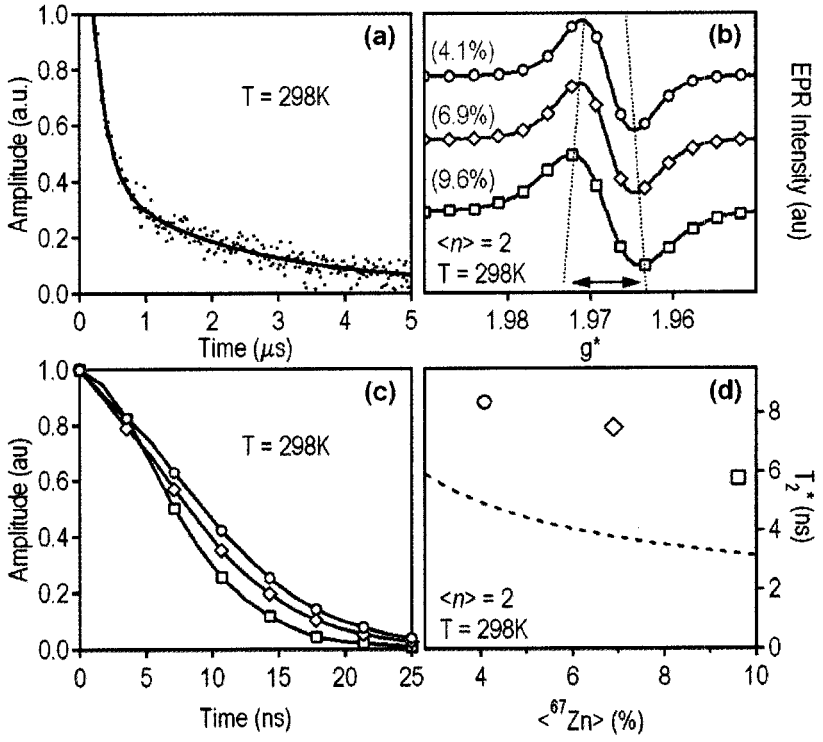

Figure 4.3.1.3. (a) Pulse saturation recovery EPR data for natural abundance ZnO quantum dots. The solid line shows a biexponential best fit with $\tau_a = 0.24$ and $\tau_b = 2.7$ μs. **(b)** e^-_{CB} : ZnO quantum dot EPR signal as a function of $\left\langle {}^{67}\mathrm{Zn}\right\rangle$ for $d = 4.0 \pm 4$ nm quantum dots with $\langle n \rangle = 2$. (○) 4.1% (natural abundance), (◇) 6.8%, and (□) 9.6% ^{67}Zn. The dotted lines are guides to the eye. **(c)** Fourier transforms of EPR absorption spectra from (b). **(d)** Plot of T_2^* vs $\left\langle {}^{67}\mathrm{Zn}\right\rangle$ for the data from (b) including the calculated results of Eqn. 4.3.1.5 (black dashed line).

been synthesized by starting from ^{67}Zn-enriched $Zn(OAc)_2$ precursors. Each sample was prepared and charged to $\langle n \rangle = 2$ under identical conditions. The resulting EPR

spectra are plotted in Figure 4.3.1.3(b). Clearly, increasing $\langle {}^{67}\mathrm{Zn} \rangle$ from 4.1 to 9.6% increases the linewidth substantially. This increase corresponds to a decreased spin-dephasing time, as evident from plots of the Fourier transformed EPR absorption spectra for the same three samples (Figure 4.3.1.3(c)). To quantify the extent to which $\langle {}^{67}\mathrm{Zn} \rangle$ concentration influences spin-dephasing, the Fourier transformed EPR absorption spectra in Figure 4.3.1.3(c) were fitted to an exponential decay curve to yield the ensemble spin-dephasing time, T_2^*. Figure 4.3.1.3(d) plots T_2^* vs $\langle {}^{67}\mathrm{Zn} \rangle$ for the three $\langle n \rangle = 2$ quantum dot samples from Figure 4.3.1.3(b). T_2^* decreases from 8 to 6 ns upon increasing $\langle {}^{67}\mathrm{Zn} \rangle$ from 4.1 to 9.6%. The T_2^* for ZnO quantum dots with $\langle n \rangle = 2$ and $\langle {}^{67}\mathrm{Zn} \rangle = 4.1\%$, is ~40 times greater than those measured for bulk and epitaxial *n*-type ZnO by TRFR spectroscopy at 290 K ($T_2^* \leq 0.19$ ns).[5]

Following ref. [2], the ensemble spin-dephasing time, T_2^*, for the three different $\langle {}^{67}\mathrm{Zn} \rangle$ concentrations was calculated using Eqn. 4.3.1.5 and plotted in Figure 4.3.1.3(d). The T_2^* in this scenario depends on the strength and number of hyperfine interactions in the quantum dot as described by Eqn. 4.3.1.5,

$$T_2^* = \hbar \sqrt{\frac{3N_L}{2n\sum_j I^j \left(I^j+1\right)\left(A^j\right)^2}} \qquad \text{Eqn. [4.3.1.5]}$$

where N_L is the total number of ions in the quantum dot, n is the number of ions in the unit cell, I^j is the nuclear spin on the j-th ion, A^j is the hyperfine coupling constant at

the j-th ion, and the sum is over all ions in the unit cell.

The isotropic hyperfine coupling for an electron localized on ^{67}Zn has been reported as $A(^{67}\text{Zn}) = 5.17\ \mu\text{eV}$.[23] With $N_L \approx 2800$ (for a 4.0 nm average diameter quantum dot), Eqn. 4.3.1.5 yields $T_2^* = 4.9$, 3.8, and 3.2 ns for the 4.1, 6.8, and 9.6% $\langle ^{67}\text{Zn} \rangle$, respectively. Although the calculated T_2^* values are a factor of ~2 smaller than the experimental values, they are in reasonable agreement given that (i) covalency will decrease $A(^{67}\text{Zn})$ and (ii) crystal shape anisotropy may cause the real e_{CB}^- wave function to deviate from the idealized wave function assumed in derivation of Eqn. 4.3.1.5.[2] The experimental trend in Figure 4.3.1.3 indicate that long room temperature electron spin-dephasing times can be achieved in quantum dots by chemical modification to eliminate ions with $I \neq 0$.

In addition to hyperfine coupling, overcharging (quantum dot containing more than 1 conduction band electron) is very effective in reducing T_2. Plot of T_2 for the same quantum dot sample ($d = 4.60 \pm 0.4$ nm) at charging levels from $\langle n \rangle = 0.7$ to 5.7 (from Figure 4.3.1.4), showing T_2 reduction from 25 to 5 ns. Although quantitative analysis is complicated by the ensemble nature of the experiment, it is evident from comparison of Figures 4.3.1.2(b) and 4.3.1.2(d) that T_2 decreases as the unpaired e_{CB}^- population shifts from predominantly S to predominantly P configurations. Since line broadening occurs only above $\langle n \rangle \approx 1.5$, where multi-electron P configurations begin to appear, it is concluded that spin-spin relaxation mechanisms are predominantly

responsible for the reduction in T_2 with increasing $\langle n \rangle$. Finally, the data in Figure 4.3.1.2(e) reveal that g^* is greater for P electrons than for an unpaired S electron. The

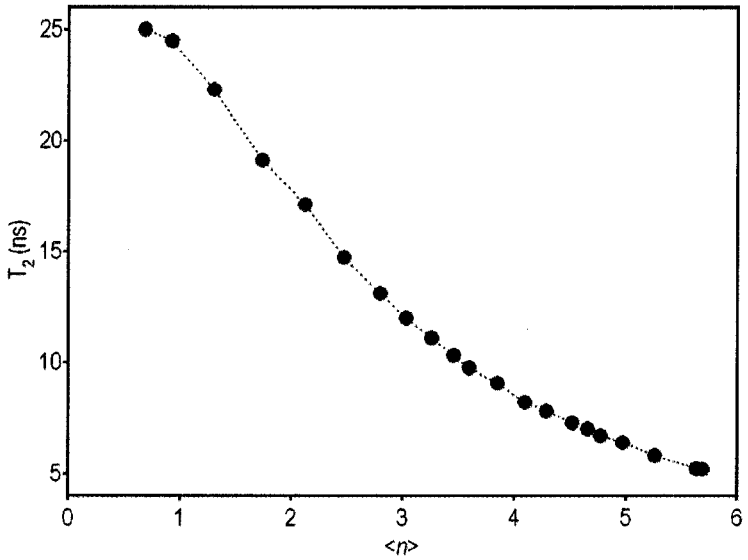

Figure 4.3.1.4. T_2 for the same quantum dot sample (d = 4.60 ± 0.4 nm) at charging levels from $\langle n \rangle$ = 0.7 to 5.7 determined using Eqn. 4.3.1.4 and Γ_L from Figure 4.3.1.2(d).

Poissonian analysis allows resolution of individual g^* values from the data in Figure 4.3.1.2(e), yielding $g^*(S^1)$ = 1.962 and $g^*(S^2P^1)$ = 1.971. This increase is also evident from the comparison of g^* = 1.968 at $\langle n \rangle$ = 4.4 where ~93% of the EPR intensity derives from P configurations, with g^* = 1.963 at $\langle n \rangle$ = 0.7 where ~86% of the EPR intensity derives from the S^1 configuration. The increasing g^* may reflect contributions from orbital angular momentum in the P configurations. Indeed, calculations on spherical ZnO nanocrystals within the multiband effective mass approximation have

predicted substantial orbital effective Landé g factors for P electrons (l = 1).[18] A detailed analysis of these highly charged quantum dots is complex and beyond the scope of this chapter, but it may be of interest for future studies.

4.3.2 Photochemical Reduction of Colloidal TM^{2+}:ZnO (TM^{2+} = Co^{2+}, Mn^{2+}) Nanocrystals

Figure 4.3.2.1(a),(b) shows 298 K electronic absorption spectra of 2.6% Co^{2+}:ZnO nanocrystals suspended in toluene (with small amount of ethanol, ~2% of the total volume) in their as-prepared and charged forms. With charging, the first excitonic peak in the UV was bleached, and an intense NIR band appeared, as reported previously for pure ZnO colloids and observed in Section 4.3.1.[7] The UV bleaching has been attributed to partial filling of the conduction band (CB) and the new NIR intensity to dipole-allowed intra-CB transitions.[7,8] Together, these spectral changes are the signature of CB electrons (e^-_{CB}).[24]

Figure 4.3.2.1(c),(e) shows 298 K electronic absorption spectra of concentrated suspensions of 4.2% Co^{2+}:ZnO and 0.8% Mn^{2+}:ZnO colloids in toluene in their as-prepared and reduced forms. The sub-bandgap absorption spectra of the as-prepared DMS nanocrystals have been described previously.[17,25] With photoreduction, both suspensions exhibited the signature UV bleaching and NIR absorption (e.g., Figure 4.3.2.1(a),(b)). For Co^{2+}:ZnO, the difference spectrum (charged–as-prepared, Figure 4.3.2.1(d)) shows no other features. Notably, there was no detectable change in the

$^4A_2 \rightarrow {}^4T_1(P)$ or $^4T_1(F)$ intensities centered at 16500 and 7200 cm^{-1}, respectively

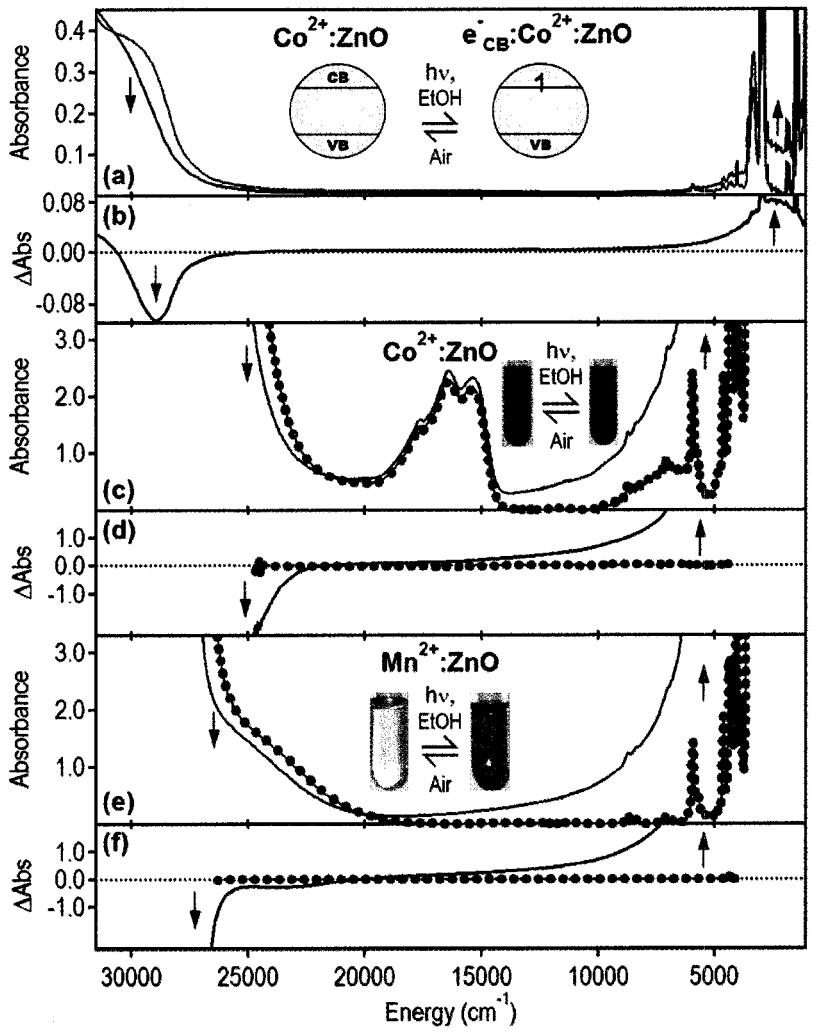

Figure 4.3.2.1. The 298 K absorption **(a, c, e)** and difference absorption **(b, d, f)** spectra of 4.5 ± 0.2 nm diameter nanocrystals: as-prepared (red line), photoreduced (blue line), and reoxidized (gray dotted line): **(a, b)** 2.6% Co^{2+}:ZnO, dilute; **(c, d)** 4.2% Co^{2+}:ZnO, concentrated; **(e, f)** 0.8% Mn^{2+}: ZnO, concentrated.

(ΔAbs < 0.8%), demonstrating that Co^+ is not formed at appreciable concentrations under these conditions (Co^+ cation mole fraction <0.03%). Because the as-prepared

Co^{2+}:ZnO nanocrystals are already blue from the $^4A_2 \rightarrow {}^4T_1(P)$ ligand field absorption, they do not color significantly upon charging.

For Mn^{2+}:ZnO, bleaching was also observed at ~24000 cm^{-1} upon photoreduction (Figure 4.3.2.1(e),(f)). Absorption and magnetic circular dichroism spectroscopies have previously identified the 24000 cm^{-1} band as a donor-type photoionization transition involving promotion of a Mn^{2+} electron into the CB.[25] Bleaching of this $Mn^{2+} \rightarrow$ CB transition is consistent with CB filling and may also reflect suppression of its intensity-stealing mechanism, which involves configuration interaction with the nearby excitonic levels.[26] The spectral changes in Figure 4.3.2.1(e) result in coloration of the Mn^{2+}:ZnO nanocrystals from yellow/brown (as-prepared) to emerald green (charged). In all cases, the reduced nanocrystals were stable indefinitely (k_{decay} < 0.01/week at 298 K) when kept anaerobic but returned rapidly to their original forms upon exposure to air (gray dots in Figure 4.3.2.1), consistent with facile reoxidation.

EPR spectroscopy was also used to study the reduced nanocrystals. Figure 4.3.2.2(a) shows 298 K EPR spectra of as-prepared and charged colloidal ZnO nanocrystals. The as-prepared ZnO nanocrystals showed no EPR signal. A new $g^* = 1.96$ signal was detected after photoreduction (Figure 4.3.2.2(a)) similar to that reported for shallow donors in nanocrystalline ZnO.[15,16] A detailed description of this EPR spectrum for undoped ZnO nanocrystals was discussed previously in Chapter 4 Section 4.3.1.

Figure 4.3.2.2(b) shows 298 K EPR spectra of as-prepared and charged Co^{2+}:ZnO nanocrystals at various Co^{2+} cation percent mole fractions (x). At 298 K, as-prepared Co^{2+}:ZnO shows no EPR signal due to rapid Co^{2+} spin-lattice

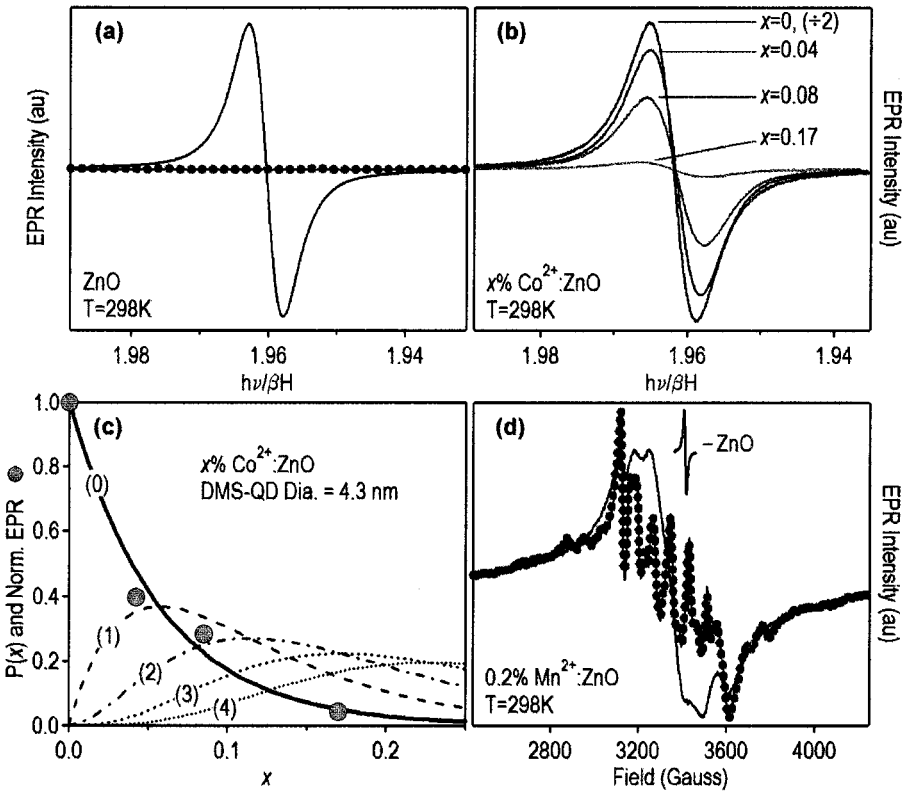

Figure 4.3.2.2. The 298 K EPR spectra of as-prepared (red line), reduced (blue line), and reoxidized (gray dotted line) colloidal nanocrystals: **(a)** ~4.1 nm diameter ZnO nanocrystals; **(b)** ~4.3 nm diameter x %Co^{2+}:ZnO nanocrystals after photoreduction; **(c)** EPR intensity from part (b) plotted versus x. Curves show statistical probabilities calculated for 0-4 dopants/particle; **(d)** ~8.0 nm diameter 0.2% Mn^{2+}:ZnO nanocrystals, with inset showing the reduced ZnO EPR spectrum from part (a) on the same x axis.

relaxation,[27] making this system amenable to observation of e^-_{CB} upon

photoreduction. For small x, a $g^* = 1.96$ EPR signal was detected after photoreduction (Figure 4.3.2.2(b)) identical to the one observed in Figure 4.3.2.2(a). With increasing x, this EPR signal weakened substantially, despite clear evidence of nanocrystal charging from absorption spectroscopy (e.g., Figure 4.3.2.1(a)-(d)). A plot of EPR intensity versus x (Figure 4.3.2.2(c)) for a series of nanocrystals reduced under identical conditions reveals that the EPR intensity correlates quantitatively with the fraction of undoped ZnO nanocrystals calculated from Poisson statistics.[9] A single Co^{2+} ion thus completely suppresses the e^-_{CB} EPR signal under these conditions, likely by lifetime broadening due to Co^{2+}-e^-_{CB} coupling.

Figure 4.3.2.2(d) shows EPR spectra of as-prepared and reduced 0.2% Mn^{2+}:ZnO nanocrystals. In contrast with Co^{2+}, Mn^{2+} in ZnO relaxes slowly[27] and shows a strong EPR signal at 298 K with extensive hyperfine structure described by the axial spin Hamiltonian parameters $g_{iso} = 1.999$, $A_{iso} = -74.0\times10^{-4}$ cm^{-1}, and $D = -2.36\times10^{-2}$ cm^{-1}.[25] This structure broadened substantially upon reduction, a change that was quantitatively reversed by exposure to air (dotted line in Figure 4.3.2.2(d)). Importantly, the spectrum of reduced Mn^{2+}:ZnO nanocrystals is not the simple sum of Mn^{2+} and e^-_{CB} spectra, indicating substantial Mn^{2+}-e^-_{CB} interaction. To estimate the effective (mean-field) Mn^{2+}-e^-_{CB} exchange energy, the line broadening of Figure 4.3.2.2(d) was analyzed. Assuming the Mn^{2+} line broadening ($\Delta\Gamma$) arises solely from exchange splitting of each Mn^{2+} hyperfine peak by interaction with the $S = \frac{1}{2}$ e^-_{CB}, a

mean Mn^{2+} level splitting of 40 G (0.23 μeV or 1.9×10^{-3} cm^{-1}) is estimated. The total exchange energy experienced by e_{CB}^{-} is the sum over all Mn^{2+}-e_{CB}^{-} interactions. For 8.0 nm diameter 0.2% Mn^{2+}:ZnO nanocrystals, the mean Mn^{2+} occupancy is $\langle TM \rangle$ = 22.5, so $\Delta E\left(e_{CB}^{-}\right) \approx 4.3\times10^{-2}$ cm^{-1}. This result can be related to the mean-field exchange parameter $N_0\alpha$ typically used to describe TM^{2+}-e_{CB}^{-} coupling in bulk DMSs[10] via Eqn. 4.3.2.1,

$$\left|N_0\alpha\right| = \left|\frac{\Delta E}{x\langle S_z\rangle}\right| \approx \left|\frac{\langle TM\rangle \Delta\Gamma}{x\langle S_z\rangle}\right| \qquad \text{Eqn. [4.3.2.1]}$$

where $\left|\langle S_z\rangle\right|$ = 0.004 is the Mn^{2+} spin expectation value under the experimental conditions of 298 K and ~0.33 T used for Figure 4.3.2.2(d). Solving Eqn. 4.3.2.1 yields $\left|N_0\alpha\right|$ = 0.66 eV, a value comparable to those reported[10] for bulk Mn^{2+}:ZnSe (+0.26 eV), Mn^{2+}:ZnTe (+0.18 eV), and Mn^{2+}:CdSe (+0.26 eV), as well as that used to model magneto-transport in Mn^{2+}: ZnO films (+0.19 eV).[28] Although reasonable in magnitude, this experimental estimate neglects Mn^{2+} relaxation broadening[29] and makes no attempt to account for nonstatistical dopant distributions,[9,17] carrier-mediated Mn^{2+}-Mn^{2+} exchange coupling,[28] or nanocrystal overcharging,[8] all of which should be important variables. Nevertheless, the data in Figure 4.3.2.2 clearly demonstrate both the existence of TM^{2+}-e_{CB}^{-} exchange interactions in charged DMS nanocrystals and the possibility to study these interactions spectroscopically.

4.4 Conclusion

In summary, conduction band electrons have been successfully introduced into colloidal undoped ZnO and TM^{2+}:ZnO (TM^{2+} = Co^{2+}, Mn^{2+}) semiconductor nanocrystals as indicated by the distinctive changes in the electronic absorption spectra and the appearance of a new EPR signal. The electron spin dynamics in undoped ZnO quantum dots have been probed by EPR spectroscopy. T_2 values up to 25 ns at 298 K have been observed, and a clear relationship between T_2^* and e_{CB}^- - ^{67}Zn hyperfine coupling has been demonstrated. These results point to chemical control over $\langle {}^{67}\mathrm{Zn} \rangle$ as a promising avenue for increasing electron spin-coherence times in ZnO quantum dots. Long spin-coherence remains a sought after property in semiconductors.

In addition, manifestations of TM^{2+} - e_{CB}^- interactions have been observed by EPR spectroscopy. For the case of Co^{2+}:ZnO the TM^{2+} - e_{CB}^- exchange interaction led to rapid quenching of the e_{CB}^- EPR signal. For the case of Mn^{2+}:ZnO, however, TM^{2+} - e_{CB}^- exchange interaction resulted in considerable broadening of the Mn^{2+} hyperfine peaks. In a broader view, extension of this research to other DMSs and nanocrystal dimensionalities is expected to reveal interesting new phenomena relevant to future spin-based information processing applications.

4.5 Notes to Chapter 4

[1] Cerletti, V.; Coish, W. A.; Gywat, O.; Loss, D., *Nanotechnology* **2005**, *16*, R27, and references therein.

[2] Merkulov, I. A.; Efros, A. L.; Rosen, M., *Phys. Rev. B* **2002**, *65*, 205309.

[3] Braun, P.-F.; Marie, X.; Lombez, L.; Urbaszek, B.; Amand, T.; Renucci, P.; Kalevich, V. K.; Kavokin, K. V.; Krebs, O.; Voisin, P.; Matsumoto, Y., *Phys. Rev. Lett.* **2005**, *94*, 116601.

[4] Look, D. C.; Claflin, B., *Phys. Status Solidi (b)* **2004**, *241*, 624.

[5] Ghosh, S.; Sih, V.; Lau, W. H.; Awschalom, D. D.; Bae, S.-Y.; Wang, S.; Vaidya, S.; Chapline, G., *Appl. Phys. Lett.* **2005**, *86*, 232507.

[6] Hasse, M.; Weller, H.; Henglein, A., *J. Phys. Chem.* **1988**, *92*, 482.

[7] (a) Shim, M.; Guyot-Sionnest, P., *J. Am. Chem. Soc.* **2001**, *123*, 11651. (b) Shim, M.; Guyot-Sionnest, P., *Nature* **2000**, *407*, 981.

[8] Germeau, A.; Roest, A. L.; Vanmaekelbergh, D.; Allan, G.; Delerue, C.; Meulenkamp, E. A., *Phys. Rev. Lett.* **2003**, *90*, 097401.

[9] For a recent review, see: Bryan, J. D.; Gamelin, D. R., *Prog. Inorg. Chem.* **2005**, *54*, 47.

[10] Furdyna, J. K., *J. Appl. Phys.* **1988**, *64*, R29.

[11] Coey, J. M. D.; Venkatesan, M.; Fitzgerald, C. B., *Nature Mater.* **2005**, *4*, 173.

[12] Fiederling, R.; Keim, M.; Reuscher, G.; Ossau, W.; Schmidt, G.; Waag, A.; Molenkamp, L. W., *Nature* **1999**, *402*, 787.

[13] Liu, W. K.; Whitaker, K. M.; Kittilstved, K. R.; Gamelin, D. R., *J. Am. Chem. Soc.* **2006**, *128*, 3910.

[14] Cunningham, J.; Corkery, S.; *J. Phys. Chem.* **1975**, *79*, 933.

[15] Orlinskii, S. B.; Schmidt, J.; Baranov, P. G.; Hofmann, D. M.; de Mello Donegá, C.; Meijerink, A., *Phys. Rev. Lett.* **2004**, *92*, 047603.

[16] Zhou, H.; Hofstaetter, A.; Hofmann, D. M.; Meyer, B. K., *Microelectron. Eng.* **2003**, *66*, 59.

[17] Schwartz, D. A.; Norberg, N. S.; Nguyen, Q. P.; Parker, J. M.; Gamelin, D. R., *J. Am. Chem. Soc.* **2003**, *125*, 13205.

[18] Rodina, A. V.; Efros, A. L.; Rosen, M.; Meyer, B. K., *Mater. Sci. Eng., C* **2002**, *19*, 435.

[19] Hoyer, P.; Weller, H., *Chem. Phys. Lett.* **1994**, *221*, 379.

[20] Roest, A. L.; Germeau, A.; Kelly, J. J.; Vanmaekelbergh, D.; Allan, G.; Meulenkamp, E. A., *Chem. Phys. Chem.* **2003**, *4*, 959.

[21] Control experiments show that these EPR spectra are independent of quantum dot concentration in our experimental range, ruling out artifacts from interparticle interactions. See Appendix B.

[22] Nielsen, R. D.; Canaan, S.; Gladden, J. A.; Gelb, M. H.; Mailer, C.; Robinson, B. H., *J. Magn. Reson.* **2004**, *169*, 129.

[23] Wertz, J. E.; Bolton, J. R. *Electron Spin Resonance* (McGraw-Hill, New York, 1972).

[24] One electron in a 4.5 nm diameter nanocrystal corresponds to a carrier concentration of 2.1×10^{19} cm^{-1}.

[25] Norberg, N. S.; Kittilstved, K. R.; Amonette, J. E.; Kukkadapu, R. K.; Schwartz, D. A.; Gamelin, D. R., *J. Am. Chem. Soc.* **2004**, *126*, 9387.

[26] Liu, W.; Salley, G. M.; Gamelin, D. R., *J. Phys. Chem. B* **2005**, *109*, 14486.

[27] Mabbs, F. E.; Collison, D., *Electron Paramagnetic Resonance of d Transition Metal Compounds*; Elsevier: Amsterdam, 1992.

[28] Andrearczyk, T.; Jaroszy'nski, J.; Grabecki, G.; Dietl, T.; Fukumura, T.; Kawasaki, M., *Phys. Rev. B* **2005**, *72*, 121309.

[29] Milivojevic, D.; Babic Stojic, B.; Stojic, M.; Kulbachinskii, V. A.;

Maryanchuk, P.D.; Churilov, I. A., *Solid State Commun.* **2002**, *122*, 389.

Chapter 5: Summary

5.1 Summary

This chapter highlights some of the main conclusions of the cumulated work in this dissertation. One of the major characteristics desired of all photovoltaic devices is a match between the wavelengths at which the photoactive material absorbs and the wavelengths at which the photon source emits. In a commercial setting, that photon source is the Sun and the greater part of its emission energy is in the visible spectral region. For this reason, photovoltaic devices based on wide bandgap semiconductors often have a poor spectral matching, which in turn leads to an overall low cell performance. Hence, it is often required to augment the wide bandgap semiconductor material.

As discussed in Chapter 1, incorporation of a small percentage of 3*d* transition metals into the host semiconductor is one of the many strategies for sensitizing wide bandgap semiconductors to the visible spectral region. This has been observed to shift the spectral response of many of these wide bandgap semiconductors, such as ZnO,[19] ZnS,[10] TiO_2,[11] $InTaO_4$,[12,13] and others into the visible spectral region due to the presence of sub-bandgap energy levels. Until now, the photophysics behind the observed photoinduced charge separation from sub-bandgap excitation have been uncertain or inadequately investigated. The work performed in Chapter 2 with Co^{2+}:ZnO electrodes rationalizes the macroscopic photoinduced charge separation observed in Co^{2+}:ZnO and other 3*d* transition metal doped wide bandgap

semiconductors. The spectroscopic and photovoltaic measurements revealed, identified, and attributed two sub-bandgap charge transfer transition states ($ML_{CB}CT$ and $L_{VB}MCT$) as being responsible for the observed charge separation under visible light illumination. In addition, charge separation under direct Co^{2+} ligand field excitation can be understood as resulting from nonradiative energy transfer from the $^4T_1(P)$ Co^{2+} ligand field excited state to the overlapping broad $ML_{CB}CT$ energy state.

The internal quantum efficiencies for charge separation were observed to be dependent on the energy separation between the charge transfer and the excitonic excited states, with internal quantum efficiency increasing with decreasing energy separation between the two excited states as a result of greater mixing between two excited states. Both internal quantum efficiencies were smaller compared to those of photovoltaic cells based on a dye-sensitized nanostructured semiconductor (10%) or *p-n* silicon (13-24%) materials.[14] A slight improvement in the overall cell performance, however, was observed when changes in the physical parameters such as increased porosity and decreased resistance were made to the film. Unfortunately, even with these modifications to the cell considerable improvements are needed if these types of photovoltaic cells are to be competitive with today's conventional silicon solar cells for commercial solar energy conversion.

In light of these findings, the photoresponse in other 3*d* transition metal doped wide bandgap semiconductors, for example Ni-doped $InTaO_4$, can now be adequately understood. Although the authors ([refs. 12,13]) did not fully assign the origin of the

new broad intensity observed in the absorption spectrum after incorporating Ni into $InTaO_4$, an analogy with the results for Co^{2+}:ZnO suggest that a sub-bandgap charge transfer state is responsible for the observed charge separation in that material.

Overall, in terms of future material design of transition metal doped semiconductors for visible light photochemistry, our findings suggests that it would be favorable to select dopants that would tune the charge transfer energies near the excitonic excited state to optimize the charge separation efficiency. In addition, one should keep in mind that incorporation of a 3*d* transition metal does not guarantee photoinduced charge separation in regards to ligand field excitation. The excited electron in the ligand field excited state is highly localized on the 3*d* transition metal. For effective charge separation to occur, the ligand field excited state must be able to relax to a nearby charge transfer excited state. Otherwise, illumination at energies corresponding to the *d-d* excited state of the 3*d* transition metal will only lead to photon absorption but not to any photocurrent. This has been observed for the case of Ni^{2+}:ZnO, where there was a noticeable absence of photocurrent at the Ni^{2+} ligand field transition energies.[2]

The importance of possessing sub-bandgap charge transfer excited states in 3*d* transition metal doped semiconductors is not exclusive to the underlying photoinduced charge separation property of the material, but extends to the ferromagnetic property as well. In identifying the existence of a sub-bandgap $ML_{CB}CT$ in Mn^{2+}:ZnO and a $L_{VB}MCT$ in Co^{2+}:ZnO in close proximity to the excitonic excited state, we have added

to our current understanding of what gives rise to the observed ferromagnetism in these materials. The relevance of having a charge transfer excited state in close proximity to the band edge relates to the effectiveness of hybridization of the 3*d* transition metal dopant ions with shallow donor (for the case of Co^{2+}:ZnO) or acceptor (for the case of Mn^{2+}:ZnO) defect bands at the Fermi level. Analogous to the spin-split donor impurity-band model,[15] strong dopant-defect hybridization leads to high-T_C ferromagnetism as observed in these materials.[16,17] In addition, the type of charge transfer, metal-to-ligand or ligand-to-metal, was capable of revealing whether the pertinent charge carriers are holes or electrons, as demonstrated by the observation of ferromagnetism in *p*-type Mn^{2+}:ZnO and *n*-type Co^{2+}:ZnO, and nonferromagnetic behavior under opposite carrier conditions.

The work presented in Chapter 3 has demonstrated that it is worthwhile to investigate and identify the charge transfer states present in diluted magnetic semiconductors, the attraction being its usefulness to explain as well as predict the ferromagnetic property in the material. Analysis of the charge transfer states has already demonstrated itself to be an effective alternative means to elucidating the ferromagnetic behavior in 3*d* transition metal doped ZnO. This charge transfer analysis formalism can be a worthy addition to other theoretical models[18-25] pertaining to carrier mediated ferromagnetism in diluted magnetic semiconductors.

Inspired by the findings in Chapter 3, paramagnetic colloidal Mn^{2+}:ZnO and Co^{2+}:ZnO nanocrystals were charged with additional electrons by photochemical

reduction. The interest behind investigating a e^-_{CB} :TM^{2+}:ZnO system was the anticipation that the introduction of a carrier in the conduction band of the semiconductor would lead to *s-d* exchange interaction with the magnetic dopant. The presence of *s-d* exchange interaction between the additional conduction band electrons and the magnetic dopant *d* electrons in Mn^{2+}:ZnO was supported by the broadening of the Mn^{2+} hyperfine structure. The observation of carrier-magnetic dopant exchange interaction in these materials is encouraging, however, as to whether or not the interaction is strong enough to lead to ferromagnetism continues to be a topic for further investigation.

Although the EPR study in Chapter 4 was only performed on Mn^{2+}:ZnO and Co^{2+}:ZnO nanocrystals, the methodology employed is by no means exclusive but may be suitable as a basic framework for studying carrier-magnetic dopant exchange interactions in other charged diluted magnetic semiconductors. In addition, extending the study to higher semiconductor dimensions will offer the opportunity to examine how changes in the degree of quantum confinement may affect the strength of carrier-magnetic dopant interaction. Overall, the ability to introduce additional carriers into diluted magnetic semiconductors by photochemical reduction has provided an experimental method for investigating the role that carriers might play in regards to ferromagnetism in diluted magnetic semiconductors.

In regards to spin-based electronics, perhaps one of the most ambitious devices to be proposed by theoreticians is the quantum computer, in which quantum states of

the electron or nuclear spin function as a quantum bit (qubit). The immense interest in the quantum computer lies in its promise to outperform the conventional computer through the use of quantum algorithms.[26] The feasibility of a quantum computer relies heavily, among other prerequisites, on the ability of the qubits to remain coherent for the duration of the quantum computation.

Recently, Petta *et al.* demonstrated the coherent manipulation of coupled electron spins in a double quantum dots device.[27] They obtained a spin coherence time of ~10 ns in their GaAs/InGaAs quantum dots, measured at a low temperature (electron temperature ~135 mK). The use of GaAs for the quantum dots, however, may not have been ideal in this device due to the 100% abundance of nuclear spins in both Ga and As. As observed in Chapter 4, it was evident that electron-nuclear hyperfine interactions led to a shortening of the coherence time. Therefore from a materials perspective, there may be advantages to replacing GaAs in such a device with ZnO. It has been demonstrated in Chapter 4 that electron spins in colloidal ZnO quantum dots would remain coherent for up to 25 ns at room temperature, which is about twice as long as that for GaAs. And unlike GaAs, all the nuclear spins in ZnO can be removed, effectively eliminating electron-nuclear hyperfine interactions which in turn should increase the spin coherence time. Overall, the results in Chapter 4 suggest that ZnO quantum dots may be a promising candidate for spin-based applications. It is anticipated that if coherent manipulation of the electrons in ZnO

quantum dots can be achieved then the field will be a step closer towards the development of an actual quantum computer.

5.2 Notes to Chapter 5

[1] Kobayashi, K.; Maeda, T.; Matsushima, S.; Okada, G., *J. Mater. Sci.* **1992**, *27*, 5953.

[2] Bahadur, L.; Rao, T. N.; Pandey, J. P., *Semicond. Sci. Technol.* **1994**, *9*, 275.

[3] Jaramillo, T. F.; Baeck, S.-H.; Kleiman-Shwarsctein, A.; Choi, K.-S.; Stucky, G. D.; McFarland, E. W., *J. Comb. Chem.* **2005**, *7*, 264.

[4] Jakani, M.; Campet, G.; Claverie, J.; Fichou, D.; Pouliquen, J.; Kossanyi, J., *J. Solid State Chem.* **1985**, *56*, 269.

[5] Fichou, D.; Pouliquen, J.; Kossanyi, J.; Jakani, M.; Campet, G.; Claverie, J., *J. Electroanal. Chem.* **1985**, *188*, 167.

[6] Bahadur. L.; Rao, T. N., *Sol. Energy Mater. Sol. Cells* **1992**, *27*, 347.

[7] Kobayashi, K.; Maeda, T.; Matsushima, S.; Okada, G., *Jpn. J. Appl. Phys.* **1992**, *31*, L1079.

[8] Fichou, D.; Mesmaeker, A. K.-D., Pulsed laser-induced photopotentials at the cobalt-photosensitized ZnO/electrolyte interface. *J. Electroanal. Chem.* **1986**, *215*, 161.

[9] Fichou, D.; Mesmaeker, A. K.-D., Transient photopotentials at the cobalt-photosensitized ZnO/electrolyte interface. *Chem. Phys. Lett.* **1986**, *132*, 128.

[10] Kudo, A.; Sekizawa, M., *Catal. Lett.* **1999**, *58*, 241.

[11] Iwasaki, M.; Hara, M.; Kawada, H.; Tada, H.; Ito, S., *J. Colloid Interface Sci.* **2000**, *224*, 202.

[12] Zou, Z.; Ye, J.; Sayama, K.; Arakawa, H., *Nature* **2001**, *414*, 625.

[13] Zou, Z.; Ye, J.; Sayama, K.; Arakawa, H., *J. Photochem. Photobiol., A* **2002**, *148*, 65.

[14] Grätzel, M., Photoelectrochemical cells. *Nature* **2001**, *414*, 338.

[15] Coey, J. M. D.; Venkatesan, M.; Fitzgerald, C. B., *Nature Mater.* **2005**, *4*, 173.

[16] Kittilstved, K. R.; Norberg, N. S.; Gamelin, D. R., *Phys. Rev. Lett.* **2005**, *94*, 147209.

[17] Schwartz, D. A.; Gamelin, D. R., *Adv. Mater.* **2004**, *16*, 2115.

[18] Sato, K.; Katayama-Yoshida, H., *Semicond. Sci. Technol.* **2002**, *17*, 367.

[19] Sato, K.; Katayama-Yoshida, H., *Physica E* **2001**, *10*, 251.

[20] Sato, K.; Katayama-Yoshida, H., *Physica B* **2001**, *308-310*, 904.

[21] Sato, K.; Katayama-Yoshida, H., *Jpn. J. Appl. Phys.* **2001**, *40*, L334.

[22] Spaldin, N. A., *Phys. Rev. B* **2004**, *69*, 125201.

[23] Coey, J. M. D.; Venkatesan, M.; Fitzgerald, C. B., *Nature Mater.* **2005**, *4*, 173.

[24] Venkatesan, M.; Fitzgerald, C. B.; Lunney, J. G.; Coey, J. M. D., *Phys. Rev. Lett.* **2004**, *93*, 177206.

[25] Ueda, K.; Tabata, H.; Kawai, T., *Appl. Phys. Lett.* **2001**, *79*, 988.

[26] Awschalom, D. D.; Loss, D.; Samarth, N., *Semiconductor Spintronics and Quantum Computation*; Springer: New York, 2002.

[27] Petta, J. R.; Johnson, A. C.; Taylor, J. M.; Laird, E. A.; Yacoby, A.; Lukin, M. D.; Marcus, C. M.; Hanson, M. P.; Gossard, A. C., *Science* **2005**, *309*, 2180.

BIBLIOGRAPHY

[1] Andrearczyk, T.; Jaroszy'nski, J.; Grabecki, G.; Dietl, T.; Fukumura, T.; Kawasaki, M., Spin-related magnetoresistance of *n*-type ZnO:Al and $Zn_{1-x}Mn_xO$:Al thin films. *Phys. Rev. B* **2005**, *72*, 121309.

[2] Archer, P. I.; Radovanovic, P. V.; Heald, S. M.; Gamelin, D. R., Low-temperature activation and deactivation of high-T_C ferromagnetism in a new diluted magnetic semiconductor: Ni^{2+}-doped SnO_2. *J. Am. Chem. Soc.* **2005**, *127*, 14479.

[3] Awschalom, D. D.; Loss, D.; Samarth, N., *Semiconductor Spintronics and Quantum Computation*; Springer: New York, 2002.

[4] Bahadur, L.; Rao, T. N., Photoelectrochemical studies of cobalt-doped ZnO sprayed thin film semiconductor electrodes in acetonitrile medium. *Sol. Energy Mater. Sol. Cells* **1992**, *27*, 347.

[5] Bahadur, L.; Rao, T. N.; Pandey, J. P., Extension of the spectral response of sprayed ZnO thin film electrodes induced by nickel and cobalt doping. *Semicond. Sci. Technol.* **1994**, *9*, 275.

[6] Beschoten, B.; Crowell, P. A.; Malajovich, I.; Awschalom, D. D.; Matsukura, F.; Shen, A.; Ohno. H., Magnetic circular dichroism studies of carrier-induced ferromagnetism in $(Ga_{1-x}Mn_x)As$. *Phys. Rev. Lett.* **1999**, *83*, 3073.

[7] Beschoten, B.; Johnston-Halperin, E.; Young, D. K.; Poggio, M.; Grimaldi, J. E.; Keller, S.; DenBaars, S. P.; Mishra, U. K.; Hu, E. L.; Awschalom, D. D., Spin coherenece and dephasing in GaN. *Phys. Rev. B* **2001**, *63*, 121202(R).

[8] Bhattacharjee, A. K., Interactions between band electrons and transition-metal ions in diluted magnetic semiconductors. *Phys. Rev. B* **1992**, *46*, 5266.

[9] Bishop, S.G.; Robbins, D. J.; Dean, P. J., Evidence for exciton binding at Ni impurity sites in ZnSe. *Solid State Commun.* **1980**, *33*, 119.

[10] Blinowski, J.; Kacman, P.; Dietl, T., Kinetic exchange vs. room temperature ferromagnetism in diluted magnetic semiconductors. *Mater Res. Soc. Symp. Proc.* **2002**, *690*, 109.

[11] Brabec, C. J.; Nann, T.; Shaheen, S. E., Nanostructured *p-n* junctions for printable photovoltaics. *MRS Bull.* **2004**, *29*, 43.

[12] Braun, P.-F.; Marie, X.; Lombez, L.; Urbaszek, B.; Amand, T.; Renucci, P.; Kalevich, V. K.; Kavokin, K. V.; Krebs, O.; Voisin, P.; Matsumoto, Y., Direct observation of the electron spin relaxation induced by nuclei in quantum dots. *Phys. Rev. Lett.* **2005**, *94*, 116601.

[13] Bryan, J. D.; Gamelin, D. R., Doped semiconductor nanocrystals: Synthesis, characterization, physical properties, and applications. *Prog. Inorg. Chem.* **2005**, *54*, 47.

[14] Bryan, J. D.; Heald, S. M.; Chambers, S. A.; Gamelin, D. R., Strong room-temperature ferromagnetism in Co^{2+}-doped TiO_2 made from colloidal nanocrystals. *J. Am. Chem. Soc.* **2004**, *126*, 11640.

[15] Bryan, J. D.; Santangelo, S. A.; Keveren, S. C.; Gamelin, D. R., Activation of high-T_C ferromagnetism in Co^{2+}:TiO_2 and Cr^{3+}:TiO_2 nanorods and nanocrystals by grain boundary defects. *J. Am. Chem. Soc.* **2005**, *127*, 15568.

[16] Bulyanitsa, D. S.; Grinberg, A. A., Optical transitions between levels of a deep impurity center. *Sov. Phys. Semicond.* **1978**, *12*, 933.

[17] Cerletti, V.; Coish, W. A.; Gywat, O.; Loss, D., Recipes for spin-based quantum computing. *Nanotechnology* **2005**, *16*, R27, and references therein.

[18] Chambers, S. A.; Yoo, Y. K., Eds. A compilation of recent reviews: "New Materials for Spintronics". *MRS Bull.* **2003**, *23*, 706.

[19] Cheng, X. L.; Zhao, H.; Hso, L. H.; Gao, S.; Zhao, J. G., ZnO nanoparticulate thin film: preparation, characterization and gas-sensing property. *Sens. Actuators, B* **2004**, *102*, 248.

[20] Chukwu, L. O.; Nwachukwu, S. C. U., Impact of refined petroleum spills on water quality, macro-invertebrate and microbial communities of a tropical aquatic environment. *J. Environ. Bio.* **2005**, *26*, 449.

[21] Coey, J. M. D.; Venkatesan, M.; Fitzgerald, C. B., Donor impurity band exchange in dilute ferromagnetic oxides. *Nature Mater.* **2005**, *4*, 173.

[22] Cunningham, J.; Corkery, S., Reactions involving electron transfer at semiconductor surfaces. VI. Electron spin resonance studies on dark and illuminated aqueous suspensions of zinc oxides. *J. Phys. Chem.* **1975**, *79*, 933.

[23] Datta, S.; Das, B, Electronic analog of the electro-optic modulator. *Appl. Phys. Lett.* **1990**, *56*, 665.

[24] Dietl, T., Dilute magnetic semiconductors: Functional ferromagnets. *Nature Mater.* **2003**, *2*, 646.

[25] Dietl, T.; Ohno, H.; Matsukura, F.; Cibert, J.; Ferrand, D., Zener model description of ferromagnetism in zinc-blende magnetic semiconductors. *Science* **2000**, *287*, 1019.

[26] Duffy, J. A., Optical electronegativity, χ^*, of transition-metal ions in simple compounds. *J. Chem. Soc., Dalton Trans.* **1983**, 1475.

[27] Eisenberg, R.; Nocera, D. G., Preface: Overview of the Forum on solar and renewable energy. *Inorg. Chem.* **2005**, *44*, 6799.

[28] Fazzio, A.; Caldas, M. J.; Zunger, A., Many-electron multiplet effects in the spectra of 3*d* impurities in heteropolar semiconductors. *Phys. Rev. B* **1984**, *30*, 3430.

[29] Fernandez, N.; Cesar, A.; Gonzalez, M.; DelValls, T. A., Level of contamination in sediments affected by the Prestige oil spill and impact on the embryo development of the sea urchin. *Ciencias Marinas* **2006**, *32*, 421.

[30] Fernley, P. W.; Moore, M. N.; Lowe, D. M.; Donkin, P.; Evans, S., Impact of the Sea Empress oil spill on lysosomal stability in mussel blood cells. *Mar. Environ. Res.* **2000**, *50*, 451.

[31] Fichou, D.; Mesmaeker, A. K.-D., Pulsed laser-induced photopotentials at the cobalt-photosensitized ZnO/electrolyte interface. *J. Electroanal. Chem.* **1986**, *215*, 161.

[32] Fichou, D.; Mesmaeker, A. K.-D., Transient photopotentials at the cobalt-photosensitized ZnO/electrolyte interface. *Chem. Phys. Lett.* **1986**, *132*, 128.

[33] Fichou, D.; Pouliquen, J.; Kossanyi, J.; Jakani, M.; Campet, G.; Claverie, J., Extension of the photoresponse of semiconducting zinc oxide electrodes by 3*d*-impurities absorbing in the visible region of the solar spectrum. *J. Electroanal. Chem.* **1985**, *188*, 167.

[34] Fiederling, R.; Keim, M.; Reuscher, G.; Ossau, W.; Schmidt, G.; Waag, A.; Molenkamp L. W., Injection and detection of a spin-polarized current in a light-emitting diode. *Nature* **1999**, *402*, 787.

[35] Figgis, B. N.; Hitchman, M. A., *Ligand Field Theory and its Applications*; Wiley: New York, 2000.

[36] Fleurov, V. N.; Kikoin, K. A., Amphoteric exciton trapping by 3*d*-impurities in A_2B_6 semiconductors. *Solid State Commun.* **1982**, *42*, 353.

[37] Furdyna, J. K., Diluted magnetic semiconductors. *J. Appl. Phys.* **1988**, *64*, R29.

[38] Gemma, N., Electronic states of transition metal impurities in II-VI and III-V semiconductors. *J. Phys. C: Solid State Phys.* **1984**, *17*, 2333.

[39] Germeau, A.; Roest, A. L.; Vanmaekelbergh, D.; Allan, G.; Delerue, C.; Meulenkamp, E. A., Optical transitions in artificial few-electron atoms strongly confined inside ZnO nanocrystals. *Phys. Rev. Lett.* **2003**, *90*, 097401.

[40] Ghosh, S.; Sih, V.; Lau, W. H.; Awschalom, D. D.; Bae, S.-Y., Wang, S.; Vaidya, S.; Chapline, G., Room-temperature spin coherence in ZnO. *Appl. Phys. Lett.* **2005**, *86*, 232507.

[41] Grätzel, M., Photoelectrochemical cells. *Nature* **2001**, *414*, 338.

[42] Gupta, J. A.; Awschalom, D. D.; Efros, A. L., Spin dynamics in semiconductor nanocrystals. *Phys. Rev. B* **2002**, *66*, 125307.

[43] Gupta, J. A.; Awschalom, D. D.; Peng, X.; Alivisatos, A. P., Spin coherence in semiconductor quantum dots. *Phys. Rev. B* **1999**, *59*, 10421(R).

[44] Haase, M.; Weller, H.; Henglein, A., Photochemistry and radiation chemistry of colloidal semiconductors. 23. Electron storage on zinc oxide particles and size quantization. *J. Phys. Chem.* **1988**, *92*, 482.

[45] Hagfeldt, A.; Grätzel, M., Molecular photovoltaics. *Acc. Chem. Res.* **2000**, *33*, 269.

[46] Hauch, A.; Georg, A., Diffusion in the electrolyte and charge-transfer reaction at the platinum electrode in dye-sensitized solar cells. *Electrochim. Acta* **2001**, *46*, 3457.

[47] Heitz, R.; Hoffmann, A.; Broser, I., Magneto-optics of Ni-bound shallow states in ZnS and CdS. *Phys. Rev. B* **1993**, *48*, 8672.

[48] Hirano, T.; Kozuka, H., Photoanodic properties of ZnO thin films prepared from zinc acetate solutions containing cobalt acetate and polyvinylpyrrolidone. *J. Mater. Sci.* **2003**, *38*, 4203.

[49] Honda, K.; Fujishima, A., Electrochemical photolysis of water at a semiconductor electrode. *Nature* **1972**, *238*, 37.

[50] Hoyer, P.; Weller, H., Size-dependent redox potentials of quantized zinc oxide measured with an optically transparent thin layer electrode. *Chem. Phys. Lett.* **1994**, *221*, 379.

[51] Ivill, M.; Pearton, S. J.; Norton, D. P.; Kelly, J.; Hebard, A. F., Magnetization dependence on electron density in epitaxial ZnO thin films codoped with Mn and Sn. *J. Appl. Phys.* **2005**, *97*, 053904.

[52] Iwasaki, M.; Hara, M.; Kawada, H.; Tada, H.; Ito, S., Cobalt ion-doped TiO_2 photocatalyst response to visible light. *J. Colloid Interface Sci.* **2000**, *224*, 202.

[53] Jakani, M.; Campet, G.; Claverie, J.; Fichou, D.; Pouliquen, J.; Kossanyi, J., Photoelectrochemical properties of zinc oxide doped with 3*d* elements. *J. Solid State Chem.* **1985**, *56*, 269.

[54] Jaramillo, T. F.; Baeck, S.-H.; Kleiman-Shwarsctein, A.; Choi, K.-S.; Stucky, G. D.; McFarland, E. W., Automated electrochemical synthesis and photoelectrochemical characterization of $Zn_{1-x}Co_xO$ thin films for solar hydrogen production. *J. Comb. Chem.* **2005**, *7*, 264.

[55] Jonker, B. T.; Park, Y. D.; Bennett, B. R.; Cheong, H. D.; Kioseoglou, G.; Petrou, A., Robust electrical spin injection into a semiconductor heterostructure. *Phys. Rev. B* **2000**, *62*, 8180.

[56] Jørgensen, C. K., Optical electronegativities of 3d group central ions. *Mol. Phys.* **1963**, *6*, 43.

[57] Jørgensen, C. K., Electron transfer spectra. *Prog. Inorg. Chem.* **1970**, *12*, 101.

[58] Juhl, A.; Hoffmann, A.; Bimberg, D.; Schulz, H.-J., Bound-exciton-related fine structure in charge transfer spectra of InP:Fe detected by calorimetric

absorption spectroscopy. *Appl. Phys. Lett.* **1987**, *50*, 1292.

[59] Kanai, Y., Optical absorption and conduction due to Co^{2+} in ZnO crystals. *J. Phys. Soc. Jpn.* **1968**, *24*, 956.

[60] Kato, H.; Kudo, A., Visible-light-response and photocatalytic activities of TiO_2 and $SrTiO_3$ photocatalysts codoped with antimony and chromium. *J. Phys. Chem. B* **2002**, *106*, 5029.

[61] Kikkawa, J. M.; Awschalom, D. D., Resonant spin amplification in n-type GaAs. *Phys. Rev. Lett.* **1998**, *80*, 4313.

[62] Kikkawa, J. M.; Gupta, J. A.; Malajovich; Awschalom, D. D., Spin coherence in semiconductors: storage, transport, and reduced dimensionality. *Physica E* **2001**, *9*, 194.

[63] Kikkawa, J. M.; Smorchkova, I. P.; Samarth, N.; Awschalom, D. D., Room-temperature spin memory in two-dimensional electron gases. *Science* **1997**, *277*, 1284.

[64] Kittilstved, K. R.; Gamelin, D. R., Activation of high-T_C ferromagnetism in Mn^{2+}-doped ZnO using amines. *J. Am. Chem. Soc.* **2005**, *127*, 5292.

[65] Kittilstved, K. R.; Liu, W. K.; Gamelin, D. R., Electronic structure origins of polarity-dependent high-T_C ferromagnetism in oxide-diluted magnetic semiconductors. *Nature Mater.* **2006**, *5*, 291.

[66] Kittilstved, K. R.; Norberg, N. S.; Gamelin, D. R., Chemical manipulation of high-T_C ferromagnetism in ZnO diluted magnetic semiconductors. *Phys. Rev. Lett.* **2005**, *94*, 147209.

[67] Kobayashi, K.; Maeda, T.; Matsushima, S.; Okada, G., Mechanism of photoinduced charge transfer in Co(Li)-doped ZnO film. *Jpn. J. Appl. Phys.* **1992**, *31*, L1079.

[68] Kobayashi, K.; Maeda, T.; Matsushima, S.; Okada, G., Optical and electronic properties of cobalt-doped zinc oxide films prepared by the sputtering method. *J. Mater. Sci.* **1992**, *27*, 5953.

[69] Kobayashi, M.; Ishida, Y.; Hwang, J. I.; Mizokawa, T., Fujimori, A.; Mamiya, K.; Okamoto, J.; Takeda, Y.; Okane, T.; Saitoh, Y.; Muramatsu, Y.; Tanaka, A.; Saeki, H.; Tabata, H.; Kawai, T., Characterization of magnetic components

in the diluted magnetic semiconductor $Zn_{1-x}Co_xO$ by X-ray magnetic circular dichroism. *Phys. Rev. B* **2005**, *72*, 201201.

[70] Koidl, P., Optical absorption of Co^{2+} in ZnO. *Phys. Rev. B* **1977**, *15*, 2493.

[71] Korotkov, R. Y.; Gregie, J. M.; Wessels, B. W., Optical properties of the deep Mn acceptor in GaN:Mn. *Appl. Phys. Lett.* **2002**, *80*, 1731.

[72] Kudo, A.; Sekizawa, M., Photocatalytic H_2 evolution under visible light irradiation on $Zn_{1-x}Cu_xS$ solid solution. *Catal. Lett.* **1999**, *58*, 241.

[73] Langer, J. M.; Delerue, C.; Lannoo, M.; Heinrich, H., Transition-metal impurities in semiconductors and heterojunction band lineups. *Phys. Rev. B* **1988**, *38*, 7723.

[74] Lau, W. H.; Olesberg, J. T.; Flatté, M. E., Electron-spin decoherence in bulk and quantum-well zinc-blende semiconductors. *Phys. Rev. B* **2001**, *64*, 161301(R).

[75] Law, R. J.; Kelly, C., The impact of the "Sea Empress" oil spill. *Aqua. Living Res.* **2004**, **17**, 389.

[76] Lee, K.; Prince, R. C.; Greer, C. W.; Doe, K. G.; Wilson, J. E. H.; Cobanli, S. E.; Wohlgeschaffen, G. D.; Alroumi, D.; King, T.; Tremblay, G. H., Composition and toxicity of residual Bunker C fuel oil in intertidal sediments after 30 years. *Spill Sci. & Technol. Bull.* **2003**, *8*, 187.

[77] Lettmann, C.; Hinrichs, H.; Maier, W. F., Combinatorial discovery of new photocatalysts for water purification with visible light. *Angew. Chem., Int. Ed.* **2001**, *40*, 3160.

[78] Lever, A. B. P., *Inorganic Electronic Spectroscopy*, 2nd ed.; Elsevier Science Publishers: Amsterdam, The Netherlands, 1984, and references therein.

[79] Lim, S.-W.; Hwang, D.-K.; Myoung, J.-M., Observation of optical properties related to room-temperature ferromagnetism in co-sputtered $Zn_{1-x}Co_xO$ thin films. *Solid State Commun.* **2003**, *125*, 231.

[80] Lim, S.-W.; Jeong, M.-C.; Ham, M.-H.; Myoung, J.-M., Hole-mediated ferromagnetic properties in $Zn_{1-x}Mn_xO$ thin films. *Jpn. J. Appl. Phys.* **2004**, *43*, L280.

[81] Liu, C.; Yun, F.; Morkoc, H., Ferromagnetism of ZnO and GaN: A review. *J. Mater. Sci. Mater. Electron.* **2005**, *16*, 555.

[82] Liu, W. K.; Salley, G. M.; Gamelin, D. R., Spectroscopy of photovoltaic and photoconductive nanocrystalline Co^{2+}-doped ZnO electrodes. *J. Phys. Chem. B* **2005**, *109*, 14486.

[83] Liu, W. K.; Whitaker, K. M.; Kittilstved, K. R.; Gamelin, D. R., Stable photogenerated carriers in magnetic semiconductor nanocrystals. *J. Am. Chem. Soc.* **2006**, *128*, 3910.

[84] Look, D. C.; Claflin, B., *p*-type doping and devices based on ZnO. *Phys. Status Solidi B* **2004**, *241*, 624.

[85] Look, D. C.; Hemsky, J. W.; Sizelove, J. R., Residual native shallow donor in ZnO. *Phys. Rev. Lett.* **1999**, *82*, 2552.

[86] Loss, D.; DiVincenzo, D. P., Quantum computation with quantum dots. *Phys. Rev. A* **1998**, *57*, 120.

[87] Mabbs, F. E.; Collison, D., *Electron Paramagnetic Resonance of d Transition Metal Compounds*; Elsevier Science Publishers: Amsterdam, The Netherlands, 1992.

[88] Madan, A., Impact on the marine environment due to drill cuttings and oil spills. *Indian J. Environ. Protection* **1988**, *8*, 687.

[89] Maruska, H. P.; Ghosh, A. K., Photocatalytic decomposition of water at semiconductor electrodes. *Sol. Energy* **1978**, *20*, 443.

[90] Marzec, A., Carbon dioxide emission from fossil fuel: Major component of greenhouse gases. *Pol. J. Appl. Chem.* **2002**, *46*, 143.

[91] Masumoto, Y.; Pal, B.; Oguchi, S.; Ikezawa, M., Spin lifetime in electron-doped InP quantum dots. arXiv:cond-mat/0608046v1

[92] Matsumoto, Y.; Murakami, M.; Shono, T.; Hasegawa, T.; Fukumura, T.; Kawasaki, M.; Ahmet, P.; Chikyow, T.; Koshihara, S.; Koinuma, H., Room-temperature ferromagnetism in transparent transition metal-doped titanium dioxide. *Science* **2001**, *291*, 854.

[93] Mavroides, J. G.; Kafalas, J. A.; Kolesar, D. F., Photoelectrolysis of water in cells with $SrTiO_3$ anodes. *Appl. Phys. Lett.* **1975**, *28*, 241.

[94] Merkulov, I. A.; Efros, A. L.; Rosen, M., Electron spin relaxation by nuclei in semiconductor quantum dots. *Phys. Rev. B* **2002**, *65*, 205309.

[95] Milivojevic, D.; Babic Stojic, B.; Stojic, M.; Kulbachinskii, V. A.; Maryanchuk, P.D.; Churilov, I. A., Electron paramagnetic resonance studies of $Hg_{1-x}Mn_xTe_{1-y}Se_y$. *Solid State Commun.* **2002**, *122*, 389.

[96] Mizokawa, T.; Fujimori, A., Configuration interaction description of transition-metal impurities in II-VI semiconductors. *Phys. Rev. B* **1993**, *48*, 14150.

[97] Mizokawa, T.; Nambu, T.; Fujimori, A.; Fukumura, T.; Kawasaki, M., Electronic structure of the oxide-diluted magnetic semiconductor $Zn_{1-x}Mn_xO$. *Phys. Rev. B* **2002**, *65*, 085209.

[98] Moreira, S. M.; Moreira-Santos, M.; Ribeiro, R.; Guilhermino, L., The Coral Bulker fuel oil spill on the north coast of Portugal: Spatial and temporal biomarker responses in Mytilus galloprovincialis. *Ecotoxicol.* **2004**, *13*, 619.

[99] Müller, B.; Roussos, G.; Schulz, H.-J., Photoluminescence and excitation spectroscopy of Ni^{2+} and Ni^{+} centers in ZnS Crystals. *J. Cryst. Growth* **1985**, *72*, 360.

[100] Mulliken, R. S., Electronic population analysis on LCAO-MO molecular wavefunctions. II. Overlap populations, bond orders, and covalent bond energies. *J. Chem. Phys.* **1955**, *23*, 1841.

[101] Nielsen, R. D.; Canaan, S.; Gladden, J. A.; Gelb, M. H.; Mailer, C.; Robinson, B. H., Comparing continuous wave progressive saturation EPR and time domain saturation recovery EPR over the entire motional range of nitroxide spin labels. *J. Magn. Reson.* **2004**, *169*, 129.

[102] Noack, V.; Eychmüller, A., Annealing of nanometer-sized zinc oxide particles. *Chem. Mater.* **2002**, *14*, 1411.

[103] Noras, J. M.; Allen, J. W., Photoionisation of nickel in ZnS and ZnSe. *J. Phys. C: Solid State Phys.* **1980**, *13*, 3511.

[104] Norberg, N. S.; Kittilstved, K. R.; Amonette, J. E.; Kukkadapu, R. K.;

Schwartz, D. A.; Gamelin, D. R., Synthesis of colloidal Mn^{2+}:ZnO quantum dots and high-T_C ferromagnetic nanocrystalline thin films. *J. Am. Chem. Soc.* **2004**, *126*, 9387.

[105] Ohno, Y.; Young, D. K.; Beschoten, B.; Matsukura, F.; Ohno, H.; Awschalom, D. D., Electrical spin injection in a ferromagnetic semiconductor heterostructure. *Nature* **1999**, *402*, 790.

[106] Orlinskii, S. B.; Schmidt, J.; Baranov, P. G.; Hofmann, D. M.; de Mello Donegá, C.; Meijerink, A., Probing the wave function of shallow Li and Na donors in ZnO nanoparticles. *Phys. Rev. Lett.* **2004**, *92*, 047603.

[107] Osuji, L. C.; Adesiyan, S. O., The Isiokpo oil-pipeline leakage: Total organic carbon/organic matter contents of affected soils. *Chem. & Biodiversity* **2005**, *2*, 1079.

[108] Park, C. H.; Zhang, S. B.; Wei, S. H., Origin of *p*-type doping difficulty in ZnO: The impurity perspective. *Phys. Rev. B* **2002**, *66*, 073202.

[109] Papageorgiou, N.; Maier, W. F.; Grätzel, M., An iodine/triiodide reduction electrocatalyst for aqueous and organic media. *J. Electrochem. Soc.* **1997**, *144*, 876.

[110] Pearton, S. J.; Abernation, C. R.; Norton, D. P.; Hebard, A. F.; Park, Y. D.; Boatner, L. A.; Budai, J. D., Advances in wide bandgap materials for semiconductor spintronics. *Mater. Sci. Eng., R* **2003**, *40*, 137.

[111] Pearton, S. J.; Heo, W. H.; Ivill, M.; Norton, D. P.; Steiner, T., Dilute magnetic semiconducting oxides. *Semicond. Sci. Technol.* **2004**, *19*, R59.

[112] Pearton, S. J.; Norton, D. P.; Ip, K.; Heo, Y. W.; Steiner, T., Recent progress in processing and properties of ZnO. *Superlattices Microstruct.* **2003**, *34*, 3.

[113] Perrin, D. D.; Armarego, W. L. F.; Perrin, D. R., *Purification of Laboratory Chemicals*, 2nd ed.; Pergamon Press: New York, 1980; p568.

[114] Petit, L.; Schulthess, T. C.; Svane, A.; Temmerman, W. M.; Szotek, Z., Valencies of Mn impurities in ZnO. *Mater. Res. Soc. Symp. Proc. E* **2004**, *825*, G2.9.1.

[115] Petta, J. R.; Johnson, A. C.; Taylor, J. M.; Laird, E. A.; Yacoby, A.; Lukin, M. D.; Marcus, C. M.; Hanson, M. P.; Gossard, A. C., Coherent manipulation of

coupled electron spins in semiconductor quantum dots. *Science* **2005**, *309*, 2180.

[116] Radovanovic, P. V.; Gamelin, D. R., High-temperature ferromagnetism in Ni^{2+}-doped ZnO aggregates prepared from colloidal diluted magnetic semiconductor quantum dots. *Phys. Rev. Lett.* **2003**, *91*, 157202.

[117] Raupach, M. R.; Marland, G.; Ciais, P.; Le Quere, C.; Canadell, J. G.; Klepper, G., Proceedings of the National Academy of Sciences of the United States of America, **2007**, *104*, 10288.

[118] Robbins, D. J.; Dean, P. J.; West, C. L.; Hayes, W., The deep impurity→ conduction band charge transfer transition in ZnSe:Co. *Philos. Trans. R. Soc. London* **1982**, *304*, 499.

[119] Rodina, A. V.; Efros, A. L.; Rosen, M.; Meyer, B. K., Theory of the zeeman effect in semiconductor nanocrystals. *Mater. Sci. Eng., C* **2002**, *19*, 435.

[120] Roest, A. L.; Germeau, A.; Kelly, J. J.; Vanmaekelbergh, D.; Allan, G.; Meulenkamp, E. A., Long-range transport in an assembly of ZnO quantum dots: The effects of quantum confinement, coulomb repulsion and structural disorder. *Chem. Phys. Chem.* **2003**, *4*, 959.

[121] Rüster, C.; Borzenko, T.; Gould, C.; Schmidt, G.; Molenkamp, L. W.; Liu, X.; Wojtowicz, T. H.; Furdyna, J. K.; Yu, Z. G.; Flatté, M. E., Very large magnetoresistance in lateral ferromagnetic (Ga,Mn)As wires with nanoconstrictions. *Phys. Rev. Lett.* **2003**, *91*, 216602.

[122] Saeki, H.; Tabata, H.; Kawai, T., Magnetic and electric properties of vanadium doped ZnO films. *Solid State Commun.* **2001**, *120*, 439.

[123] Sato, K.; Katayama-Yoshida, H., Electronic structure and ferromagnetism of transition metal impurity doped zinc oxide. *Physica B* **2001**, *308-310*, 904.

[124] Sato, K.; Katayama-Yoshida, H., Ferromagnetism in a transition metal atom doped ZnO. *Physica E* **2001**, *10*, 251.

[125] Sato, K.; Katayama-Yoshida, H., First principles materials design for semiconductor spintronics. *Semicond. Sci. Technol.* **2002**, *17*, 367.

[126] Sato, K.; Katayama-Yoshida, H., Stablization of ferromagnetic states by electron doping in Fe-, Co-, or Ni-doped ZnO. *Jpn. J. Appl. Phys.* **2001**, *40*, L334.

[127] Schaub, R.; Thostrup, P.; Lopez, N.; Laegsgarrd, E.; Stensgaard,I.; Norskov, J. K.; Besenbacher, F., Oxygen vacancies as active sites for water dissociation on rutile TiO_2(110). *Phys. Rev. Lett.* **2001**, *87*, 266104.

[128] Schultz, H.-J.; Thiede, M., Optical spectroscopy of $3d^7$ and $3d^8$ impurity configurations in a wide-gap semiconductor (ZnO:Co, Ni, Cu). *Phys. Rev. B* **1987**, *35*, 18.

[129] Schwartz, D. A.; Gamelin, D. R., Reversible 300 K ferromagnetic ordering in a diluted magnetic semiconductor. *Adv. Mater.* **2004**, *16*, 2115.

[130] Schwartz, D. A.; Norberg, N. S.; Nguyen, Q. P.; Parker, J. M.; Gamelin, D. R., Magnetic quantum dots: synthesis, spectroscopy, and magnetism of Co^{2+}- and Ni^{2+}-doped ZnO nanocrystals. *J. Am. Chem. Soc.* **2003**, *125*, 13205.

[131] Serpone, N.; Lawless, D.; Disdier, J.; Hermann, J.-M., Spectroscopic, photoconductivity, and photocatalytic studies of TiO_2 colloids: Naked and with the lattice doped with Cr^{3+}, Fe^{3+}, and V^{5+} cations. *Langmuir* **1994**, *10*, 643.

[132] Shim, M.; Guyot-Sionnest, P., *n*-type colloidal semiconductor nanocrystals. *Nature* **2000**, *407*, 981.

[133] Shim, M.; Guyot-Sionnest, P., Organic-capped ZnO nanocrystals: Synthesis and *n*-type character. *J. Am. Chem. Soc.* **2001**, *123*, 11651.

[134] Shklovskii, B. I., Hopping conduction in lightly doped semiconductors. *Sov. Phys. Semicond.* **1973**, *6*, 1053.

[135] Smestad, G. P., Education and solar conversion: Demonstrating electron transfer. *Sol. Energy Mater. Sol. Cells* **1998**, *55*, 157.

[136] Solomon, E. I.; Hanson, M. A., Bioinorganic Spectroscopy. In *Inorganic Electronic Structure and Spectroscopy*; Solomon, E. I., Lever, A. B. P., Eds.; Wiley-Interscience: New York, 1999; Vol. II, p1.

[137] Soriano, J. A.; Vinas, L.; Franco, M. A.; Gonzalez, J. J.; Ortiz, L.; Bayona, J. M.; Albaiges, J., Spatial and temporal trends of petroleum hydrocarbons in

wild mussels from the Galician coast (NW Spain) affected by the Prestige oil spill. *Sci. Total Environ.* **2006**, *370*, 80.

[138] Spaldin, N. A., Search for ferromagnetism in transition-metal-doped piezoelectric ZnO. *Phys. Rev. B* **2004**, *69*, 125201.

[139] Thomas, D. G., Interstitial zinc in zinc oxide. *J. Phys. Chem. Solids* **1957**, *3*, 229.

[140] Ti Tien, H.; Chen, J.-W., Photoelectrolysis of water in semiconductor septum electrochemical photovoltaic cells. *Sol. Energy* **1992**, *48*, 199.

[141] Traversa, E.; Bearzotti, A., A novel humidity-detection mechanism for ZnO dense pellets. *Sens. Actuators, B* **1995**, *23*, 181.

[142] Ueda, K.; Tabata, H.; Kawai, T., Magnetic and electric properties of transition-metal-doped ZnO films. *Appl. Phys. Lett.* **2001**, *79*, 988.

[143] U.S. Department of Energy: Energy Information Administration, *International Energy Outlook 2007*; Washington, DC, DOE/EIA-0484 (2007).

[144] Venkatesan, M.; Fitzgerald, C. B.; Lunney, J. G.; Coey, J. M. D., Anisotropic ferromagnetism in substituted zinc oxide. *Phys. Rev. Lett.* **2004**, *93*, 177206.

[145] Wan, Q.; Li, Q. H.; Chen, Y. J.; Wang, T. H.; He, X. L.; Gao, X.G.; Li, J. P., Positive temperature coefficient resistance and humidity sensing properties of Cd-doped ZnO nanowires. *Appl. Phys. Lett.* **2004**, *84*, 3085.

[146] Wang, Q.; Sun, Q.; Jena, P.; Kawazoe,Y., Carrier-mediated ferromagnetism in N codoped (Zn,Mn)O $(10\bar{1}0)$ thin films. *Phys. Rev. B* **2004**, *70*, 052408.

[147] Weakliem, H. A., Optical spectra of Ni^{2+}, Co^{2+}, and Cu^{2+} in tetrahedral sites in crystals. *J. Chem. Phys.* **1962**, *36*, 2117.

[148] Wertz, J. E.; Bolton, J. R., *Electron Spin Resonance*; McGraw-Hill: New York., 1972.

[149] Wolf, S. A.; Awschalom, D. D.; Buhrman, R. A.; Daughton, J. M.; von Molnár, S.; Roukes, M. L.; Chtchelkanova, A. Y.; Treger, D. M., Spintronics: A spin-based electronics vision for the future. *Science* **2001**, *294*, 1488.

[150] Wolfsberg, M.; Helmholz, L., The spectra and electronic structure of the

tetrahedral ions MnO_4, CrO_4, and ClO_4. *J. Chem. Phys.* **1952**, *20*, 837.

[151] Wong, W. C.; McClure, D. S.; Basun, S. A.; Kokta, M. R., Charge-exchange processes in titanium-doped sapphire crystals. I. Charge-exchange energies and titanium-bound excitons. *Phys. Rev. B* **1995**, *51*, 5682.

[152] Wrzesinski, J.; Fröhlich, D., Determination of electronic parameters of ZnO by nonlinear spectroscopy. *Solid State Commun.* **1998**, *105*, 301.

[153] Zhou, H.; Hofstaetter, A.; Hoffman, D. M.; Meyer, B. K., Magnetic resonance studies on ZnO nanocrystals. *Microelectron. Eng.* **2003**, *66*, 59.

[154] Zou, Z.; Ye, J.; Sayama, K.; Arakawa, H., Direct splitting of water under visible light irradiation with an oxide semiconductor photocatalyst. *Nature* **2001**, *414*, 625.

[155] Zou, Z.; Ye, J.; Sayama, K.; Arakawa, H., Photocatalytic hydrogen and oxygen formation under visible light irradiation with M-doped $InTaO_4$ (M = Mn, Fe, Co, Ni and Cu) photocatalysts. *J. Photochem. Photobiol., A* **2002**, *148*, 65.

Appendix A: Supplementary Information to Chapter 3

A.1 Calculation of $L_{VB}MCT$ and $ML_{CB}CT$ transition energies used for plotting Figure 3.3.3.2.

The $L_{VB}MCT$ and $ML_{CB}CT$ transition energies plotted in Figure 3.3.3.2 were calculated using Jørgensen's optical electronegativity model[1,2] (Eqn. A.1.1), but with Pauling electronegativities for comparison across the series of TM^{2+}:ZnO DMSs.

$$E_{CT}\left(cm^{-1}\right) = 30000cm^{-1}\left(\chi_{opt}(D) - \chi_{opt}(A)\right) + \Delta SPE \pm 10Dq \quad \text{Eqn. [A.1.1]}$$

The first term of Eqn. A.1.1 describes the difference in Pauling electronegativities between the donors and acceptors. Valence and conduction band electronegativities on the Pauling scale (χ_{opt} = 2.278 and 1.113, respectively) were calibrated using the spectroscopic $L_{VB}MCT$ and $ML_{CB}CT$ transition energies of Co^{2+}- and Mn^{2+}-doped ZnO (Figure 3.3.2.1) and their Pauling electronegativities as described in refs. [3] and [4]. The spin-pairing energies were calculated using Eqn. A.1.2.

$$SPE = \left[\left\langle S(S+1)\right\rangle - S(S+1)\right]D \quad \text{Eqn. [A.1.2]}$$

where $\left\langle S(S+1)\right\rangle$ is the average $S(S+1)$ value for a given transition metal configuration of l^q, where l is the orbital angular momentum quantum number (2 for d orbitals), q is the number of electrons in the $3d$ orbitals, and S is the spin quantum number. The quantity $\left\langle S(S+1)\right\rangle$ was evaluated using Eqn. A.1.3.

$$\langle S(S+1)\rangle = \frac{q(q+2)}{4} - \frac{(2l+2)q(q-1)}{2(4l+1)} = \frac{q(q+2)}{4} - \frac{q(q-1)}{3} \qquad \text{Eqn. [A.1.3]}$$

The value D in Eqn. A.1.2 is related to Racah parameters for electron-electron repulsion, B and C, as described by Eqn. A.1.4.[1,2]

$$D = \frac{7}{6}\left(\frac{5}{2}B_{dopant} + C_{dopant}\right) \qquad \text{Eqn. [A.1.4]}$$

The nephaleuxetic ratios ($\beta = B_{\text{dopant}}/B_{\text{free ion}}$ and $\gamma = C_{\text{dopant}}/C_{\text{free ion}}$) were assumed constant across the series of TM^{2+}:ZnO complexes. Average values of $\beta = 0.74$ and $\gamma = 0.91$ were determined from literature values for Mn^{2+}:ZnO,[4] Co^{2+}:ZnO,[5] and Ni^{2+}:ZnO[5] and applied to dopants for which experimental Racah parameters in ZnO are not known. $B_{\text{free ion}}$ and $C_{\text{free ion}}$ values for those ions were taken from the book by Figgis and Hitchman.[6]

The last term in Eqn. A1.1 is the ligand field splitting energy, $10Dq$, which is roughly 4000 cm^{-1} across the series of TM^{2+} dopants in ZnO [Dq = 420 cm^{-1} (Mn^{2+})[4] 390 cm^{-1} (Co^{2+})[5] 420 cm^{-1} (Ni^{2+})[5]]. Changes in Dq across the series are negligible relative to changes in the first two terms of Eqn. A.1.1. All parameters used in calculating L_{VB}MCT and ML_{CB}CT transition energies are tabulated in Table A.1.1.

Table A.1.1. Parameters used for calculating $L_{VB}MCT$ and $ML_{CB}CT$ transition energies by Eqn. A.1.1. All energies are given in cm^{-1}.

		Metal-to-Ligand (CB) CT			Ligand (VB)-to-Metal CT		
TM^{2+}	$\chi_{Pauling}$	ΔSPE $l^q \rightarrow l^{q-1}$	Ligand Field Correction	$E_{ML_{CB}CT}$	ΔSPE $l^q \rightarrow l^{q+1}$	Ligand Field Correction	$E_{L_{VB}MCT}$
(Sc^{2+})	0.70*	0	0	-12393	-2518	0	44829
(Ti^{2+})	0.90*	2893	0	-3500	-5786	4000	39561
V^{2+}	1.63	6266	-4000	17773	-9399	4000	14048
Cr^{2+}	1.66	10519	-4000	22926	-14026	4000	8521
Mn^{2+}	1.55	16688	-4000	24000	16688	0	36740
Fe^{2+}	1.83	-16059	0	5448	12044	0	25491
Co^{2+}	1.88	-12658	0	9727	8439	4000	24800
Ni^{2+}	1.91	-8744	-4000	10432	4372	4000	19784
Cu^{2+}	1.90	-5112	-4000	14495	0	4000	15347

*Pauling electronegativities for Sc^{2+} and Ti^{2+} were not found, and these values were instead estimated following Jørgensen's empirical method.[7] Because $E_{ML_{CB}CT} << 0$ for both Sc^{2+} and Ti^{2+}, these ions were not considered further in this analysis.

A.2 LSDA-DFT data used for plotting Figure 3.3.3.2.

Figure 3.3.3.2 includes LSDA-DFT data adapted from refs. [8] and [9]. The stabilization energies of the ferromagnetic phases in $TM^{2+}:Zn_{1-x}O$ (TM^{2+} = Mn^{2+}, Fe^{2+}, Co^{2+}, and Ni^{2+}) with donors (Ga^{2+}) or acceptors $\left(N_O^{2-}\right)$, calculated for x = 0.25 and donor/acceptor concentrations of 25%, were normalized to those of Co^{2+}:ZnO

(n-type) or Mn^{2+}:ZnO (p-type) and included in Figure 3.3.3.2 for comparison to experimental and spectroscopic results. Negative stabilization energies in refs. [8] and [9] were plotted as zeros in Figure 3.3.3.2. For reference, the LSDA-DFT values plotted in Figure 3.3.3.2 are tabulated in Table A.2.1. Although the computational data for $x = 0.25$ were used, the trends in refs. [8] and [9] are largely independent of x, as demonstrated by the similarity of Figure 3.3.3.2 to the same plot made using $x = 0.05$ in Figure A.2.1.

Table A.2.1. Calculated energy differences between ferromagnetic (FM) and antiferromagnetic (AFM) phases in $TM^{2+}_{0.25} : Zn_{1-x}O$ (with Ga^{2+}_{Zn} or N^{2-}_{O} doping at 25% for n- or p-type, respectively). Data from refs. [8] and [9].

$TM^{2+}_{0.25} : Zn_{1-x}O$	n-type $\left(25\%\ Ga^{2+}_{Zn}\right)$		p-type $\left(25\%\ N^{2-}_{O}\right)$	
TM^{2+}	ΔE_{FM-AFM} (eV)	$\dfrac{\Delta E_{FM}}{\Delta E_{FM(Co^{2+})}}$	ΔE_{FM-AFM} (eV)	$\dfrac{\Delta E_{FM}}{\Delta E_{FM(Mn^{2+})}}$
Mn^{2+}	-0.043	0	0.035	1
Fe^{2+}	0.036	1.03	-0.076	0
Co^{2+}	0.035	1	-0.031	0
Ni^{2+}	0.026	0.74	-0.005	0

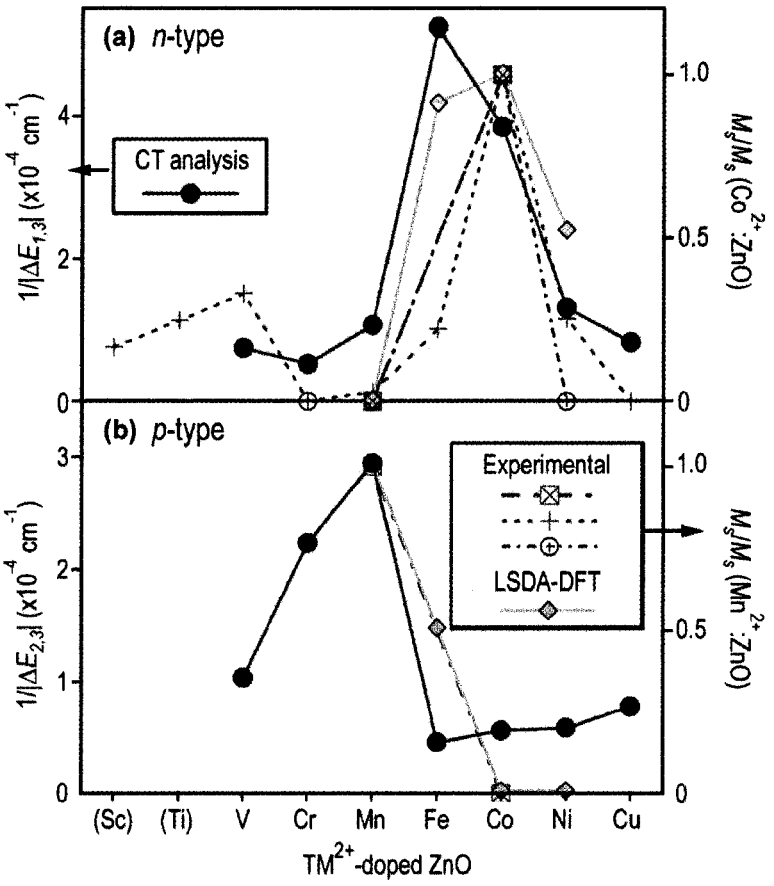

Figure A.2.1. Same as Figure 3.3.3.2 from the manuscript except now plotted using computational data from refs. [8] and [9] for $x = 0.05$ rather than $x = 0.25$ (the data in Figure 3.3.3.2). The trends are the same as those described by Figure 3.3.3.2.

A.3 Electrical and magnetic data used for plotting Figure 3.3.3.2.

Table A.3.1. Summary of thin film electrical and magnetic properties for literature data used in Figure 3.3.3.2. Each of the two data sets was assumed to have minimized differences due to changes in carrier and dopant concentration across the series.

TM^{2+}:ZnO, reported nominal TM^{2+} concentration (%)	Carrier Concentration (cm^{-3})	P_{O_2} during growth	T_C (K)	M_s (μ_B / TM^{2+})	Ref.
15% Co^{2+}	e^-=2.90×10^{20}	2-4×10^{-5} Torr	~300	2.0	10
5-25% Mn^{2+}	not reported	2-4×10^{-5} Torr	†	0.0	10
5-25% Cr^{2+}	not reported	2-4×10^{-5} Torr	†	0.0	10
5-25% Ni^{2+}	not reported	2-4×10^{-5} Torr	†	0.0	10
5% Cu^{2+}	not reported	10^{-4} mbar	†	0.05	11
5% Ni^{2+}	not reported	10^{-4} mbar	>300	0.49	11
5% Co^{2+}	not reported (*n*-type)	10^{-4} mbar	>300	1.94	11
5% Fe^{2+}	not reported (insulating)	10^{-4} mbar	>300	0.43	11
5% Mn^{2+}	not reported	10^{-4} mbar	†	0.05	11
5% Cr^{2+}	not reported (insulating)	10^{-4} mbar	†	0.00	11
5% V^{2+}	not reported	10^{-4} mbar	>300	0.64	11
(5% Ti^{2+})	not reported (insulating)	10^{-4} mbar	>300	0.48	11
(5% Sc^{2+})	not reported	10^{-4} mbar	>300	0.32	11
0.20% Mn^{2+}	not measurable	air	†	0.0	12, *
0.20% Mn^{2+}	not measurable	air + added amine	>350	1.5	12, *
3.5% Co^{2+}	not measurable	air	>350	0.04	12, *
3.5% Co^{2+}	not measurable	air + added amine	†	0.0	12, *

† Not ferromagnetic. * This work.

A.4 Magnetic data used for plotting Figure 3.3.1.1(a).

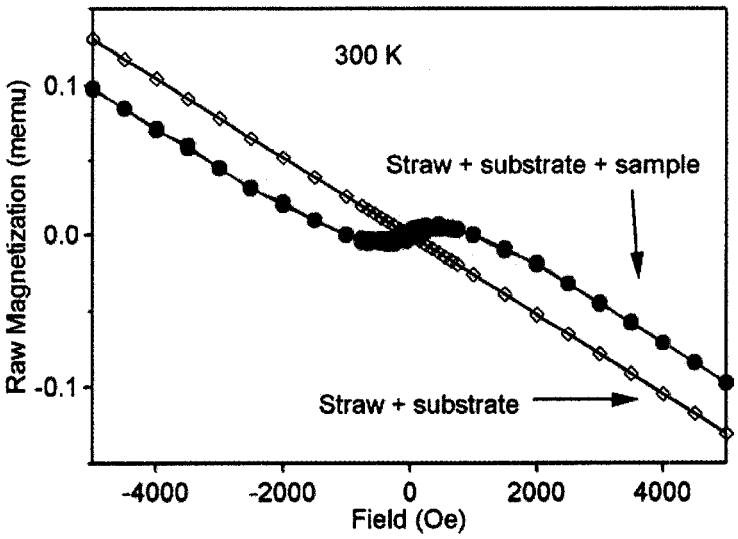

Figure A.4.1. Raw 300 K SQUID magnetization data for the sample shown in Figure 3.3.1.1(a). (◇) Bare substrate in a straw, showing net diamagnetism at 300 K. (●) Spin-coated film of 0.2% Mn^{2+}:ZnO N-capped nanocrystals, showing ferromagnetic signal superimposed on the net diamagnetic background. All data reported in Figure 3.3.1.1 were obtained by subtraction of the net diamagnetic background from the sample's raw magnetization.

A.5 Notes to Appendix A

[1] Jørgensen, C. K., *Progress in Inorg. Chem.* **1970**, *12*, 101.

[2] Lever, A. B. P., *Inorganic Electronic Spectroscopy* (Elsevier Science Publishers, Amsterdam, 1984, and references therein.).

[3] Schwartz, D. A.; Norberg, N. S.; Nguyen, Q. P.; Parker, J. M.; Gamelin, D. R., *J. Am. Chem. Soc.* **2003**, *125*, 13205.

[4] Norberg, N. S.; Kittilstved, K. R.; Amonette, J. E.; Kukkadapu, R. K.; Schwartz, D. A.; Gamelin, D. R., *J. Am. Chem. Soc.* **2004**, *126*, 9387.

[5] Weakliem, H. A., *J. Chem. Phys.* **1962**, *36*, 2117.

[6] Figgis, B. N. & Hitchman, M. A. *Ligand Field Theory and its Applications* (Wiley, N.Y., 2000, and references therein).

[7] Jørgensen, C. K., *Mol. Phys.* **1963**, *6*, 43.

[8] Sato, K.; Katayama-Yoshida, H., *Semicond. Sci. Technol.* **2002**, *17*, 367.

[9] Sato, K.; Katayama-Yoshida, H., *Jpn J. of Appl. Phys.* **2001**, *40*, L334.

[10] Ueda, K.; Tabata, H.; Kawai, T., *Appl. Phys. Lett.* **2001**, *79*, 988.

[11] Venkatesan, M.; Fitzgerald, C. B.; Lunney, J. G.; Coey, J. M. D., *Phys. Rev. Lett.* **2004**, *93*, 177206.

[12] Kittilstved, K. R.; Norberg, N. S.; Gamelin, D. R., *Phys. Rev. Lett.* **2005**, *94*, 147209.

Appendix B: Supplementary Information to Chapter 4

B.1 IR versus $\langle n \rangle$ plot

Figure B.1.1 shows the change in the near infrared intensity with $\langle n \rangle$ analyzed using the same statistical model used for the EPR intensity. The relative *S-P:P-D* oscillator strength used in the calculation is 0.25, in good agreement with the published ratio (~0:33) (ref. [1]).

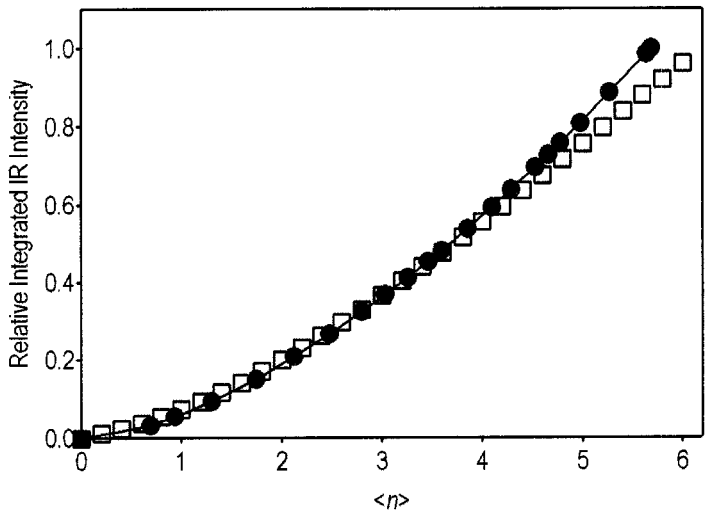

Figure B.1.1. The relative integrated near infrared intensity (◖) plotted with the calculated infrared intensity (□) based the same statistical model as for the EPR in Figure 4.3.1.2.

B.2. Concentration dependence on the EPR Lorentzian line broadening

To ensure that the concentration of ZnO quantum dots in the sample made no significant contribution to the measured EPR line broadening, two samples of ZnO with different quantum dot concentrations were measured and analyzed. The results in Figure B.2.1 show that no sample concentration dependence of the Lorentzian line broadening within the concentration range used, 62.8 μM and 628 μM ZnO quantum dots. All samples measured in Chapter 4 are within this concentration range, ~280 μM ZnO quantum dots.

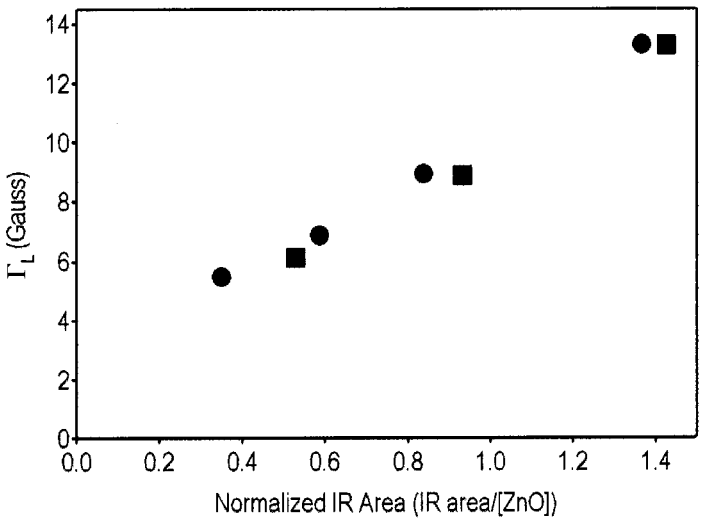

Figure B.2.1. EPR Lorentzian line width for colloidal ZnO quantum dot concentrations of 62.8 μM (●) and 628 μM (■).

B.3 Correlating IR and $\langle n \rangle$

Empirical correlation between integrated IR intensity and the average number of electrons, $\langle n \rangle$. The expression was used to place the EPR data on an $\langle n \rangle$ scale in Figure 4.3.1.2.

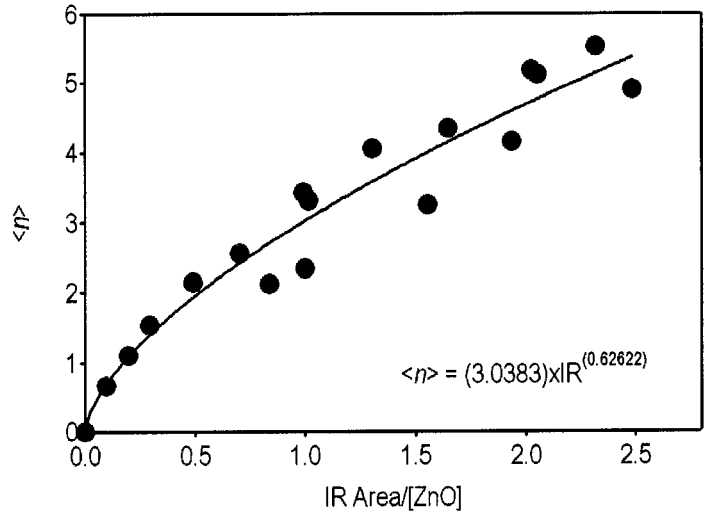

Figure B.3.1. Results of the ZnO/methyl viologen titration experiments. The data points (•) are from titration experiments with methyl viologen and the blue line is the fit. The expression is used to place the EPR data on a $\langle n \rangle$ scale in Figure 4.3.1.2.

B.4 Spin-weighted Poissonian plot for $S = ½$ only

The spin-weighted Poissonian probabilities for *S*, *P*, and *D* filling in an ensemble of ZnO QDs where only the $S = ½$ is considered is shown in Figure B.4.1. The calculated curve fails to adequately reproduce the curvature of the experimental result of Figure 4.3.1.2.

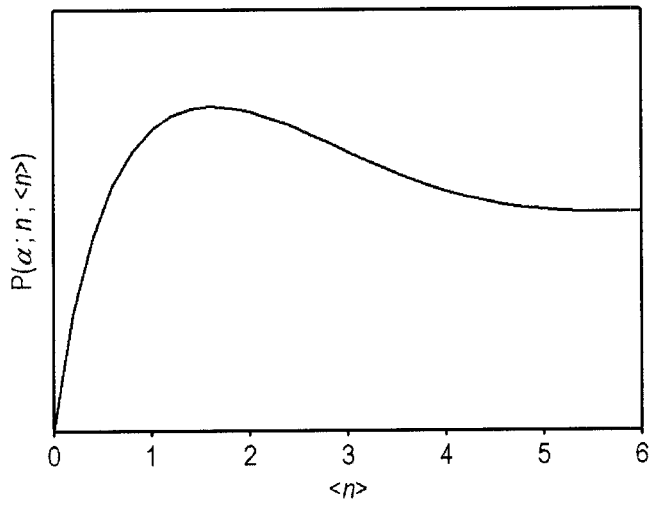

Figure B.4.1. Spin-weighted Poissonian probabilities for *S*, *P*, and *D* filling in an ensemble of ZnO QDs where only the $S = ½$ is considered.

B.5 Information on the isotopic distribution of zinc in depleted zinc acetate

Table B.5.1. Isotopic distribution of zinc in depleted zinc acetate (Lot Number: DZA2004AV7-11). Information provided by Trace Sciences International in the Certificate of Analysis.

Zn-64	Zn-66	Zn-67	Zn-68	Zn-70
$I = 0$	$I = 0$	$I = 5/2$	$I = 0$	$I = 0$
0.89%	32.38%	9.60%	55.10%	2.03%

B.6 The inhomogeneous contribution, $\Gamma_{\Delta g^*}$, from the deconvolved EPR data

The inhomogeneous contribution, $\Gamma_{\Delta g^*}$, from the deconvolved EPR data for ZnO quantum dots ($d = 4.60 \pm 0.4$ nm, 298 K) as a function of $\langle n \rangle$.

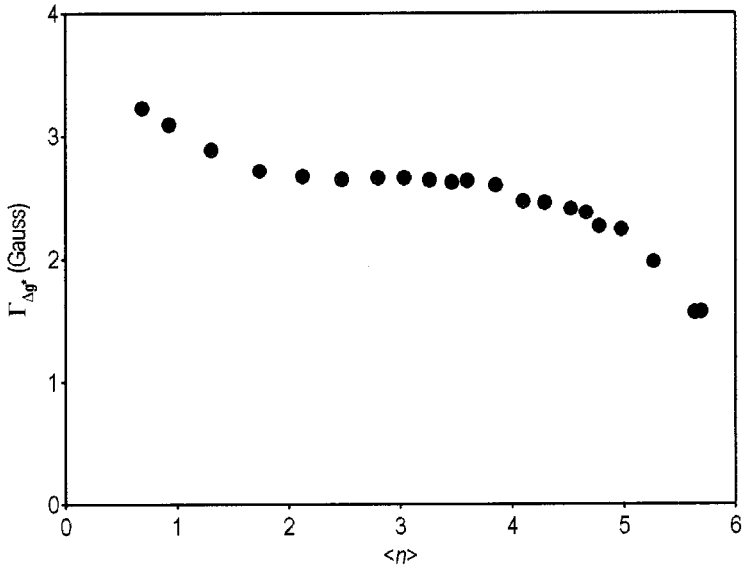

Figure B.6.1. Inhomogeneous contribution, $\Gamma_{\Delta g^*}$, to the lineshape in each EPR spectrum for ZnO quantum dots ($d = 4.60 \pm 0.4$ nm, 298 K) as a function of $\langle n \rangle$.

B.7 Notes to Appendix B

[1] Germeau, A.; Roest, A. L.; Vanmaekelbergh, D.; Allan, G.; Delerue, C.; Meulenkamp, E. A., *Phys. Rev. Lett.* **2003**, *90*, 097401.

VITA

William Liu was born in Hong Kong, China. After serving six years in the United States Navy, he returned to Portland, Oregon where he earned a Bachelor of Science degree in Chemistry from Portland State University. In 2002 he joined the research group of Professor Daniel R. Gamelin at the University of Washington where he earned a Doctor of Philosophy in Chemistry in 2007.